PERFORMANCE ENHANCEMENT OF FIBER OPTIC PHOTOTHERMAL INTERFEROMETRY FOR GAS SENSING

HONG YINGZHEN

PhD

The Hong Kong Polytechnic University

2023

The Hong Kong Polytechnic University

Department of Electrical and Electronic Engineering

Performance enhancement of fiber optic photothermal interferometry for gas sensing

HONG YINGZHEN

A thesis submitted in partial fulfilment of the requirements for
the degree of Doctor of Philosophy

June 2023

CERTIFICATE OF ORIGINALITY

I hereby declare that this thesis is my own work and that, to the best of my knowledge and belief, it reproduces no material previously published or written, nor material that has been accepted for the award of any other degree or diploma, except where due acknowledgement has been made in the text.

____________________ (Signed)

HONG Yingzhen (Name of student)

Abstract

Trace gas sensing holds importance in numerous domains, encompassing air pollution surveillance, medical examination, and industrial process regulation. Laser absorption spectroscopy (LAS) has been widely used in gas detection, utilizing the unique "fingerprint" absorption characteristics of gas molecules. Photothermal interferometry (PTI) is a derivative of LAS that offers high sensitivity for trace gas detection, involving two lasers for pumping and probing. A modulated pump laser generates heat in the gas medium, modulates its local refractive index (RI) and subsequently the phase of a probe beam propagating within the medium. This modulation can be detected via optical interferometry.

Diverse gas species have been detected in the laboratory environment with noise-equivalent-concentrations (NEC) down to parts-per-billion (ppb) level, utilizing different interferometric configurations. However, the ultra-low detection limit does not directly applicable to practical applications that demand high sensitivity and long-term stability. Thus, the objective of this thesis is to improve the performance of hollow-core fiber (HCF)-based PTI gas sensors to make them more applicable to real-world situations.

Several interferometric schemes have been scrutinized to detect gases exhibiting strong absorption in the near-infrared (NIR) spectrum. However, gases like oxygen do not have strong

absorption in the NIR. Given the inherent simplicity of the Fabry-Perot interferometer (FPI), which enables the independent utilization of the pump and probe transmission optics, we propose a visible-pump and NIR-probe FPI scheme. This approach allows for efficient access to the strong absorption lines within the visible spectrum, while also providing a cost-effective solution for using a NIR probe interferometer. We further propose a high-finesse Fabry-Perot (FP) cavity with a short HCF, yielding superior performance compared to the low-finesse FPI. With a 1-cm-long HCF gas cell, we demonstrate an oxygen detection down to 6 parts-per-million (ppm) with a 1000-s averaging time.

In PTI systems, the probe source commonly employed is a narrow-linewidth laser. However, the use of such a laser induces unwanted intensity fluctuations due to parasitic interference. To counteract this, we propose a fiber optic low-coherence (LC) PTI system, which employs a broadband probe source with a short coherence length. With a 10-cm-long HCF, we achieve acetylene detection with measurement precision of 0.025% and instability of ±0.038% over 3 hours. Theoretical analysis and experimental investigation of parasitic interference reveal that LC-PTI offers improved measurement precision and long-term stability compared to traditional PTI.

To further enhance the gas detection sensitivity, we demonstrate the optical phase-modulation amplification (OPMA) by using an HCF FP cavity and a dual-mode interferometer (DMI),

respectively. By locking the probe wavelength to the resonance of an FP cavity, OPMA of over two orders of magnitude is achieved, enabling ultra-sensitive gas detection with large dynamic range. However, it requires accurate wavelength locking, which is complex for practical applications. Hence, we further demonstrate the OPMA by operating a DMI at destructive interference and use it to achieve carbon dioxide detection with NEC of 1 ppb with a 50-cm-long HCF. The OPMA can be employed to improve the sensitivity of phase modulation-based sensors.

Acknowledgements

First and foremost, I would like to extend my deepest gratitude to my supervisor, Prof. Wei Jin, for his unwavering guidance and encouragement throughout my PhD journey. The invaluable insights gained from our meetings and discussions enable me to overcome the challenges I have faced. His open-mindedness, expertise, and patience are crucial in transforming ideas and unexpected discoveries into publishable results.

I am also immensely grateful to Dr. Haihong Bao and Mr. Feifan Chen for their invaluable contributions to my academic growth. Their stimulating conversations and insights reignite my innate curiosity for research during my PhD studies.

My heartfelt appreciation goes out to my colleagues Dr. Hoi Lut Ho, Dr. Shoulin Jiang, Dr. Yun Qi, Dr. Yan Zhao, Dr. Chao Wang, Dr. Pengcheng Zhao, Dr. Shuangxiang Zhao, Dr. Kaiyuan Zheng, Mr. Hanyu Liao, and Mr. Linhao Guo. Their valuable discussions and generous assistance have made a significant impact on my work.

I would also like to acknowledge Prof. Yingying Wang and Dr. Shoufei Gao for their kind provision of the hollow-core fibers, which greatly facilitate our research.

Last but not least, I am forever grateful to Han Gao and my loving parents for their unwavering support and affection throughout this journey.

Publications Arising from the Thesis

Journal articles

[1] **Y. Hong**, H. Bao, W. Jin, S. Jiang, H. L. Ho, S. Gao, and Y. Wang, "Oxygen gas sensing with photothermal spectroscopy in a hollow-core negative curvature fiber," *Sensors,* vol. 20, no. 21, 2020, 6084.

[2] **Y. Hong**, F. Chen, H. Bao, W. Jin, S. Jiang, H. L. Ho, S. Gao, and Y. Wang, "Amplified photothermal phase modulation for carbon dioxide detection by operating a dual-mode interferometer at destructive interference," *Anal. Chem.*, vol. 95, no. 8, pp. 4204-4211, 2023.

[3] **Y. Hong**, H. Bao, F. Chen, W. Jin, H. L. Ho, S. Gao, and Y. Wang, "Low-coherence photothermal interferometry for precision spectroscopic gas sensing," *Laser Photonics Rev.*, 2300358.

[4] H. Bao, **Y. Hong**, W. Jin, H. L. Ho, C. Wang, S. Gao, Y. Wang, and P. Wang, "Modeling and performance evaluation of in-line Fabry-Perot photothermal gas sensors with hollow-core optical fibers," *Opt. Express*, vol. 28, no. 4, pp. 5423–5435, 2020.

[5] H. Bao, **Y. Hong**, W. Jin, H. L. Ho, S. Gao, and Y. Wang. "Phase-modulation-amplifying hollow-core fiber photothermal interferometry for ultrasensitive gas sensing," *J. Light. Technol.*, vol. 40, no. 1, pp. 313-322, 2022.

Conference articles

[1] **Y. Hong**, H. Bao, W. Jin, H. L. Ho, Y. Zhao, S. Gao, and Y. Wang, “Oxygen sensing with laser photothermal spectroscopy in a hollow-core optical fiber,” in *Optical Fiber Sensors Conference 2020 Special Edition*, 2020, pp. Th4-20.

[2] **Y. Hong**, H. Bao, S. Gao, H. L. Ho, Y. Wang and W. Jin, “Hollow-core fiber cavity-enhanced photothermal spectroscopy for oxygen detection,” in *27th International Conference on Optical Fiber Sensors*, Alexandria, Virginia, USA, 2022, pp. Th1-3.

[3] **Y. Hong**, F. Chen, H. Bao, S. Gao, H. L. Ho, Y. Wang and W. Jin, “Sensitivity enhancement of photothermal gas detection via optical-phase-modulation amplification,” in *27th International Conference on Optical Fiber Sensors*, Alexandria, Virginia, USA, 2022, pp. F2-3. (Post-deadline)

[4] H. Bao, **Y. Hong**, W. Jin, H. L. Ho, S. Gao, Y. Wang, and P. Wang, “Highly sensitive and stable photothermal gas sensor with a hollow-core fiber Fabry-Perot cavity,” in *Optical Fiber Sensors Conference 2020 Special Edition*, 2020, pp. W1-4.

Table of Contents

List of Figures

List of Tables

List of Acronyms

AOM	acoustic-optic modulator
ARROW	anti-resonant reflecting optical waveguide
BD	balanced detector
BLS	broadband light source
CMDS	cavity mode-dispersion spectroscopy
DAS	direct absorption spectroscopy
DAQ	data-acquisition card
dB	decibel
DFB	distributed feedback
DMI	dual-mode interferometer
DOB	Delta over baseline
ECDL	external-cavity diode laser
EDFA	erbium-doped fiber amplifier

EOM	electro-optical modulator
FFT	fast Fourier transform
FG	function generator
FP	Fabry-Perot
FPI	Fabry-Perot interferometer
FRM	Faraday rotator mirror
FSR	free spectral range
HC-ARF	hollow-core anti-resonant fiber
HC-CTF	hollow-core conjoined-tube fiber
HC-NANF	hollow-core nested anti-resonant nodeless fiber
HC-PBF	hollow-core photonic bandgap fiber
HC-PCF	hollow-core photonic crystal fiber
HCF	hollow-core fiber
IM	intensity modulator
IRMS	isotope ratio mass spectrometers

LAS	Laser absorption spectroscopy
LC-PTI	low-coherence photothermal interferometry
LIA	lock-in amplifier
LPF	low-pass filter
MI	Michelson interferometer
MPD	mode phase difference
MZI	Mach-Zehnder interferometer
NEA	noise-equivalent-absorbance
NEC	noise-equivalent-concentration
NICE-OHMS	noise-immune cavity-enhanced optical heterodyne molecular spectroscopy
NIR	near-infrared
OBPF	optical band-pass filter
OFL	optical fiber laser
OPD	optical path difference
OPMA	optical phase-modulation amplification

OSA	optical spectrum analyzer
PA	photoacoustic
PC	polarization controller
PD	photodetector
PDH	Pound-Drever-Hall
PM	phase modulator
ppb	parts-per-billion
ppm	parts-per-million
ppq	part-per-quadrillion
ppt	parts-per-trillion
PT	photothermal
PTI	photothermal interferometry
p.p.	peak-to-peak
PTS	photothermal spectroscopy
PZT	piezoelectric transducer

RA	Raman amplifier
RI	refractive index
RIM	residual intensity modulation
RIN	relative intensity noise
RMS	root-mean-square
s.d.	standard deviation
SI	Sagnac interferometer
SMF	single-mode fiber
SNR	signal-to-noise ratio
SOA	semiconductor optical amplifier
TDFA	thulium-doped fiber amplifier
TDLAS	Tunable diode laser absorption spectroscopy
TECF	thermally expanded core fiber
UBT	urea breath test
WDM	wavelength division multiplexer

WMS	wavelength modulation spectroscopy

List of Symbols

α	absorption coefficient of gas molecules
α_0	absorption coefficient of pure gas
γ	coherence function
$\mathit{\Delta}\nu$	laser linewidth
Δf	detection bandwidth
ε	measurement precision
η	phase modulation coefficient
η_c	coupling efficiency
κ	thermal conductivity
ν_D	Doppler HWHM linewidth
ν_L	Lorentzian HWHM linewidth
ρ	density
σ	standard deviation value

τ	relaxation time
τ_c	coherence time of the laser
τ_d	time delay between the two arms of the interferometer
τ_n	non-radiative relaxation time
τ_r	radiative relaxation time
ω	angular modulation frequency
c	speed of light in a vacuum
C	gas concentration
C_V	specific heat
f_D	Doppler lineshape function
f_L	Lorentzian lineshape function
f_V	Voigt lineshape function
H	heating efficiency
h	Planck constant
k_B	Boltzmann constant

L_C	coherence length
N_m	molecular number density of an excited state
n	refractive index
n_{eff}	effective refractive index
Q	heat production
q	electron charge
R	reflectivity
R_{PD}	responsivity of the PD
r	reflection coefficient
S_0	spectral line strength
$S_p(f)$	power spectral density
t	transmission coefficient
V	visibility of interference

Chapter 1 Introduction

1.1 Background

Gas sensors have a wide range of applications in various fields such as environmental protection, medical diagnosis, energy and petrochemical monitoring, national defence and aerospace [1-3]. In the field of environmental protection, gas sensors are used for monitoring air quality and atmospheric pollutants. Gas sensors are also extensively used in medical diagnosis for the detection of exhaled breath gases and metabolites, which can aid in the diagnosis and monitoring of various diseases. In the energy and power sector, gas sensors are used to monitor trace gases in insulating oil, which helps to assess the working condition of transformers and maintain safe operation of power systems. In the petrochemical industry, gas sensors are used for real-time monitoring of various gases, such as methane (CH_4), nitrogen oxides (NO), and sulfur dioxide (SO_2), to ensure safe operation of the manufacturing process. In the national defence and aerospace sector, gas sensors are crucial for maintaining good ambient air quality in sealed compartments of spacecraft and for providing timely warning of gas leaks and equipment overheating failures. Overall, gas sensors play a vital role in ensuring safety, maintaining efficient operations, and safeguarding human health and the environment.

Traditional gas detection technologies are usually based on non-optical detection, such as semiconductor and electrochemical sensors, which are susceptible to cross-sensitivity with other gas components or adverse factors such as surface contamination of sensitive films [4, 5]. Laser absorption spectroscopy (LAS), on the other hand, uses the unique absorption spectra of gas molecules and the Beer-Lambert law to identify and measure gases, enabling high sensitivity and selectivity. Tunable diode laser absorption spectroscopy (TDLAS) is one of the most widely used techniques in this field [6]. While conventional TDLAS systems use a free-space gas cell composed of separated optical elements to measure gas characteristics, hollow-core fibers (HCFs) provide a feasible set of solutions for the miniaturization of spectral gas sensing systems [7]. Gas cells constructed with HCFs can significantly reduce system size and weight and simplify optical path alignment, making them unique in terms of flexibility, compactness, high reliability, low cost, resistance to electromagnetic interference, long-range measurement, and networking. LAS and its derivative spectroscopy based on HCFs have been rapidly developed since the end of the 20th century to achieve gas detection on the order of parts-per-million (ppm) to parts-per-billion (ppb) in volume concentration, and gradually become an important branch in gas sensing research [8].

However, to further enhance the detection performance of the sensors, new sensitive mechanisms need to be further explored, and new fiber optic gas cells need to be designed and fabricated. Therefore, this thesis aims to address the urgent needs of the applications by proposing novel optical fiber-based spectral gas sensing methods and systematically investigating the scheme and implementation techniques to enhance the sensor detection performance.

1.2 Literature review

1.2.1 Hollow-core fibers

HCFs are commonly used to achieve efficient light-gas interaction by tightly confining the optical mode within the fiber core over a long distance, which can be classified into two types, namely hollow-core photonic bandgap fibers (HC-PBFs) and hollow-core anti-resonant fibers (HC-ARFs) based on the light guiding mechanism.

In 1999, Russell et al. developed the first HC-PBF, which confines light inside the hollow core and utilizes the photonic bandgap principle to guide light [9]. A commercial HC-PBF with a core diameter of about 11 μm, a transmission center wavelength of 1550 nm, and a transmission bandwidth of about 200 nm has been developed. Several gases including acetylene (C_2H_2), ammonia (NH_3), CH_4, carbon dioxide (CO_2), carbon monoxide (CO), and hydrogen sulfide (H_2S) have absorption in this band [10]. The low-loss connection between the HC-PBF and the standard single-mode fiber (SMF) has also been achieved, making the gas cells with HC-PBFs easy to integrate into an optical system made of standard SMFs. An HC-PBF with a 20 μm core diameter was developed by Russell et al., which achieved low-loss transmission of about 1.72 dB/km at 1565 nm [11]. The acceptable bending loss of HC-PBFs can be achieved even with a bending radius of 1 cm, allowing the HCF to be coiled to achieve light-gas interaction over a long distance while maintaining a small gas volume [12].

In 2002, Russell et al. also developed the first Kagome hollow-core photonic crystal fiber (HC-PCF), which relies on the anti-resonance (or forbidden coupling) mechanism to guide light [13]. In 2010, Benabid et al. investigated the effect of the curvature of the air hole near the core on the transmission characteristics of micro-structured fibers and produced an hypocycloid-core Kagome HCF with low transmission loss and wide transmission band [14]. To continue reducing the transmission loss, in 2013, Dianov et al. proposed a nodeless HC-ARF [15]. The nodeless HC-ARF consists of a ring of thin-walled glass tubes that do not touch each other around an air core embedded in a quartz glass tube with a larger aperture to form a cladding. By an appropriate configuration of fiber parameters, the proportion of mode energy within the air core has the potential to attain an elevated 99.99% level [16]. In 2021, Poletti et al. developed an HC-ARF with a double-layer thin glass tube nesting structure, achieving a transmission loss as low as 0.22 dB/km at 1625 nm, which is comparable to the level of commercial solid quartz fibers [17].

The development of low-loss HCFs in the mid-infrared and visible wavelengths has also been well established. In 2010, Knight et al. successfully fabricated small-core HC-PCFs with a core range of 4.4 to 5.9 μm, which exhibited low-loss transmission over a wide frequency range of 500-700 nm [18]. In 2012, they further fabricated micro-structured HCFs with negative curvature in the transmission band beyond 4 μm, achieving a transmission loss of approximately 34 dB/km at an operating wavelength of 3.05 μm [19]. In 2011, Dianov et al. developed a nodeless HC-ARF with a low-loss transmission band extending beyond 3.5 μm by forming a negative curvature structure around the air hole in the HCF [20]. In 2014, Poletti et al. achieved a low-loss transmission of better than 130 dB/km in the 3.1 - 3.7 μm band using a large-aperture HC-PBF [21]. Benabid et al. prepared a hypocycloid-core Kagome HCF to achieve low-loss optical transmission in the broadband of 450-650 nm, with a transmission loss of about 70 dB/km at 600 nm [22]. In 2017, Wang et al. fabricated a nodeless HC-ARF with a core diameter of 26 μm, achieving ultra-wideband optical transmission from 440-1200 nm. The transmission loss at 532 nm was approximately 80 dB/km, while the bending loss at an 8-cm bending radius was approximately 0.2 dB/m [23].

1.2.2 Spectroscopic gas sensing with HCFs

The interaction between light and gases can lead to various physical processes, such as direct light absorption, photothermal (PT) /photoacoustic (PA) effects, and Raman scattering. These processes can alter the characteristic parameters of transmitted light in optical fibers, result in temperature and density changes, and produce Raman signals, which can be utilized to analyse gas species and accurately measure their concentrations.

In 2004, Hoo et al. reported the first spectroscopic gas sensor with HCFs, utilizing a HC-PBF to measure the diffusion of C_2H_2 through direct absorption spectroscopy (DAS) [24]. In the same year, Ritari et al. utilized a fiber optic gas cell with a HC-PBF to measure the absorption spectra of gases, including CH_4, C_2H_2, NH_3, and Hydrogen Cyanide (HCN), using a broadband light source (BLS) [25]. Benabid et al. achieved locking the wavelength of a semiconductor laser to the absorption line of C_2H_2 using a HC-PCF in 2005 [26]. While gas sensing with HC-PBFs has been demonstrated with several gases such as C_2H_2, CH_4, ethane (C_2H_6), and oxygen (O_2) [27-29], the sensitivity of HCF-based spectroscopic gas sensors remained in the tens of ppm level for a long time, which is inadequate for many practical applications.

Photothermal interferometry (PTI) has proven to be a highly effective method for detecting trace gases using HCFs. The first high-sensitivity gas sensor using PTI with HCFs was reported in 2015 by Jin et al., demonstrating ppb sensitivity for C_2H_2 using a 10-meter-long HC-PBF [7]. The PTI method measures the phase modulation of a probe beam resulting from absorption of a modulated pump beam, with the PT phase modulation amplitude proportional to the gas concentration, pump power, and HCF length. Subsequently, a PT gas sensor using the Fabry-

Perot interferometer (FPI) with a 2-cm-long HC-PBF was demonstrated to achieve a response time of less than 19 s for faster gas sensing [30]. A variety of fiber optic interferometric configurations have been used to achieve gas detection with noise-equivalent-concentration (NEC) down to ppb and even parts-per-trillion (ppt) levels for different gas species [31-36]. Heterodyne PTI with a 5.26 μm pump and 100-s integration time was able to detect NO down to single-ppb level [37]. Moreover, the mode phase difference (MPD) in a dual-mode HCF was utilized to detect acetylene down to ppt level using ~5-m-long HCF by exploiting the noise cancellation property of the MPD, which is sensitive to absorption-induced PT phase modulation in the hollow core but insensitive to external environmental perturbations, resulting in a remarkable enhancement of signal-to-noise ratio (SNR) [38]. Overall, compared to HCF gas sensors based on DAS, PTI has significantly improved the sensitivity.

1.3 Motivation of this work

PTI is a highly sensitive spectroscopic technique for trace gas detection. The PTI gas sensors with HCF gas cells have demonstrated detection sensitivity in ppb levels in the near-infrared (NIR) region in laboratory environment. Nevertheless, the performance of the state-of-the-art laser spectroscopic sensors is still inadequate for specific applications necessitating high sensitivity and stability for gas species that do not have strong absorption in the NIR.

Some gases like oxygen exhibit weak absorption in the NIR spectrum. To sensitively detect oxygen with FPI, we propose a visible-pump and NIR-probe scheme, capitalizing on the robust oxygen absorption in the visible range and the well-established telecom fiber optic components within the NIR domain. Increasing the length of HCF could enhance the magnitude of the PT phase modulation. However, the FPI is intrinsically an unbalanced interferometer, which limits system performance by converting phase noise into intensity noise at the FPI output if the HCF used is too long. Hence, we propose a high-finesse Fabry-Perot (FP) cavity with a short HCF to improve the sensitivity for oxygen detection. The high-finesse cavity enhances the detected signal converted from the PT phase modulation by a factor proportional to the cavity finesse, resulting in better performance compared to the low-finesse FPI scheme. Comprehensive modelling for PT phase modulation in HCF by considering thermal relaxation of oxygen and thermal conduction has been carried out, and oxygen detection experiments have been conducted.

The implementation of PT-FPI systems up to now involves a narrow-linewidth laser for probing, which can cause parasitic interferences resulting from reflections and backward scatterings. This may cause variation in interference fringe visibility, result in fluctuations in the operating point of the optical interferometer and hence limit the measurement precision. To address this issue, we propose fiber optic low-coherence (LC) PTI for gas detection with ultra-high precision and stability, employing a broadband probe source with a short coherence length to suppress parasitic interference. We carry out theoretical analysis for the parasitic interference of the PTI system powered by broadband and narrow-linewidth probe and find that LC-PTI provides a much better measurement precision and long-term stability compared with the traditional PTI with a coherent laser source.

To further improve the gas detection sensitivity, we demonstrate an optical phase-modulation amplification (OPMA) by using an HCF resonating cavity and a dual-mode interferometer (DMI), respectively. By locking the probe wavelength to the resonance of a high-finesse FP cavity, the PT phase modulation is amplified by a factor of the cavity finesse. Detection of the amplified phase modulation with optical fiber interferometry enables gas sensors with remarkably improved performance. By use of an HCF FP gas cell with a moderate finesse at the probe wavelength and pump sources of different wavelengths, we demonstrate ultra-sensitive detection of methane, acetylene, and oxygen. To avoid the complex wavelength locking, we further investigate the OPMA by operating a DMI at destructive interference and use this effect to improve the sensitivity of gas detection. The effects of OPMA on signal and noise levels are studied theoretically and experimentally. With OPMA using a DMI, detection of carbon dioxide with high sensitivity and large dynamic range is demonstrated. The OPMA with an HCF resonating cavity or an optical fiber DMI can be readily used to improve the sensitivity of other phase modulation-based sensors.

1.4 Outline

The structure of the thesis is as follows:

In Chapter 1, the research background of HCF-based gas sensors is introduced. The current development of HCFs is reviewed and the research status of spectroscopic gas sensing with HCFs is outlined. The significance and the content of the thesis are presented.

In Chapter 2, the elements of laser spectroscopy for gas sensing are reviewed, including absorption spectroscopy of gases, wavelength modulation spectroscopy (WMS) and photothermal spectroscopy (PTS). An introduction of HCFs is also presented.

In Chapter 3, the PT phase modulation in gas-filled HCFs is studied theoretically, including heat source, heat conduction and PT phase modulation. The different interferometric configurations for detecting the PT phase modulation are presented and the noise sources in PTI are presented.

In Chapter 4, the performance optimization of the HCF FPI for oxygen detection is carried out. With a low-finesse FPI, experiments of detecting oxygen are demonstrated. To further improve the sensitivity, we optimize the reflectivity of the mirrors coated on SMFs and demonstrate the sensitive oxygen detection. Using a high-finesse FP cavity with a short HCF, experiments of tracing oxygen are further demonstrated with high sensitivity and stability.

In Chapter 5, the fiber optic LC-PTI is presented. Experiments of detecting acetylene and its isotope ratios are demonstrated with high precision and remarkable stability. The measurement precision of the PTI system powered by narrow linewidth probe and broadband laser source is compared, based on a discussion of parasitic interferences.

In Chapter 6, the OPMA of an HCF FP cavity is firstly presented. Ultra-sensitive detection of methane, acetylene, and oxygen are demonstrated, respectively. The OPMA of a DMI operating at destructive interference is also investigated. Experiments of detecting carbon dioxide and its isotope ratios with high sensitivity are demonstrated. The amplifying effect on PT phase modulation is discussed theoretically and experimentally and the noise analysis is also performed.

In Chapter 7, the works in this thesis are summarized and the future research directions are suggested.

Reference of Chapter 1

1. M. A. Gondal, "Laser photoacoustic spectrometer for remote monitoring of atmospheric pollutants," Applied Optics **36**, 3195-3201 (1997).
2. M. G. Allen, "Diode laser absorption sensors for gas-dynamic and combustion flows," Measurement Science and Technology **9**, 545-562 (1998).

3. D. Smith, and P. Spanel, "The challenge of breath analysis for clinical diagnosis and therapeutic monitoring," Analyst **132**, 390-396 (2007).

4. N. Yamazoe, "New approaches for improving semiconductor gas sensors," Sensors and actuators B: Chemical **5**, 7-19 (1991).

5. J. W. Fergus, "Materials for high temperature electrochemical NOx gas sensors," Sensors and Actuators B: Chemical **121**, 652-663 (2007).

6. P. Werle, R. Mücke, and F. Slemr, "The limits of signal averaging in atmospheric trace-gas monitoring by tunable diode-laser absorption spectroscopy (TDLAS)," Applied Physics B **57**, 131-139 (1993).

7. W. Jin, Y. Cao, F. Yang, and H. L. Ho, "Ultra-sensitive all-fibre photothermal spectroscopy with large dynamic range," Nat Commun **6**, 6767 (2015).

8. W. Jin, H. Bao, P. Zhao, Y. Zhao, Y. Qi, C. Wang, and H. L. Ho, "Recent Advances in Spectroscopic Gas Sensing With Micro/Nano-Structured Optical Fibers," Photonic Sensors (2021).

9. R. Cregan, B. Mangan, J. Knight, T. Birks, P. S. J. Russell, P. Roberts, and D. Allan, "Single-mode photonic band gap guidance of light in air," science **285**, 1537-1539 (1999).

10. W. Jin, H. Ho, Y. Cao, J. Ju, and L. Qi, "Gas detection with micro-and nano-engineered optical fibers," Optical Fiber Technology **19**, 741-759 (2013).

11. B. Mangan, L. Farr, A. Langford, P. J. Roberts, D. P. Williams, F. Couny, M. Lawman, M. Mason, S. Coupland, and R. Flea, "Low loss (1.7 dB/km) hollow core photonic bandgap fiber," in *Optical Fiber Communication Conference*(Optica Publishing Group2004), p. PD24.

12. T. P. Hansen, J. Broeng, C. Jakobsen, G. Vienne, H. R. Simonsen, M. D. Nielsen, P. M. Skovgaard, J. R. Folkenberg, and A. Bjarklev, "Air-guiding photonic bandgap fibers: spectral properties, macrobending loss, and practical handling," Journal of Lightwave Technology **22**, 11-15 (2004).

13. F. Benabid, J. C. Knight, G. Antonopoulos, and P. S. J. Russell, "Stimulated Raman scattering in hydrogen-filled hollow-core photonic crystal fiber," Science **298**, 399-402 (2002).

14. Y. Wang, N. V. Wheeler, F. Couny, P. Roberts, and F. Benabid, "Low loss broadband transmission in hypocycloid-core Kagome hollow-core photonic crystal fiber," Optics letters **36**, 669-671 (2011).

15. A. N. Kolyadin, A. F. Kosolapov, A. D. Pryamikov, A. S. Biriukov, V. G. Plotnichenko, and E. M. Dianov, "Light transmission in negative curvature hollow core fiber in extremely high material loss region," Optics express **21**, 9514-9519 (2013).

16. S. Gao, Y. Wang, and P. Wang, "Research progress on hollow-core anti-resonant fiber and gas raman laser technology," Chin. J. Lasers **46**, 183-200 (2019).

17. H. Sakr, T. D. Bradley, G. T. Jasion, E. N. Fokoua, S. R. Sandoghchi, I. A. Davidson, A. Taranta, G. Guerra, W. Shere, and Y. Chen, "Hollow core NANFs with five nested tubes

and record low loss at 850, 1060, 1300 and 1625nm," in *Optical Fiber Communication Conference*(Optica Publishing Group2021), p. F3A. 4.

18. P. J. Mosley, W. Huang, M. G. Welch, B. J. Mangan, W. J. Wadsworth, and J. C. Knight, "Ultrashort pulse compression and delivery in a hollow-core photonic crystal fiber at 540 nm wavelength," Optics letters **35**, 3589-3591 (2010).

19. F. Yu, W. J. Wadsworth, and J. C. Knight, "Low loss silica hollow core fibers for 3–4 μm spectral region," Optics express **20**, 11153-11158 (2012).

20. A. D. Pryamikov, A. S. Biriukov, A. F. Kosolapov, V. G. Plotnichenko, S. L. Semjonov, and E. M. Dianov, "Demonstration of a waveguide regime for a silica hollow-core microstructured optical fiber with a negative curvature of the core boundary in the spectral region> 3.5 μm," Optics express **19**, 1441-1448 (2011).

21. N. V. Wheeler, A. M. Heidt, N. K. Baddela, E. N. Fokoua, J. R. Hayes, S. R. Sandoghchi, F. Poletti, M. N. Petrovich, and D. J. Richardson, "Low-loss and low-bend-sensitivity mid-infrared guidance in a hollow-core–photonic-bandgap fiber," Optics Letters **39**, 295-298 (2014).

22. B. Debord, M. Alharbi, A. Benoit, D. Ghosh, M. Dontabactouny, L. Vincetti, J.-M. Blondy, F. Gérôme, and F. Benabid, "Ultra low-loss hypocycloid-core Kagome hollow-core photonic crystal fiber for green spectral-range applications," Optics Letters **39**, 6245-6248 (2014).

23. S.-f. Gao, Y.-y. Wang, X.-l. Liu, C. Hong, S. Gu, and P. Wang, "Nodeless hollow-core fiber for the visible spectral range," Optics letters **42**, 61-64 (2017).

24. Y. Hoo, W. Jin, H. Ho, J. Ju, and D. Wang, "Gas diffusion measurement using hollow-core photonic bandgap fiber," Sensors and Actuators B: Chemical **105**, 183-186 (2005).

25. T. Ritari, J. Tuominen, H. Ludvigsen, J. Petersen, T. Sørensen, T. P. Hansen, and H. R. Simonsen, "Gas sensing using air-guiding photonic bandgap fibers," Optics Express **12**, 4080-4087 (2004).

26. F. Benabid, F. Couny, J. Knight, T. Birks, and P. S. J. Russell, "Compact, stable and efficient all-fibre gas cells using hollow-core photonic crystal fibres," Nature **434**, 488-491 (2005).

27. A. Cubillas, M. Silva-Lopez, J. Lazaro, O. Conde, M. Petrovich, and J. Lopez-Higuera, "Methane detection at 1670-nm band using a hollow-core photonic bandgap fiber and a multiline algorithm," Optics Express **15**, 17570-17576 (2007).

28. X. Li, J. Liang, S. Lin, Y. Zimin, Y. Zhang, and T. Ueda, "NIR spectrum analysis of natural gas based on hollow-core photonic bandgap fiber," IEEE Sensors Journal **12**, 2362-2367 (2012).

29. D. Munzke, M. Böhm, and O. Reich, "Gaseous oxygen detection using hollow-core fiber-based linear cavity ring-down spectroscopy," Journal of Lightwave Technology **33**, 2524-2529 (2015).

30. F. Yang, Y. Tan, W. Jin, Y. Lin, Y. Qi, and H. L. Ho, "Hollow-core fiber Fabry–Perot photothermal gas sensor," Optics letters **41**, 3025-3028 (2016).

31. H. Bao, Y. Hong, W. Jin, H. L. Ho, C. Wang, S. Gao, Y. Wang, and P. Wang, "Modeling and performance evaluation of in-line Fabry-Perot photothermal gas sensors with hollow-core optical fibers," Opt Express **28**, 5423-5435 (2020).

32. F. Chen, S. Jiang, W. Jin, H. Bao, H. L. Ho, C. Wang, and S. Gao, "Ethane detection with mid-infrared hollow-core fiber photothermal spectroscopy," Opt Express **28**, 38115-38126 (2020).

33. C. Yao, S. Gao, Y. Wang, P. Wang, W. Jin, and W. Ren, "MIR-Pump NIR-Probe Fiber-Optic Photothermal Spectroscopy With Background-Free First Harmonic Detection," IEEE Sensors Journal **20**, 12709-12715 (2020).

34. G. Gomolka, M. Krajewska, A. M. Khegai, S. V. Alyshev, A. S. Lobanov, S. V. Firstov, D. Pysz, G. Stepniewski, R. Buczynski, M. Klimczak, and M. Nikodem, "Heterodyne photothermal spectroscopy of methane near 1651 nm inside hollow-core fiber using a bismuth-doped fiber amplifier," Applied Optics **60**, C84-C91 (2021).

35. K. Krzempek, P. Jaworski, P. Kozioł, and W. Belardi, "Antiresonant hollow core fiber-assisted photothermal spectroscopy of nitric oxide at 5.26 μm with parts-per-billion sensitivity," Sensors and Actuators B: Chemical **345** (2021).

36. J. P. Waclawek, H. Moser, and B. Lendl, "Balanced-detection interferometric cavity-assisted photothermal spectroscopy employing an all-fiber-coupled probe laser configuration," Opt Express **29**, 7794-7808 (2021).

37. K. Krzempek, "Part-per-billion level photothermal nitric oxide detection at 5.26 microm using antiresonant hollow-core fiber-based heterodyne interferometry," Opt Express **29**, 32568-32579 (2021).

38. P. Zhao, Y. Zhao, H. Bao, H. L. Ho, W. Jin, S. Fan, S. Gao, Y. Wang, and P. Wang, "Mode-phase-difference photothermal spectroscopy for gas detection with an anti-resonant hollow-core optical fiber," Nat Commun **11**, 847 (2020).

Chapter 2 Elements of laser spectroscopy for gas sensing

In the present chapter, we endeavour to lay the groundwork for understanding the critical concepts underpinning spectroscopic gas sensing via HCFs. To commence, we endeavour to delineate the core principle undergirding absorption spectroscopy, thereby setting the stage for more complex discussions. Thereafter, we turn our focus towards explicating the elementary principles intrinsic to WMS and PTS, before concluding with an exposition on HCFs.

2.1 Theory of absorption spectroscopy

2.1.1 Light-gas interaction

Gas molecules are composed of bonded atoms, and they can oscillate or rotate at a particular frequency denoted as the natural frequency. These frequencies typically correspond to the range of infrared light. Vibrational or rotational modes that induce alterations in the dipole moment of the molecules in the vicinity of the equilibrium position are designated as infrared-active modes. This implies that these specific frequencies are susceptible to absorption by infrared light.

A schematic representation of absorption spectroscopy is presented in Fig. 2.1. Incident photons possessing a particular frequency may be absorbed by the molecule when the energy of the photon precisely matches the energy difference between the higher and lower energy states of the molecule, which is typically identified as absorption. Following absorption, a phenomenon known as non-radiative relaxation can transpire, whereby molecules transition from an elevated energy state to a diminished energy state without the emission of a photon. Consequently, the energy that had initially been absorbed is converted into the molecule's translational energy. This transformation effectuates an elevation in the sample's temperature.

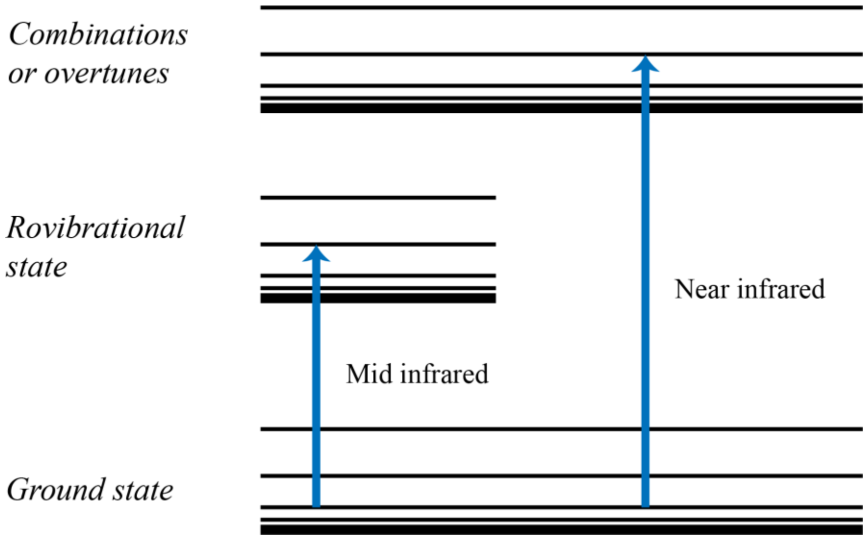

Fig. 2.1 The energy state schematic representation within absorption spectroscopy.

According to quantum mechanics, the energy state of a molecule is confined to a series of distinct, non-continuous values, commonly referred to as energy levels. The total energy inherent in a gaseous molecule can be conceptualized as an aggregation of its diverse components, including electronic, vibrational, rotational, nuclear, and translational energies. The required energy for different types of level transitions has the following relationships.

Vibrational transitions typically occur with rotational transitions, while electronic transitions occur with ro-vibrational transitions. Transitions between rotational energy levels typically manifest within the microwave region of the electromagnetic spectrum. Conversely, transitions incorporating both rotational and vibrational energy levels predominantly correspond to the mid-infrared region of the spectrum. Overtone or combination bands can be also formed from vibrational and rotational modes, which typically lie in the NIR region. Electronic level transitions correspond to the ultraviolet/visible region.

Vibrational and rotational modes pertain to the repetitive physical dynamics of molecules. In the context of polyatomic molecules encompassing more than two atoms, a multitude of vibrational modes are presented, which are also commonly referred to as degrees of freedom [1]. For a linear polyatomic molecule consisting of N atoms, a total of $3N$ coordinates are required to determine the molecule's position and direction, i.e., $3N$ degrees of freedom. The summative number of degrees of freedom parallels the aggregate of the coordinates necessitated for elucidating the motion of the molecule's center of mass, rotation, and vibration. For translational motion, three coordinates are required to determine the position of the molecule. For rotational motion, a linear molecule requires two angles to be determined, while a non-linear molecule requires three angles to be determined. As for vibrational motion, the vibrational degrees of freedom of a linear multi-atomic molecule can be represented by $3N-5$, and that of a non-linear multi-atomic molecule is $3N-6$.

Fig. 2.2 depicts a schematic diagram of the ro-vibrational transitions and the corresponding spectra. The asymmetry of the absorption spectra of actual diatomic molecules is due to the presence of complex factors such as non-rigid rotation, non-harmonic vibration, and vibration-rotation coupling.

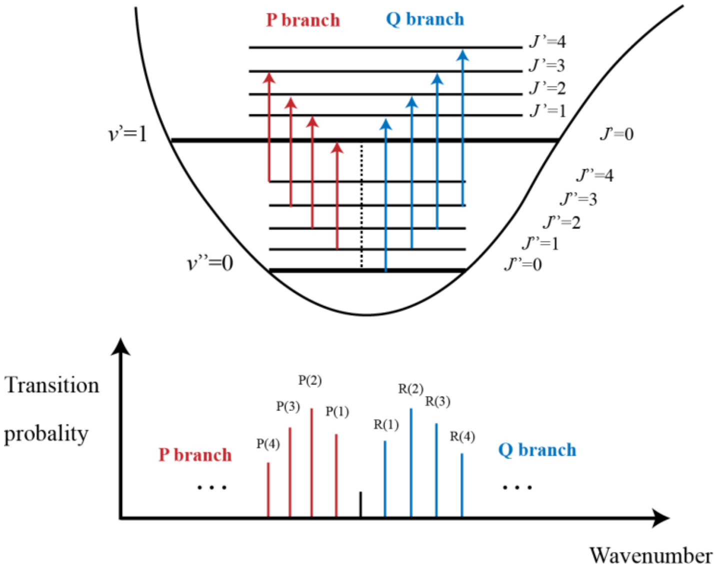

Fig. 2.2 Schematic diagram of the ro-vibrational transitions and the corresponding spectra [2].

In the vibrational spectrum of multi-atomic molecules, the shift from the foundational vibrational status to the initial elevated vibrational state ($\Delta v=1$) in the i-th vibrational mode is called the fundamental frequency transition v_i. However, due to the inherent anharmonicity of vibrations, transitions with $\Delta v=e(e>1)$ are also possible, which are called overtone transitions. Overtone transitions include the first overtone transition ($2v_i,\ \Delta v = 2$), the second overtone transition ($3v_i,\ \Delta v = 3$), and so on. In addition, when two or more fundamental or overtone transitions manifest concurrently, combination transitions can be observed (e.g., $v_1 + v_2, \Delta v_1 = \Delta v_2 = 1$), but their spectral intensities are much weaker than those of the fundamental transitions. Overtone absorption bands are typically located in the NIR region of the spectrum, while fundamental absorption bands are usually found in the mid-infrared region.

2.1.2 Beer-Lambert law

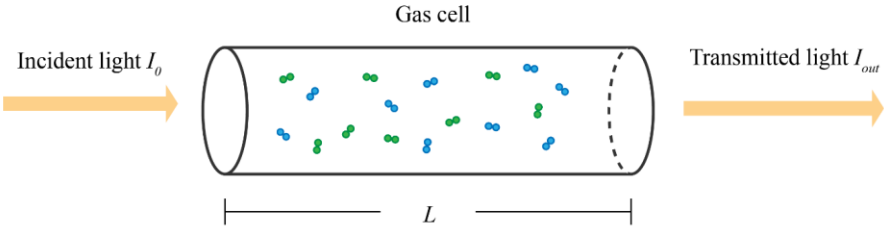

Fig. 2.3 Illustrative diagram of absorption spectroscopy.

As elucidated in Fig. 2.3, the propagation of a laser beam through a cell containing gaseous matter leads to the absorption of laser energy by the gas. This results in a subsequent diminution of the intensity of light transmitted. The transmitted light intensity can be described by Beer-Lambert's law, expressed as:

$$I_{out}(v) = I_0 e^{-\alpha(v)L} \tag{2.1}$$

where I_0 represents the light intensity of the incident light, $\alpha(\nu)$ represents the absorption coefficient of gas molecules at a specified wavenumber ν, and L is the length of the gas cell. The gas absorption coefficient $\alpha(\nu)$ can be expressed as:

$$\alpha(\nu) = CN_{tot}S_0 f(\nu) = \alpha_0(\nu)C \tag{2.2}$$

which is related to the gas concentration C, spectral line strength S_0, and line shape $f(\nu)$. Here, $C = N/N_{tot}$ is the concentration of the absorbing gaseous substance, N is the quantity of molecules of absorbing gas, N_{tot} is the total number of molecules. $\alpha_0(\nu) = N_{tot}S_0 f(\nu)$ is the absorption coefficient of gas molecules for 100% concentration.

Given specific conditions of temperature T and pressure P, the total quantity of gas molecules N_{tot} can be formulated as:

$$N_{tot} = \frac{P}{k_B T} \tag{2.3}$$

where k_B is the Boltzmann constant. At standard temperature and pressure, $N_{tot} = 2.479 \times 10^{19}\ \mathrm{mol \cdot cm^{-3}}$.

The actual molecular absorption spectrum is not composed of infinitely sharp lines, but has a certain width. Spectral broadening can be classified into two categories: homogeneous broadening and inhomogeneous broadening. A single atom or molecule is neither homogeneous nor inhomogeneous, but the spectrum often reflects the behaviour of a group of particles. The mechanism of homogeneous broadening is the same for the spectral line shape of each particle in the ensemble, regardless of whether the system consists of a single particle, multiple particles, or a group of particles. In contrast, inhomogeneous broadening refers to the existence of local physical environments that differ for each particle, resulting in very slight differences in the spectral line position of each particle. The superposition of spectra from particles with slight differences results in the ensemble spectrum. The physical mechanisms of spectral broadening mainly include natural broadening, Doppler broadening, and collisional broadening. Natural broadening arises due to the limited duration of the excited state and is classified as a variety of homogeneous broadening. Doppler broadening originates from the velocity distribution of particles, and because the frequency change produced by each particle is different due to their different velocities, Doppler broadening is a type of inhomogeneous broadening. Collisional broadening refers to collisions between particles and their surrounding particles, which shorten the excited state lifetime and cause spectral broadening. Collisional broadening is related to temperature, pressure, and gas type and is a type of homogeneous broadening.

Homogeneous broadening is represented by the Lorentzian line shape, while inhomogeneous broadening is represented by the Gaussian line shape. The actual molecular spectral line shape is the convolution between the Lorentzian lineshape function f_L and Doppler lineshape function f_D, known as the Voigt profile f_V, expressed as:

$$f_L(\nu) = \frac{\nu_L}{\pi} \frac{1}{(\nu - \nu_0)^2 + {\nu_L}^2} \tag{2.4}$$

$$f_D(\nu) = \frac{1}{\nu_D} \sqrt{\frac{ln2}{\pi}} \exp\,[-ln2 \cdot (\frac{\nu - \nu_0}{\nu_D})^2] \tag{2.5}$$

$$f_V(\nu) = \int_{-\infty}^{+\infty} f_L(\nu' - \nu_0) f_D(\nu - \nu')\, d\nu' \tag{2.6}$$

where ν_L and ν_D are the Lorentzian linewidth and Doppler linewidth at half-width and half-maximum, respectively, and ν_0 is the wavenumber of the absorption line.

Under the weak absorption approximation $\alpha(\nu)L \ll 1$, the light intensity absorbed by the gas can be deduced from Eq. (2.1) and written as:

$$I = I_0 - I_{out} = I_0\left(1 - e^{-\alpha(\nu)L}\right) \approx \alpha(\nu) L I_0 = \alpha_0(\nu) C L I_0 \propto C \tag{2.7}$$

Since the absorbed light intensity is related to the gas concentration C, the gas concentration can be obtained through the detection of the power decay of the probing light or the intensity of the thermal or acoustic effects accompanying gas absorption.

2.2 Wavelength modulation spectroscopy

Within the realm of laser spectroscopy, the utilization of modulation techniques is essential for achieving precision and high sensitivity measurements. Two widely utilized modulation techniques in this field are wavelength modulation and frequency modulation, each providing distinct advantages in the reduction of low-frequency noise. While frequency modulation techniques have demonstrated lower detection limits, for our present research demands, wavelength modulation techniques are deemed more suitable. Consequently, we have decided to employ wavelength modulation in our studies.

A schematic representation of the WMS technique is illustrated in Fig. 2.4. This technique involves applying a high-frequency sinusoidal modulation (typically tens of kilohertz) to the wavelength of the laser beam. The central laser wavelength undergoes a progressive alteration across the absorption line distinctive to the target molecule, resulting in a harmonic signal due to the interaction between the modulated light and the absorption feature. To extract the signal of interest, a lock-in amplifier (LIA) is utilized for efficient demodulation.

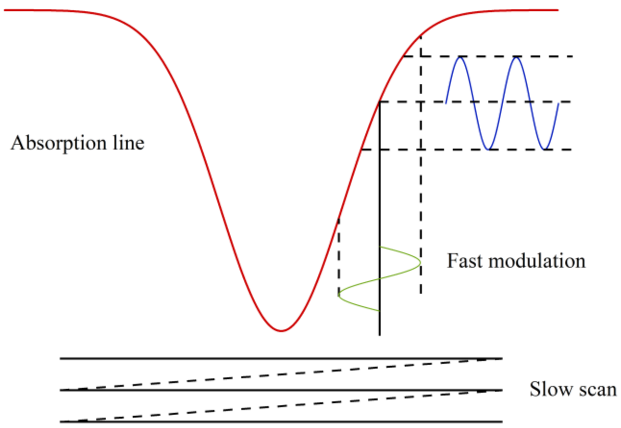

Fig. 2.4 Schematic of WMS.

When a sinusoidal modulation of the frequency f_m is applied to the injection current, the wavenumber could be expressed as:

$$\nu(t) = \nu_c + \nu_a cos(2\pi f_m t) \tag{2.8}$$

where ν_c is the center laser wavenumber, which is swept at slow frequency, and ν_a is the modulation amplitude. Since most of the absorption spectroscopy is carried out at room temperature and standard atmospheric pressure, the Voigt line shape of gas molecules approaches Lorentz profile. The normalized laser wavenumber could be defined as:

$$\begin{aligned} \bar{\nu} &= (\nu(t) - \nu_0)/\nu_L \\ &= \big((\nu_c - \nu_0) + \nu_a cos(2\pi f_m t)\big)/\nu_L \\ &= \bar{\nu_c} + m cos(2\pi f_m t) \end{aligned} \tag{2.9}$$

where $\bar{\nu_c} = (\nu_c - \nu_0)/\nu_L$ is the normalized wavenumber deviation from the line center, $m = \nu_a/\nu_L$ is the modulation depth. The absorption coefficient, characterized by a Lorentzian lineshape, can be depicted as:

$$\alpha(\nu) = \alpha_0(\nu) C \frac{1}{1 + (\frac{\nu - \nu_0}{\nu_L})^2} \tag{2.10}$$

By inserting Eq. (2.9) into Eq. (2.10), since $\alpha(\nu)$ is an even function, the representation of this coefficient could be deconstructed into a succession of Fourier series [3]:

$$\alpha(\bar{v}) = \alpha_0 C\left[H_0 + \sum_{n=1}^{\infty} H_n \cos(2n\pi f_m t)\right] \tag{2.11}$$

$$H_0 = \frac{1}{\pi}\int_0^{\pi} \frac{1}{1+[\bar{v}_c + m\cos(\theta)]^2} d\theta \tag{2.12}$$

$$H_n = \frac{2}{\pi}\int_0^{\pi} \frac{\cos(n\theta)}{1+[\bar{v}_c + m\cos(\theta)]^2} d\theta \ (n \geq 1) \tag{2.13}$$

where H_0 and H_n denote the harmonic coefficients, and n indicates the n-th order of harmonics.

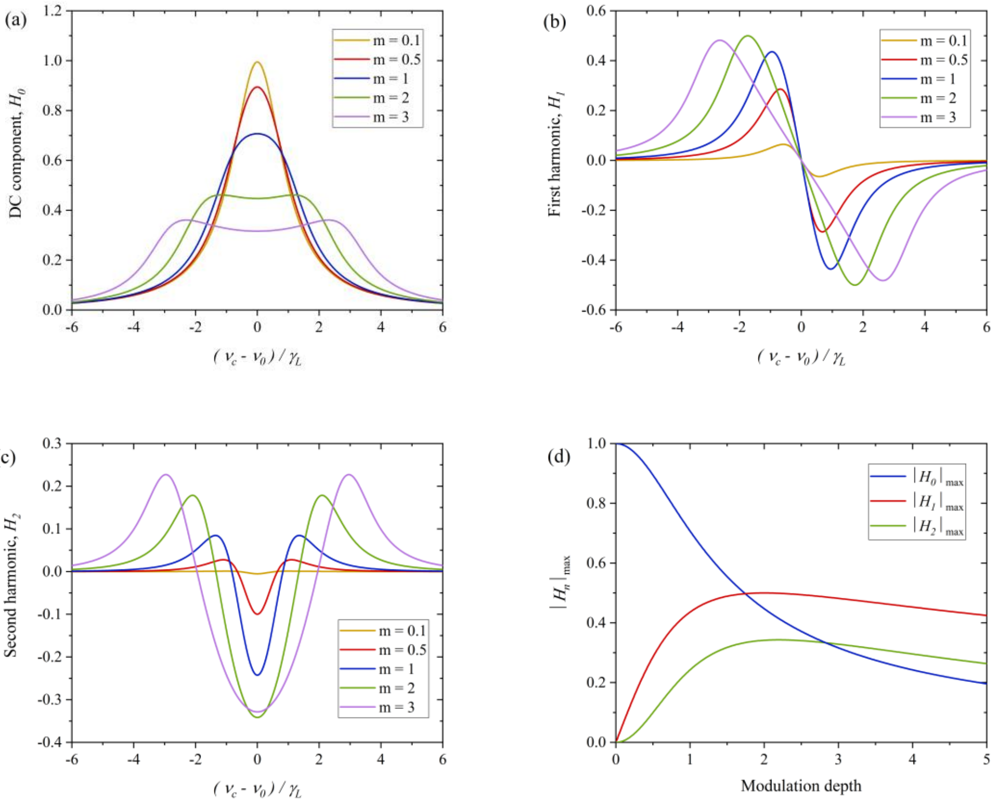

Fig. 2.5 The harmonic coefficients with variations in the modulation depth.

Fig. 2.5 depicts the harmonic coefficients computed with variations in the modulation depth. It can be observed that the coefficients pertaining to the even-order reveal a peak at the central location of the absorption line, while their odd-order counterparts equal zero. The most important harmonics are the first and second harmonics. Their maximum values are depended on the modulation depth. The first harmonic coefficient attains its maximum value at the line center for a modulation depth of approximately 2, after which it decreases gradually upon further modulation depth increase. And the second harmonic coefficient achieves its maximum value when the modulation depth is 2.2.

By inserting Eq. (2.11) – (2.13) into Eq. (2.7), assuming that $\alpha L \ll 1$ and neglecting the higher-order terms, we may obtain the approximation expression of the first and second harmonic output signal:

$$I_{1,2} = H_{1,2}\, \alpha_0 C L I_0 \propto C \tag{2.14}$$

Thus, through Eq. (2.14), we can calculate the gas concentration from the first or second harmonic signal.

2.3 Photothermal spectroscopy

PTS is a highly sensitive technique employed for measuring the optical absorption and thermal properties of a specimen. The fundamental processes responsible for generating the signal in PTS are depicted in Fig. 2.6. The sample is excited by optical radiation and absorbs some of the incident energy, thereby augmenting its internal energy. This energy is dissipated via relaxation, engendering a change in the temperature of the sample. Provided that the PT-induced temperature alteration transpires at a faster pace than the requisite time for gas expansion or contraction, it culminates in a change in pressure, which further propels as an acoustic wave. Subsequent to the relaxation of pressure to its equilibrium state, a variation in density, commensurate with the temperature, persists. These changes in temperature and density influence other attributes of the sample, which are measured through PTS. In particular, sensitive PT techniques rely on the measurement of the refractive index (RI) variation prompted by fluctuations in the sample's temperature and density.

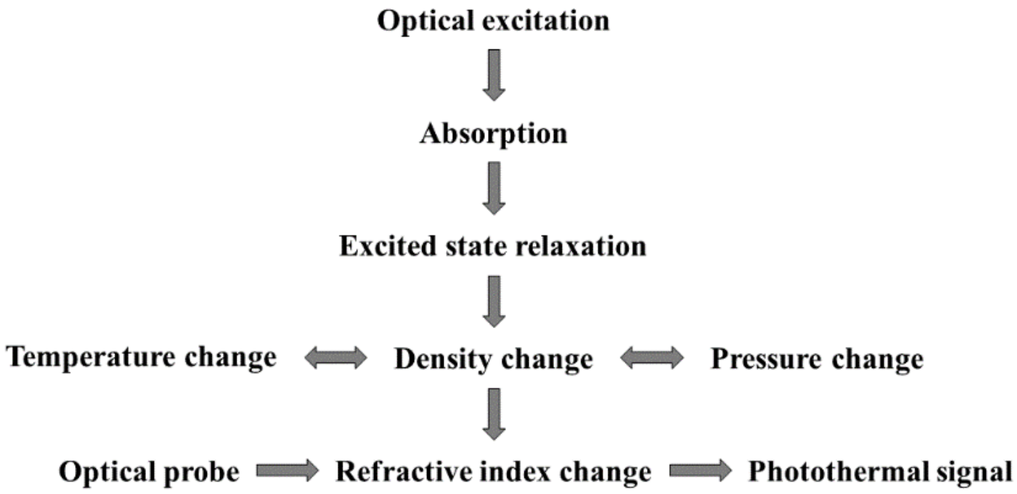

Fig. 2.6 The fundamental processes in PTS [4].

The fundamental principle of PTS is based on the change in thermal state resulting from the absorption of radiation by the sample [4]. The process of optical absorption involves the excitation of an absorbing species, thereby augmenting the internal energy of the absorber that is equivalent to the energy of the incident photon. Oftentimes, relaxation of the excited state leads to a heat generation in the sample, with the thermal energy being equal to that of the absorbed photon. Nonetheless, the heating process is not immediate and can occur at various rates. Slowly produced heat may not yield detectable PT signals. The relaxation of the excited state might involve multiple mechanisms, with each energy transfer typically occurring at a distinct rate. The time scales associated with excited-state relaxation range from femtoseconds to seconds [5-7].

The prediction of relaxation steps for a vibrationally excited species is facilitated by the trends in vibrational, rotational, and translational relaxation [4]. A schematic representation of the mechanism underlying the relaxation of vibrationally excited species is depicted in Fig. 2.7. The utilization of laser sources to achieve vibrational excitation can result in the excitation of specific ro-vibrational state species to upper vibrational levels, generating a singular ro-vibrational excited state with a hole present in the initial rotational state. Subsequent to excitation, relaxation processes including rotation to rotation (R-R), rotation to translation (R-T), and translation to translation (T-T) relaxation are initiated. The relaxation of the excited state via R-R processes leads to the distribution of ro-vibrational states into a canonical distribution. Concurrently, in the ground state, rotational hole filling transpires, while in the excited state, a dissipation of rotational states occurs. Subsequent to relatively faster R-R/T and

T-T relaxation stages, vibration to vibration (V-V) relaxation occurs. V-V relaxation leads to the establishment of a quasi-equilibrium state within the excited vibrational levels. Finally, the vibrational levels excited revert to the ground state via vibration to rotation (V-R) and vibration to translation (V-T) processes.

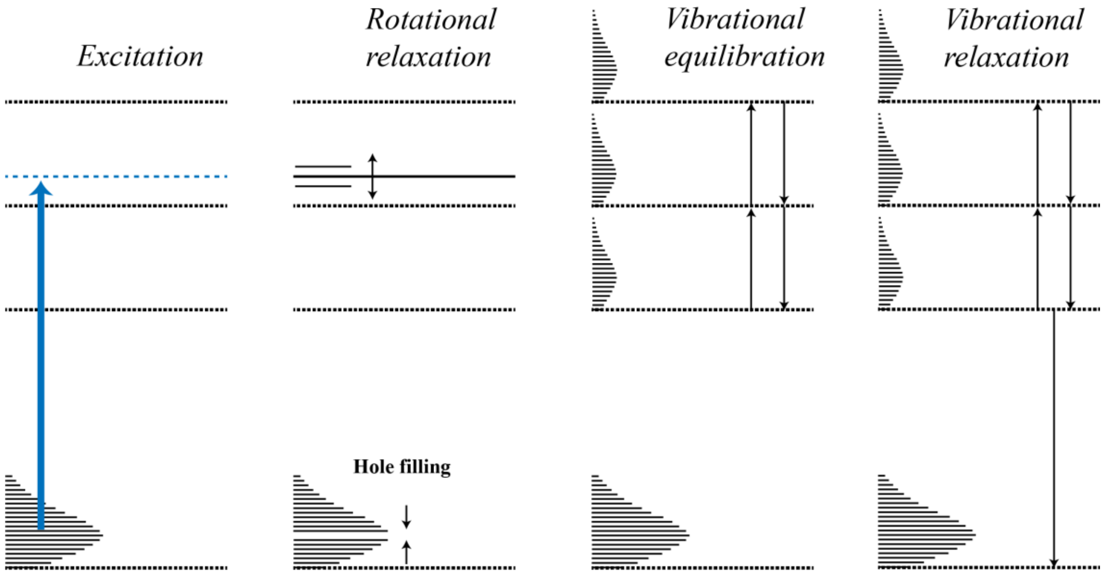

Fig. 2.7 Schematic diagram of the relaxation processes associated with ro-vibrational excitation.

2.4 Hollow-core fibers

An HCF is an optical fiber that guides light primarily within a hollow region, resulting in a minimal portion of the optical power propagating in the solid fiber material, typically glass. HCFs can be classified into two types based on the light guiding mechanism: HC-PBFs and HC-ARFs.

2.4.1 Hollow-core bandgap fibers

An HC-PBF consists of an air core and a cladding made of quartz-air two-dimensional microstructure with periodic RI variations, typically as shown in the Fig. 2.8. In the context of conventional optical fibers, the confinement of a light beam within the core is typically based on the principle of total internal reflection. However, the mechanism of light confinement differs significantly in HC-PBFs. In these structures, the confinement of light within the hollow core is facilitated through the photonic bandgap effect [8]. The photonic bandgap effect arises from the periodic variation in the RI of the micro-structured cladding of the fiber. This variation creates a bandgap in the optical spectrum, which prevents the propagation of light within certain frequency ranges. The presence of this bandgap ensures that light is confined to the hollow core, as it cannot propagate through the cladding.

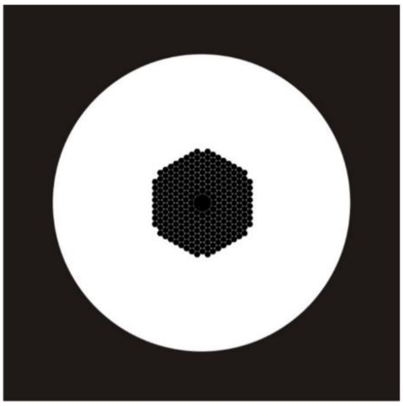

Fig. 2.8 Schematic diagram of the HC-PBF (HC-1550-02 from NKT Photonics) [9].

The characteristic of an HC-PBF is its narrow transmission window, determined by the bandgap of the cladding micro-structure. The central wavelength of the bandgap is determined by the period of the micro-structure, while the width of the bandgap is correlated to the volume fraction of air in the micro-structure. The number of core modes that a fiber can support is primarily influenced by the dimensions of the air core, with larger core sizes supporting more modes [10]. HC-PBFs with transmission central wavelengths ranging from visible to NIR wavelengths have been reported, with transmission spectral widths ranging from tens to hundreds of nano-meters. The core diameter ranges from 5 to 20 μm, with the proportion of light in the air core reaching up to 95%. The transmission loss is slightly larger than 1 dB/m at a working wavelength of 400 nm, while it is less than 0.02 dB/m near 1500 nm [11].

2.4.2 Hollow-core anti-resonant fibers

The characteristics of HC-ARFs are primarily defined by their irregular silica cladding and air core, which facilitate a unique path of light propagation. The mechanism that facilitates light guiding in HCFs can be elucidated through the utilization of the anti-resonant reflecting optical waveguide (ARROW) principle [12]. The air-core is enclosed by thin layers of silica, which effectively function as an FP resonator. The silica layers manifest an anti-resonance phenomenon, which substantially mitigates the overlap between the air-core mode and the silica cladding mode. This hindrance prevents the air-core mode from being channelled out via its interaction with the silica cladding mode continuum, a phenomenon known as inhibited coupling [13]. The HCF exhibits elevated losses under the resonance condition of the glass membrane thickness as expressed as [14]:

$$\lambda_r = \frac{2\left(t\sqrt{n^2 - 1}\right)}{m} \tag{2.15}$$

where n is the RI of the glass, t is the thickness of the glass membrane and m is the resonance order. In contrast, for wavelengths other than λ_r, the light will be restricted within the air core with minimal leakage loss. From this perspective, the broadband and multiband light guiding can be perceived as outcomes of the slab shapes of the glass membranes.

For the purpose of reducing the modal content and attenuation, various types of HC-ARFs have been studied and manufactured. Fig. 2.9 shows several types of HC-ARFs, including Kagome HCF, single-ring HC-ARF, hollow-core conjoined-tube fiber (HC-CTF) and hollow-core nested anti-resonant nodeless fiber (HC-NANF).

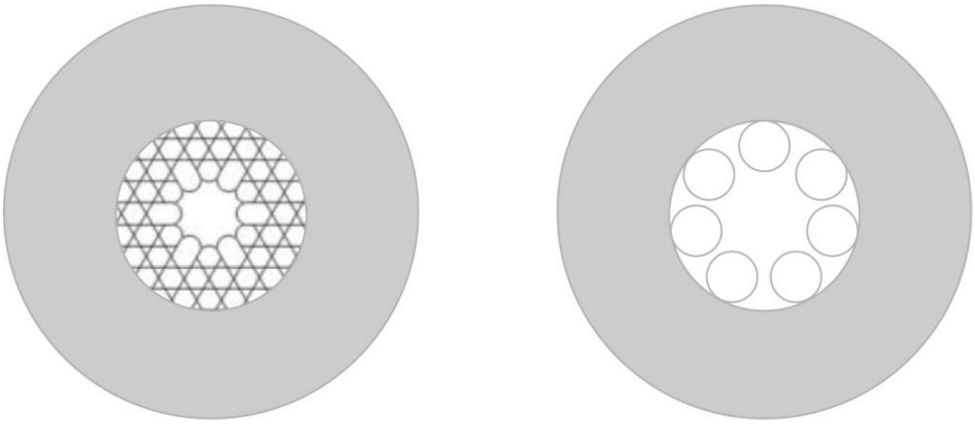

(a) (b)

(c) (d)

Fig. 2.9 Schematic diagram of HC-ARFs. (a) Kagome HCF. (b) Single-ring HC-ARF. (c) HC-CTF. (d) HC-NANF.

2.5 Conclusion

In this chapter, we expound upon the rudimentary tenets of optical gas sensing, predicated on absorption spectroscopy. Additionally, we elaborate on a few techniques, namely, WMS and PTS, which can enable the attainment of high sensitivity. Furthermore, we proffer an overview of the HCFs including HC-PBFs and HC-ARFs. We posit that the information presented herein shall serve as the underpinning for the subsequent chapters.

Reference of Chapter 2

1. H. Lefebvre-Brion, and R. W. Field, *The spectra and dynamics of diatomic molecules: revised and enlarged edition* (Elsevier, 2004).
2. R. K. Hanson, R. M. Spearrin, and C. S. Goldenstein, *Spectroscopy and optical diagnostics for gases* (Springer, 2016).
3. R. Arndt, "Analytical line shapes for Lorentzian signals broadened by modulation," Journal of Applied Physics **36**, 2522-2524 (1965).

4. J. Winefordner, "Photothermal Spectroscopy method for chemical analysis," (New York: Wiley, 1996).

5. R. C. Millikan, and D. R. White, "Systematics of vibrational relaxation," The Journal of chemical physics **39**, 3209-3213 (1963).

6. J. E. Dove, and H. Teitelbaum, "The vibrational relaxation of H2. I. Experimental measurements of the rate of relaxation by H2, He, Ne, Ar, and Kr," Chemical Physics **6**, 431-444 (1974).

7. J. Häger, W. Krieger, T. Rüegg, and H. Walther, "Vibrational relaxation of acetylene and acetylene–rare‐gas mixtures," The Journal of Chemical Physics **72**, 4286-4290 (1980).

8. J. Broeng, S. E. Barkou, T. Søndergaard, and A. Bjarklev, "Analysis of air-guiding photonic bandgap fibers," Optics letters **25**, 96-98 (2000).

9. Y. Lin, W. Jin, F. Yang, J. Ma, C. Wang, H. L. Ho, and Y. Liu, "Pulsed photothermal interferometry for spectroscopic gas detection with hollow-core optical fibre," Sci Rep **6**, 39410 (2016).

10. M. J. Digonnet, H. K. Kim, G. S. Kino, and S. Fan, "Understanding air-core photonic-bandgap fibers: analogy to conventional fibers," Journal of Lightwave Technology **23**, 4169-4177 (2005).

11. P. Roberts, F. Couny, H. Sabert, B. Mangan, D. Williams, L. Farr, M. Mason, A. Tomlinson, T. Birks, and J. Knight, "Ultimate low loss of hollow-core photonic crystal fibres," Optics express **13**, 236-244 (2005).

12. N. Litchinitser, A. Abeeluck, C. Headley, and B. Eggleton, "Antiresonant reflecting photonic crystal optical waveguides," Optics letters **27**, 1592-1594 (2002).

13. B. Debord, A. Amsanpally, M. Chafer, A. Baz, M. Maurel, J.-M. Blondy, E. Hugonnot, F. Scol, L. Vincetti, and F. Gérôme, "Ultralow transmission loss in inhibited-coupling guiding hollow fibers," Optica **4**, 209-217 (2017).

14. S. Liu, Y. Wang, M. Hou, J. Guo, Z. Li, and P. Lu, "Anti-resonant reflecting guidance in alcohol-filled hollow core photonic crystal fiber for sensing applications," Optics Express **21**, 31690-31697 (2013).

Chapter 3 Fiber optic photothermal interferometry with HCFs

In this chapter, we provide an overview of the principles underlying PTI with gas-filled HCFs. Specifically, we examine the PT phase modulation in HCFs, considering the heat generation and conduction. We then explore various types of fiber optical interferometers used to detect the PT phase modulation and discuss the phase-to-intensity conversion of optical interferometers. Finally, we investigate sources of noise in PTI.

3.1 PT phase modulation in gas-filled HCFs

3.1.1 Heat source

To understand the PT phase modulation within HCFs, a simplified model is used as shown in Fig. 3.1. The model encompasses two distinct regions: the core region filled with gases of interest where standard temperature and pressure conditions are assumed, and a fused silica solid region surrounding the air core. The thermal source is represented by the power produced per unit volume via non-radiative relaxation.

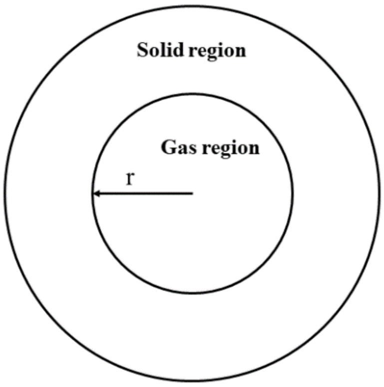

Fig. 3.1 A hollow capillary for modelling the gas-filled HCF.

The phenomenon of heat generation resulting from the PT effect can be elucidated through the alteration in molecular number density [1]. In the case of a basic two-energy system comprised of a vibrational ground state and an excited state with molecular number density N_m, the behaviour of N_m is described by a rate equation [2]:

$$\frac{dN_m}{dt} = \frac{\alpha_0 C I_p}{h\nu_p} - \frac{N_m}{\tau} \tag{3.1}$$

where h is Planck constant, ν_p is the pump wavenumber. $I_p = P_p|\psi_{pump}|^2$ is the optical intensity of pump light, where P_p is the pump power. The electric field of the pump beam is normalized over the cross-sectional area of S, denoted as ψ_{pump}, which satisfies $\langle\psi_{pump}, \psi_{pump}\rangle = \iint_S \psi_{pump}^2 dS = 1$. The relaxation time represents $\tau = 1/(\tau_n^{-1} + \tau_r^{-1})$, where τ_n and τ_r are the time constants of non-radiative and radiative relaxation, respectively. Hence, the heat source can be expressed as:

$$Q = h\nu_p \frac{N_m}{\tau} = P_p \left|\psi_{pump}\right|^2 \alpha_0 C \tag{3.2}$$

It is worth noting that since $\langle \psi_{pump}, \psi_{pump} \rangle = \iint_S \psi_{pump}^2 dS = 1$, the peak magnitude of $\left|\psi_{pump}\right|^2$ is approximately inversely proportional to the effective mode area (A_{eff}) of the HCF. Hence, compared with the free-space approaches, a HCF can deliver significantly increased peak intensity due to its small mode field area.

3.1.2 Heat conduction

The conduction of heat in a gaseous medium can be described by the equation of the heat conduction, in which the physical quantity representing the PT process is temperature T. Assuming that the pump intensity varies little along the longitudinal direction of the HCF with the simple model shown in Fig 3.1 and that the longitudinal perturbations can be ignored, then at location r in the fiber cross-section, the temperature T can be characterized by slight deviations from equilibrium values as:

$$T(r,t) = T + \delta T(r,t) \tag{3.3}$$

where T is the temperature of the equilibrium state and δT is the perturbation.

Prior to computation, it is necessary to delineate the boundary for thermal conduction. Based on the model of the hollow capillary shown in Fig. 3.1, treating the external boundary of the silica solid as an isothermal boundary serves as a satisfactory approximation [3]. This approximation substantially eases our computation, hence, necessitating the consideration of thermal conduction solely within the silica region and the gas region.

Neglecting the influences of convective heat transfer and thermal radiation, the temperature $T(r,t)$ can be governed by the heat conduction equation in the time domain, which can be explicated by [4]:

$$\rho C_V \frac{\partial \delta T}{\partial t} - \kappa \nabla^2 \delta T = Q \tag{3.4}$$

where ρ is the gas density, C_V is the specific heat at constant volume and κ is the thermal conductivity.

Assuming constant pressure, alterations in the RI can be expressed in relation to density changes, which bear resemblance to their expression in terms of temperature changes. The RI within the gas-filled HCF can then be derived by [5]:

$$n(r,t) = n + \delta n(r,t) = n + \frac{dn}{dT} \delta T(r,t) \tag{3.5}$$

where dn/dT is the thermo-optical coefficient of gaseous medium.

3.1.3 PT phase modulation

When a probe laser beam passes through a gas cell of length L, in the absence of gas absorption, the probe phase can be expressed as [4]:

$$\phi = \frac{2\pi}{\lambda} n_{eff} L \tag{3.6}$$

where λ is the probe wavelength, n_{eff} is the effective RI of the probe light.

Upon the concurrent incidence of a modulated pump laser beam into the gas cell, the gas absorption will cause the RI change of the gas medium, as expressed as Eq. (3.5). To calculate the alteration in the effective RI, it becomes necessary to execute an integration across the cross-section of the hollow core by [6]:

$$\delta n_{eff}(r,t) = \langle \delta n(r,t), \psi_{probe}^2 \rangle \tag{3.7}$$

where ψ_{probe} is the normalized electrical field of probe beam in HCF and the integration of the electrical field over the cross section of S satisfies $\langle \psi_{probe}, \psi_{probe} \rangle = \iint_S \psi_{probe}^2 dS = 1$. Combining Eq. (3.5) – (3.7), the overall probe phase changes induced by PT effect may be calculated by

$$\phi_{PT} = \frac{2\pi L}{\lambda} \cdot \frac{dn}{dT} \cdot \langle \delta T(r,t), \psi_{probe}^2 \rangle = \eta \alpha_0 C L P_{pump} \tag{3.8}$$

where η signifies a phase modulation coefficient which is contingent on the modulation frequency of the pump. This is, in turn, determined by a combination of factors: the characteristic parameters of the HCFs, the wavelengths associated with both the pump and the probe, as well as the thermodynamic properties of the gases.

Hence, we can estimate the gas concentration from the PT-induced phase modulation, which can be measured by different types of fiber optic interferometers.

3.2 Fiber optic interferometers for phase detection

A series of PT detection techniques have been established for the high sensitivity detection of RI change of gas media, including laser photothermal lens spectroscopy [7], laser photothermal deflection spectroscopy [8] and PTI. Here we focus on the basic principles of detecting PT phase modulation with optical interferometers, which includes Mach-Zehnder interferometer (MZI), Sagnac interferometer (SI), FPI and DMI.

3.2.1 Mach-Zehnder interferometer

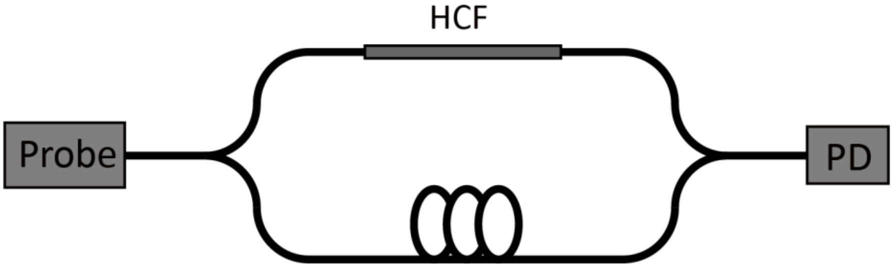

Fig. 3.2 Illustration of a fiber optic MZI.

Fig. 3.2 shows the illustration of a typical fiber optic MZI. The input light is split into two beams, one of them encompassing an HCF. The output optical power exhibits a correlation with the phase variance between the two arms:

$$P = P_1 + P_2 + 2\sqrt{P_1 P_2}\cos\phi \tag{3.9}$$

with

$$\phi = \phi_0 + \phi_{PT} \tag{3.10}$$

where $P_{1,2}$ denote the probe power output from the two arms. The phase shift ϕ between them contain two parts, a background phase shift ϕ_0 predominantly attributed to the disparity in the lengths of the two beams and the PT phase modulation ϕ_{PT}.

To achieve an optimum and linear conversion from phase to intensity, the MZI may be operated at its quadrature point where the initial phase difference (ϕ_0) of the MZI is sustained at $n\pi + \pi/2$ $(n = 0, \pm 1, \pm 2)$, as shown in Fig. 3.3.

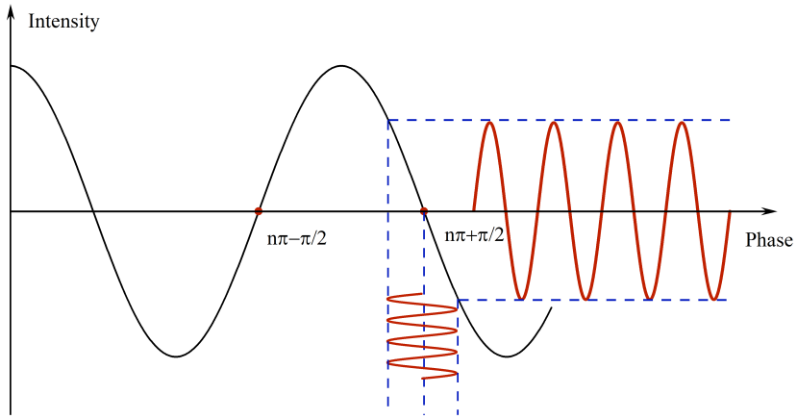

Fig. 3.3 Illustration of phase-to-intensity conversion of interferometers.

Assuming weak absorption, we have $\cos\left(\frac{\pi}{2} + \phi_{PT}\right) = -\sin\phi_{PT} \approx -\phi_{PT}$, Eq. (3.9) can be rewritten as

$$P = P_1 + P_2 - 2\sqrt{P_1 P_2}\phi_{PT} \tag{3.11}$$

The visibility of interferometric output may be expressed as [9]:

$$V = \frac{P_{max} - P_{min}}{P_{max} + P_{min}} = \frac{2\sqrt{P_1 P_2}}{P_1 + P_2} \tag{3.12}$$

Thus, the output of interferometer with the quadrature condition can be formulated in a more straightforward manner:

$$P = (P_1 + P_2)(1 - V \cdot \phi_{PT}) \tag{3.13}$$

Eq. (3.13) includes a constant term and an alternating term. Here we focus on the time-varying term containing the PT-induced phase modulation. Combing the Eq. (3.8), the alternating term of the ultimate signal extracted from the photodetector (PD) takes an expression of:

$$i = R_{PD} V \bar{P} \phi_{PT} = R_{PD} V \bar{P} \eta \alpha_0 C L P_{pump} \tag{3.14}$$

where R_{PD} is the responsivity of the PD and $\bar{P} = P_1 + P_2$ stands for the mean probe power achieving the PD. According to Eq. (3.14), the detection capability of interferometer is determined by the visibility of interferometric fringe. The degree of visibility is indicative of the interferometer's conversion efficiency from phase-to-intensity modulation, and ultimately impacts the sensitivity of phase detection. Notably, the visibility of the interferometer ranges between 0 and 1. A higher value of V is associated with a more efficient conversion, and therefore greater sensitivity in phase detection.

In practical optical interferometric systems, the static phase difference ϕ_0 is subject to environmental perturbations, including temperature, pressure and mechanical perturbations. As a result, the fluctuations in ϕ_0 may lead to deviations from the quadrature point. Therefore, the stabilization of optical interferometers is crucial. A common approach to achieve this stabilization is through the use of negative feedback servo-loop control. Within this setup, any phase deviations from the pre-determined optimal value are transformed into an error signal. This error signal is then reintegrated into the system via an optical fiber-wound piezoelectric transducer (PZT), thus compensating for fluctuations in phase.

The output interferometric signal may then be written as:

$$P = P_1 + P_2 + 2\sqrt{P_1 P_2}\cos(\phi_0 + \phi_n - \phi_c + \phi_{PT}) \tag{3.15}$$

where ϕ_c is the feedback compensation signals. ϕ_n contains the environmental perturbation, noise originating from the PZT, and the laser phase noise. Within the context of the MZI, which is responsible for detecting the single-path phase modulation through the HCF, it is crucial to balance the optical pathlengths of the two interfering beams. By accomplishing this balance, the laser phase noise can be mitigated, thereby enhancing the efficacy of phase detection within the system. Nonetheless, environmental disturbances impacting SMFs and the presence of Kerr nonlinearity within the SMFs, both integral components of the MZI, may introduce undesirable phase modulation. Consequently, these factors have the potential to compromise the stability of phase measurement.

It was discussed that to optimize and linearize the conversion from phase to intensity signal, the interferometer should be operated at the quadrature point where ϕ_0 is expected to be $n\pi + \pi/2$. Proximate to the quadrature point, the slow varying terms (V_{DC}) without the PT phase modulation (ϕ_{PT}) can be obtained as the error signal from the output signal through a low-pass filter (LPF), represented by:

$$V_{DC} = V_0(\phi_\varepsilon - \phi_c) \tag{3.16}$$

with

$$\phi_\varepsilon = \phi_0 - \frac{\pi}{2} + \phi_n \tag{3.17}$$

where V_{DC} and V_0 are the voltage signals proportional to the optical power. To stabilize the interferometer, the output V_{DC} can be extracted from the data-acquisition card (DAQ) and rerouted as feedback to an analogy control that generates a voltage signal to actuate the PZT unit. The PZT unit generates a phase ϕ_c that cancels out ϕ_ε, and hence V_{DC} can be zero.

3.2.2 Sagnac interferometer

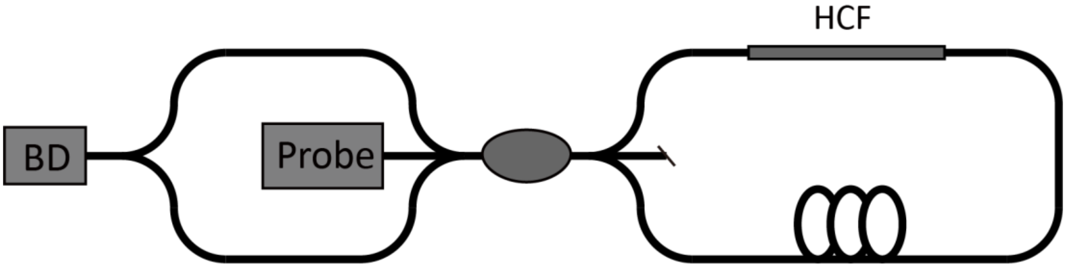

Fig. 3.4 Illustration of a fiber optic SI.

Fig. 3.4 shows the illustration of a fiber optic SI. In this configuration. A 3×3 coupler is utilized to partition the incident light into two waves propagating in opposite directions within a fiber loop. The HCF gas cell is positioned in proximity to one extremity of the looped fiber. Owing to the presence of a delay fiber, these counter-propagating waves undergo phase modulation from the HCF at distinct temporal instances. Subsequently, the two beams are recombined and detected by a balanced detector (BD). The differential optical power at the BD can be represented by [10]:

$$P = \frac{2\sqrt{3}}{9} P_0 \eta_\omega \frac{\phi_{PT}}{L} \cos\left[\omega\left(t - \frac{L_t n}{2c}\right)\right] \tag{3.18}$$

where P_0 is the probe power, L and L_t denote the length of the HCF and the total length of optical fiber, respectively, ω represents the pump modulation frequency, n signifies the RI of the SMF, η_ω is a coefficient that varies with frequency and c is the speed of light. When the condition $L \ll c/\omega n$ is met, η_ω can be approximated as $\eta_\omega \approx 2\sin\left(\omega L_t \frac{n}{2c}\right)$. Thus, the length of delay fiber can be selected to maximize η_ω while maintaining a constant modulation frequency. By employing the 3×3 coupler, the SI is capable of intrinsically operating at the quadrature point without external locking techniques.

Compared to the MZI, the single fiber configuration exhibits enhanced robustness, due to the similar susceptibility of the two beams propagating in opposite directions to environmental factors. Consequently, the phase difference between the beams remains relatively unaffected by external disturbances. A drawback of fiber optic SI, however, is the interference caused by backscattered light. As the length of the delay fiber may extend to several kilometers, increased backscattered light is to be expected. Although the impact can be mitigated through the use of a broadband probe source, the noise of fiber optic SI typically originates from the presence of backscattered light.

3.2.3 Fabry-Perot interferometer

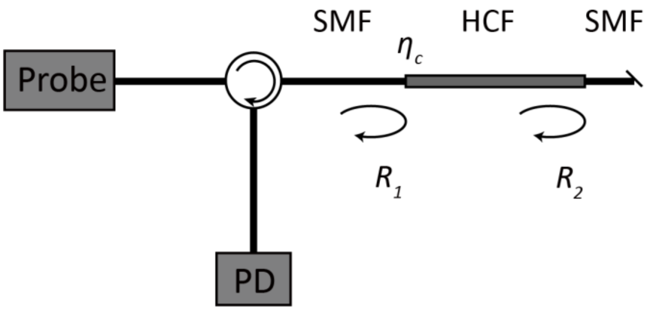

Fig. 3.5 Illustration of a fiber optic FPI.

A simpler and more compact configuration is the FPI. As shown in Fig. 3.5, it consists of a SMF, HCF, and another SMF. The optical waves reflected at the two interfaces between the HCF and SMF interfere with each other, resulting in an expression for the power detected at the PD as:

$$P = P_0\left(R_1 + R_2\eta_c^2 + 2\eta_c\sqrt{R_1R_2}\cos\phi\right) \tag{3.19}$$

where $R_{1,2}$ are the reflectivity of the two end-faces of the FPI, respectively, and η_c is the coupling efficiency between HCF and SMF. By employing servo control to adjust either the length of the HCF or the probe wavelength, the interferometer can be maintained at a quadrature point where the PT phase modulation is transformed into intensity modulation in the output, as detailed in Section 3.2.1.

The discrepancy in phase between the interfering beams of the FPI is twice the magnitude of the phase modulation experienced by a single beam as it passes through the HCF. This arrangement results in a notable resistance of the FPI against external disturbances or variations in the surrounding environment. This resilience arises due to the predominant role played by SMFs in facilitating efficient light transmission without compromising the overall stability of the interferometer. Owing to the near-simultaneous passage of reflected probe beams through the SMF, low-frequency external perturbations minimally affect the differential phase modulation. Additionally, the Kerr nonlinear coefficient of the HCF is two to three orders of magnitude smaller than that of the SMF, further reinforcing the diminished impact of the HCF on the overall phase modulation characteristics.

Nonetheless, the FPI inherently functions as an unbalanced interferometer. Consequently, the probe laser phase noise is transformed into intensity noise at the output of the FPI. This noise can surpass other sources of noise if the linewidth of the source is insufficiently narrow or if the length of the HCF is excessively long.

3.2.4 Dual-mode interferometer

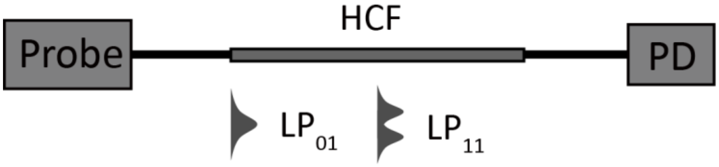

Fig. 3.6 Illustration of a fiber optic DMI.

Fig. 3.6 illustrates a fiber optic DMI. The DMI comprises two sections of SMFs and one HCF that supports two propagating modes (LP_{01} and LP_{11} modes) with low transmission loss. The pump beam is introduced into primarily the fundamental LP_{01} mode, characterized by an approximately Gaussian intensity distribution within the cross-sectional area of the fiber. The probe beam traverses both LP_{01} and LP_{11} modes. By implementing an offset alignment at the joint between the output of the HCF and the SMF to establish a DMI, the detection of differential phase modulation can be obtained by:

$$\phi_{01} - \phi_{11} = \eta' \alpha_0 C L P_{pump} \tag{3.20}$$

where $\phi_{01,11}$ are the phases of the LP_{01} and LP_{11} modes. η' denotes the differential phase modulation coefficient that depends not only on the pump modulation frequency but also on the fractional pump power in the LP_{01} mode. For the HC-ARF in Ref. [11], η' represents approximately 20% of the phase modulation coefficient of the fundamental mode. This proportionality suggests a sensitivity of differential phase modulation to variations in gas concentrations. This sensitivity emanates from the overlap between various mode fields and the non-uniform thermal profile, which in turn results in a varied response to changes in gas concentration.

Consequently, the received probe power may be represented mathematically as follows:

$$P = P_{01} + P_{11} + 2\sqrt{P_{01}P_{11}}\cos(\phi_{01} - \phi_{11}) \tag{3.21}$$

where $P_{01,11}$ are the optical power levels in the LP_{01} and LP_{11} modes.

The common-noise rejection is a notable benefit of DMI. The PTS with a DMI is sensitive to PT phase modulation within the HCF but insensitive to external environmental perturbations, enabling remarkably improved SNR.

3.3 Noise sources in fiber optic PTI

The measurement of PT phase modulation using interferometry is hindered by the presence of noise in optical interferometers. The noise level depends on the particular arrangement and setup of the interferometer, and it includes the laser noise, noise from electronic devices, and shot noise.

In an optical interferometric system, the noise may come from the probe laser noise, which exhibits fluctuations in both amplitude and phase. Noise in the amplitude is typically characterized through the fluctuations it causes in optical power normalized by the mean output power, and is termed relative intensity noise (RIN). The root-mean-square (RMS) value in the form of electric current can be derived from the RIN of the probe laser, which can be expressed as [12]:

$$i_{intensity} = R_{PD}P \cdot \sqrt{RIN \cdot \Delta f} \tag{3.22}$$

where Δf is the detection bandwidth.

In interferometric systems with arms of unequal length, the predominance of phase noise can potentially result in variations in the interferometric output, contingent on the optical path difference (OPD). At the quadrature working point, considering the transformation of phase noise into intensity noise within an interferometer, the RMS of the detection current induced by the single frequency laser phase noise may be expressed as [13]:

$$i_{phase} = R_{PD}P\frac{2}{\sqrt{\tau_c}}|\tau_d|e^{|\tau_d|/\tau_c}\sqrt{\Delta f} \tag{3.23}$$

with

$$\tau_d = \frac{\Delta L_{eff}}{c} \tag{3.24}$$

$$\tau_c = \frac{1}{\pi\Delta\nu} \tag{3.25}$$

where τ_d denotes the temporal delay between the two arms of the interferometer, which is related to the effective OPD induced by the RI difference and/or length difference, while τ_c is the coherence time of the probe laser, which is related to the laser linewidth $\Delta\nu$. The Eq. (3.23) reveals that the broader linewidth lasers exhibit higher phase into intensity noise conversion compared to narrow linewidth lasers which underscores the significance of taking laser linewidth into account while designing and implementing laser-based systems. Additionally, an increase in the effective OPD can result in a rise in both the amplitude of the PT signal and the laser phase noise in an interferometric system. It implies a trade-off stemming from the effective OPD.

In an appropriately engineered system, the noise arising from the electronic devices is relatively small and could be estimated from the power spectral density, which can be found in the manuals. We could simply estimate the noise level using:

$$i_{electronic} = \sqrt{S_p(f)\Delta f} \tag{3.26}$$

where $S_p(f)$ is the power spectral density of the electronic noise causing by the devices including PD, LIA, etc.

A fundamental constraint to the optical intensity noise is given by shot noise. Shot noise is considered to originate from the stochastic nature of photon absorption events in a PD, implying that it is not an inherent noise in the light field but rather a characteristic of the detection mechanism. The expression of shot noise can be conveniently represented in the form of electric current as [14]:

$$i_{shot} = \sqrt{2qR_{PD}P\Delta f} \tag{3.27}$$

where q is electron charge.

Thus, the total RMS of the noise current can be rewritten as:

$$i_n = \sqrt{i_{intensity}^2 + i_{phase}^2 + i_{electronic}^2 + i_{shot}^2} \tag{3.28}$$

Here we conduct a qualitative analysis of the noise present in Eq. (3.28). In an optimally engineered system, the electronic noise can typically be disregarded. When the power received by PD is minimal, shot noise prevails over both laser intensity noise and phase noise, subsequently constraining the performance of PTI detection systems. This scenario frequently occurs when there is substantial coupling loss between the HCF and the SMF. As the power of the probe light reaches a specific threshold, shot noise ceases to be the dominant source of system noise. Assuming a sufficiently narrow laser linewidth and a perfectly matched OPD in the fiber optic interferometer, phase noise can be neglected, allowing intensity noise to predominate. However, if these conditions are not met, phase noise will dominate by the conversion of phase-to-intensity noise in an interferometer. Consequently, when designing HCF-based PTI gas sensors, sensitivity can be enhanced through various approaches, including increasing the pump and probe power, utilizing a probe laser with reduced intensity noise and a narrower linewidth.

3.4 Conclusion

The basic theory of PTI in HCFs is outline. The PT phase modulation can be improved by increasing the pump power and length of the HCF. Different interferometric configurations are also reviewed. In addition, the noise sources in PTI are presented. The use of lasers with lower intensity and phase noise, as well as the detection of narrower bandwidth, can reduce the noise in interferometers. These foundational understandings serve as the underlying principles guiding the creation of a pragmatic, PTI-based gas sensor.

Reference of Chapter 3

1. D. Kliger, *Ultrasensitive laser spectroscopy* (Elsevier, 2012).

2. J.-P. Besson, "Photoacoustic spectroscopy for multi-gas sensing using near infrared lasers," (EPFL, 2006).

3. Y. Lin, W. Jin, F. Yang, J. Ma, C. Wang, H. L. Ho, and Y. Liu, "Pulsed photothermal interferometry for spectroscopic gas detection with hollow-core optical fibre," Sci Rep **6**, 39410 (2016).

4. J. Winefordner, "Photothermal Spectroscopy method for chemical analysis," (New York: Wiley, 1996).

5. C. C. Davis, and S. J. Petuchowski, "Phase Fluctuation Optical Heterodyne Spectroscopy of Gases," Applied Optics **20**, 2539-2554 (1981).

6. A. Snyder, and J. Love, "Optical Waveguide Theory (Springer Science & Business Media," (2012).

7. S. E. Bialkowski, and A. Chartier, "Diffraction effects in single-and two-laser photothermal lens spectroscopy," Applied optics **36**, 6711-6721 (1997).

8. W. B. Jackson, N. M. Amer, A. Boccara, and D. Fournier, "Photothermal deflection spectroscopy and detection," Applied optics **20**, 1333-1344 (1981).

9. M. Born, and E. Wolf, *Principles of optics: electromagnetic theory of propagation, interference and diffraction of light* (Elsevier, 2013).

10. K. Kråkenes, and K. Bløtekjaer, "Sagnac interferometer for underwater sound detection: noise properties," Optics letters **14**, 1152-1154 (1989).

11. P. Zhao, Y. Zhao, H. Bao, H. L. Ho, W. Jin, S. Fan, S. Gao, Y. Wang, and P. Wang, "Mode-phase-difference photothermal spectroscopy for gas detection with an anti-resonant hollow-core optical fiber," Nature communications **11**, 847 (2020).

12. R. Hui, and M. O'Sullivan, *Fiber-Optic Measurement Techniques* (Academic Press, 2022).

13. M. R. Salehi, and B. Cabon, "Theoretical and Experimental Analysis of Influence of Phase-to-Intensity Noise Conversion in Interferometric Systems," Journal of Lightwave Technology **22**, 1510-1518 (2004).

14. G. P. Agrawal, *Fiber-optic communication systems* (John Wiley & Sons, 2012).

Chapter 4 Optimizing the performance of PTI with a fiber optic FPI

PTI with HCF gas cells has demonstrated gas detection sensitivity in ppb levels in the NIR region. However, gases like oxygen exhibit none or weak absorption in the NIR. In this chapter, we demonstrate an oxygen sensor with a visible-pump and NIR-probe detection scheme, capitalizing on the robust oxygen absorption in the visible range and the well-established telecom fiber optic components within the NIR domain. The initial oxygen detection system with a low-finesse FPI is presented and the further improvements are made by utilizing mirrors with designed reflectivity to optimize the visibility of the FPI. A short high-finesse FP cavity is then demonstrated to achieve high performance with a more compact gas cell.

4.1 PTS based on low-finesse FPI

4.1.1 Design and test of low-finesse FPI

The construction of the gas cell employs a segment of HC-ARF, as shown in Fig. 4.1. One end of the HC-ARF is connected to a SMF at the pump wavelength (~760 nm) by fusion splicing and the opposite end is coupled via butt-joint method to a SMF at the probe wavelength (~1550 nm) via a ceramic sleeve and ferrules which are fixed together with ultraviolet curing glue.

There is a micrometer-size air gap at the HC-ARF/SMF butt-coupled joint to facilitate gas filling to the HC-ARF.

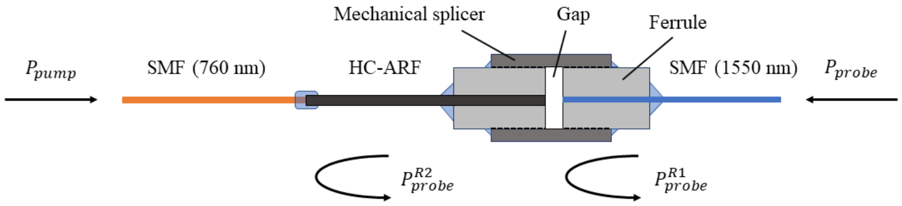

Fig. 4.1 Schematic of the SMF/HC-ARF/SMF gas cell. P^{R1}_{probe} *and* P^{R2}_{probe} *are the reflected probe beams from the SMF/HC-ARF interfaces.*

The modulated pump beam is delivered to the HC-ARF via the pump SMF to produce PT phase modulation. The amplitude of phase modulation may be expressed as Eq. (3.8). The probe beam is coupled into the HC-ARF from the opposite side via the probe SMF, and the reflections at the two HC-ARF/SMF interfaces form a low-finesse FPI to detect the PT phase modulation. The phase detected is actually the phase difference between the reflected probes waves from the two fiber joints, which is twice the phase modulation of a single pass through the HCF. Such an arrangement allows the comprehensive segregation of the pump and probe transmission optics while sharing the same HC-ARF gas cell, which enables the utilization of the best quality fibers in terms of transmission loss and mode quality and other components optimized for the pump and probe wavelengths, respectively.

The absorption spectrum of oxygen around 760 nm is shown in Fig. 4.2(a). We use the absorption line around 760.88 nm, which has an absorption coefficient of 1.425×10^{-3} cm^{-1} at 293 K and 1 atm for a relative concentration of 100% [1]. The transmission spectrum of the HC-ARF used in this work is depicted in Fig. 4.2(b). As shown in Fig. 4.2(c), the HC-ARF has an inscribed air-core with diameter of ~35 μm which is surrounded by seven capillary rings with diameter of 17.5 μm. The HC-ARF has double transmission windows covering wavelength from below 600 to ~800 nm and from ~1 to beyond 1.7 μm.

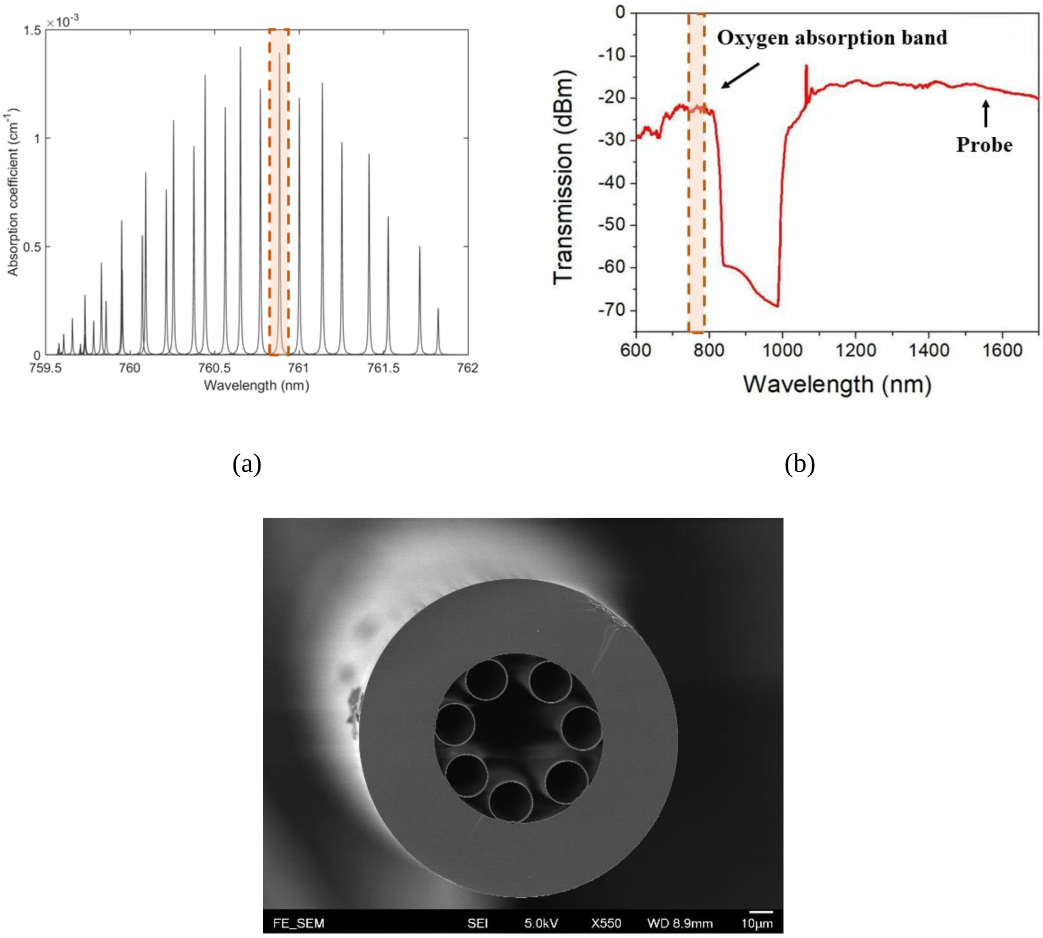

(a) (b)

(c)

Fig. 4.2 (a) Absorption lines of oxygen from 759.5 to 762 nm at 293 K and 1 atm determined by the HITRAN database. (b) Spectral transmission of the HC-ARF. (c) The cross-sectional image of the HC-ARF.

To evaluate the performance of the FPI with the HC-ARF, the reflected spectrum of the FPI is measured with the wavelength resolution of 20 pm as shown in Fig. 4.3(a). Based on the measured reflected spectrum, the free spectral range (FSR) of the FPI is nearly 28 pm. Giving the relationship between the cavity length L and the measured FSR:

$$L = \lambda_{probe}^{2} / (2 \cdot FSR) \tag{4.1}$$

With the probe light wavelength λ_{probe}=1550 nm and FSR=28 pm, the length L is estimated to be 4.2 cm, which is consistent with the direct measurement. The fast Fourier transform (FFT) of the FPI transmitted spectrum is shown in Fig. 4.3(b). The peak at spatial frequency of 37.5 nm^{-1} is identified as the FP interference.

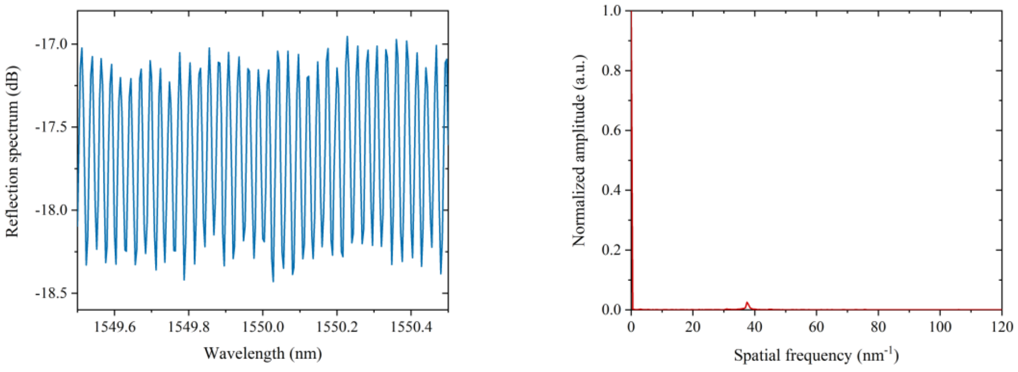

(a) (b)

Fig. 4.3 (a) The measured reflected spectrum of a 4.3-cm-long FPI. (b) The FFT of the FPI transmitted spectrum.

4.1.2 Experimental setup

Fig. 4.4 depicts the setup of the PTI-based oxygen detection system using the HC-ARF. We employ a distributed feedback (DFB) laser with wavelength around 760 nm and linewidth of ~10 MHz as the pump and a semiconductor optical amplifier (SOA) to amplify pump power to about 30 mW. The pump laser is wavelength-modulated sinusoidally while being slowly scanned across the oxygen absorption line at 760.88 nm. The external-cavity diode laser (ECDL) of 1550 nm is utilized as the probe light. The cavity length is 4.3 cm. The HC-ARF is mounted on a PZT so that the cavity length can be servo-controlled, by monitoring the DC component of output from PD1, to ensure that the FPI works at quadrature at the probe wavelength.

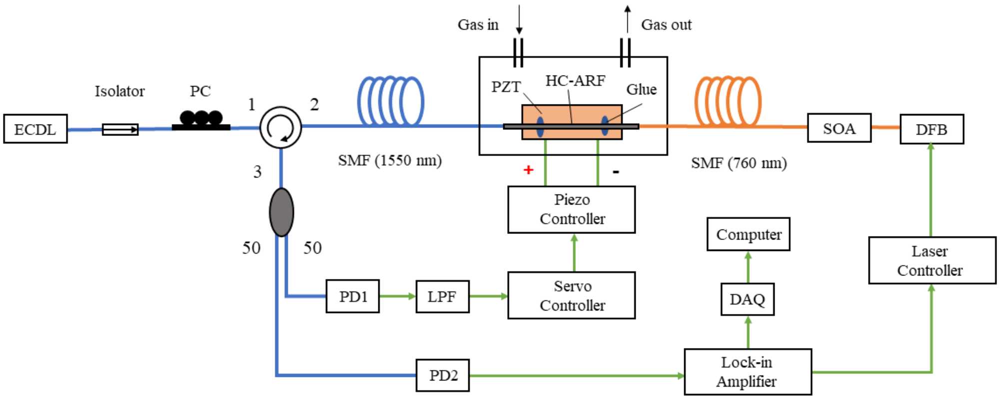

Fig. 4.4 Experimental setup of oxygen detection based on PTI with a HC-ARF. PC: polarization controller.

The pump modulation is achieved by modulating the injection current of the DFB laser which modulates the laser frequency and intensity simultaneously. Since the residual intensity modulation (RIM) of the pump power has large contribution to the non-absorption background of $1f$ signal, the demodulation of $2f$ signal is preferred in traditional WMS. However, for the PTI system studied here, only the pump power absorbed by gas molecules will contribute to the PT phase modulation, hence the influence of RIM on its non-absorption background is negligible. Thus, we demodulate the $1f$ component from PD2 by using a LIA, which has the largest amplitude among all the harmonic components of wavelength modulation without strong background signal [2].

4.1.3 Frequency response

The magnitude of PT phase modulation in the HC-ARF has a dependence on the structure of the HC-ARF, pump modulation frequency, gas thermal relaxation rate and thermal conduction parameters [3]. The relaxation in PT process involves the multi-step transitions at different relaxation rate. If the thermal relaxation rate is slower compared with heat conduction, the heat production may not be observed via PT signal [4]. For oxygen molecules, we focus here on one characteristic time of the order of microseconds corresponding to the transition from $b^1\sum_g^+$ to

$a^1\Delta_g$, since the relaxation times of other processes are relatively long and above the order of milliseconds. In this case, only a part of the absorbed energy eventually contributes to the PT signal [5]. The efficiency of heating may be expressed in the form of [6]:

$$H(\omega\tau) = \frac{1}{\sqrt{1 + (\omega\tau)^2}} \tag{4.2}$$

where ω is the pump angular modulation frequency and τ is the relaxation time. If the relaxation time is shorter compared to the pump modulation period, the absorbed energy will be effectively transferred to heat. However, when the value of $\omega\tau$ is larger than or comparable to the unity, the efficiency of heating will be significantly reduced.

On the basis of considering the relaxation time and heating efficiency of oxygen, we further investigate the PT phase modulation in the HC-ARF. By using COMSOL Multiphysics software, we conducted numerical calculations to determine the PT phase modulation in the oxygen-filled HC-ARF at various frequencies of the pump modulation [7]. The model illustrating the HC-ARF is presented in Fig. 4.5, exhibiting a silica outer cladding characterized by an inner diameter measuring 70 μm. Additionally, an inner cladding composed of seven rings with a diameter of 17 μm is incorporated within the structure. The mode fields for the pump and the probe in the HC-ARF may be approximated as Gaussian distribution with mode field radiuses of 12.5 μm at 760 nm and 13.5 μm at 1550 nm. The cladding material of the HC-ARF is silica and its hollow region is filled with 20.8% oxygen balanced in nitrogen. The ambient temperature and gas pressure are assumed to be 293 K and 1 bar, respectively. The thermal parameters of nitrogen are used in solving the thermal conduction equation. The pump is sinusoidally modulated at frequency *f*, which is varied from 2 and 100 kHz.

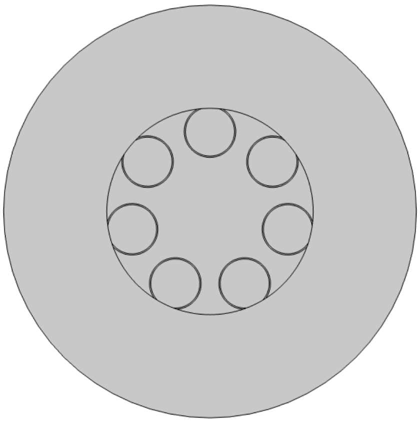

Fig. 4.5 The model for the HC-ARF.

By utilizing the aforementioned information, one can derive the amplitude of PT phase modulation through an examination of its dependency on modulation frequency. For the convenience of comparison, we selected the amplitude of PT phase modulation at 3 kHz as the reference value and the normalized output is expressed as a level in decibels (dB) by evaluating ten times the common logarithm of the ratio of the simulation results to the reference value, which is represented by the red line in Fig. 4.6. The blue dots are the data obtained from the experiment. At low pump modulation frequencies, the PT phase modulation shows a relatively flat response. At high pump modulation frequencies (e.g., *f* >15 kHz), due to the slow thermal conduction related to the buffer gas thermal parameters and fiber characteristics, the change of temperature field could not catch up the laser modulation rate, leading to a reduced amplitude of PT phase modulation.

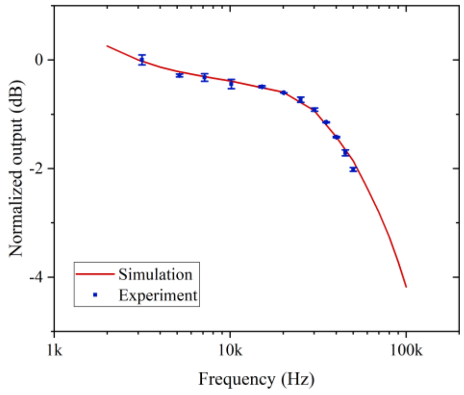

Fig. 4.6 Normalized PT signal as a function of pump modulation frequency. The red line is calculated by COMSOL Multiphysics and the blue dots are the experimental data. Error bars depict the standard deviation (s.d.) of measured data.

4.1.4 Experimental results

The $1f$ signal as a function of modulation frequency from 3 to 50 kHz was measured in atmosphere with ~20.8% oxygen. For comparison with numerical simulation, the $1f$ signal is normalized to the value at 3 kHz and expressed in dB, which is represented as the blue dots in Fig. 4.6. Since the PT signal decreases relatively quickly with increasing pump modulation frequency above 15 kHz, we fix the pump modulation frequency to 15 kHz for subsequent oxygen concentration detection experiments. The first harmonic output is depicted in Fig. 4.7.

The peak-to-peak (p.p.) amplitude of the 1*f* signal is 153.5 µV when the pump laser is swept across the absorption line of oxygen. To determine the system noise level, the pump wavelength is deliberately adjusted away from the absorption line and kept fixed at 760.9 nm, resulting in an estimated noise level of 0.25 µV. With a lock-in time constant of 1 s with and a filter slope of 18 dB/Oct, the SNR is calculated to be ~614, corresponding to the NEC of 339 ppm.

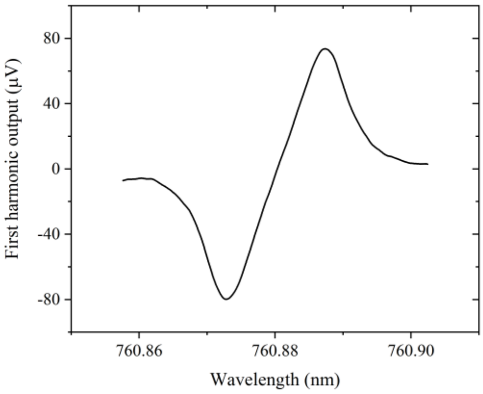

Fig. 4.7 First harmonic output signal for ~20.8% oxygen in air.

Fig. 4.8(a) shows the recorded 1*f* signal for 5%, 10%, 20.5%, 41.2% and 61.1% oxygen in nitrogen. Fig. 4.8(b) presents the dependence of the amplitude of the 1*f* signal on the oxygen concentration, ranging from 5% to 60%, while maintaining a nitrogen balance. The PT signal increases approximately linearly with oxygen concentration.

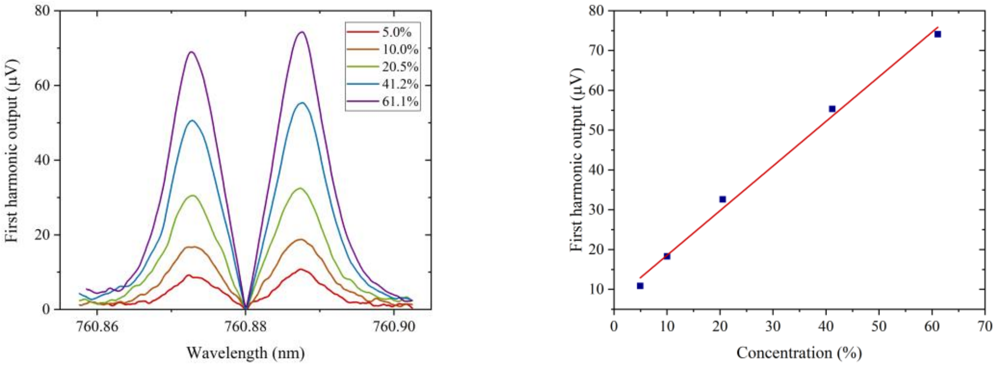

(a) (b)

Fig. 4.8 (a) Measured 1f signal for 5%, 10%, 20.5%, 41.2% and 61.1% oxygen in nitrogen. (b) The p.p. of the PT signal with the oxygen concentration ranging from 5% to 60%.

To assess the stability of the detection system, we conducted an Allan-Werle deviation analysis. The 1*f* signal for oxygen in atmosphere was recorded for over 3 hours, while the pump wavelength remained fixed at 760.9 nm, away from the absorption line, and with a time constant of 100 ms for the LIA. The resulting Allan-Werle plot is presented in Fig. 4.9. The optimal averaging time is approximately 600 s, yielding a noise level of approximately 0.04 µV. Using a SNR of unity, the corresponding NEC is 54 ppm. For a shorter averaging time of 100 s, the NEC increases to 135 ppm.

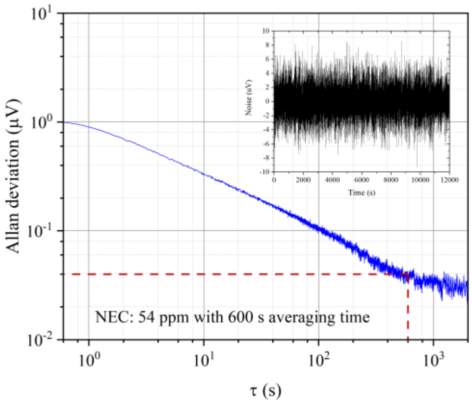

Fig. 4.9 Allan-Werle plot using the noise data obtained from a recording period of 3 hours.

4.2 Performance enhancement by optimizing the mirror reflectivity

The enhancement of detection sensitivity in the FPI could be approached from two aspects. One involves augmenting the interaction length between the pump light and the gas contained within the HCF. The other is to optimize the visibility of the FPI thereby increasing the efficiency of the PT phase-to-intensity conversion. To achieve these two purposes, the simplest way is to design the reflectivity for the pump and probe at the two ends of the FPI separately.

4.2.1 Construction of the FPI with designed reflective mirrors

The basic design of the FPI with reflective mirrors is shown in Fig. 4.10(a). The FPI is formed by sandwiching a 14.5-cm-long HC-CTF between the SMFs. The employed HC-CTF features an air core that is inscribed with a diameter measuring 30 μm. It has multiple transmission windows covering wavelength bands of 750-850 nm, 950-1200 nm, and 1400-1650 nm, as shown in Fig. 4.10(b). The HC-CTF has smaller transmission loss and bending loss compared with the HC-ARF used in the previous section, and hence we choose this HC-CTF for oxygen detection from this section. The SMFs and the HC-CTF are joined together by mechanical splicing with small air gaps of a few microns to enable gas filling into the hollow core.

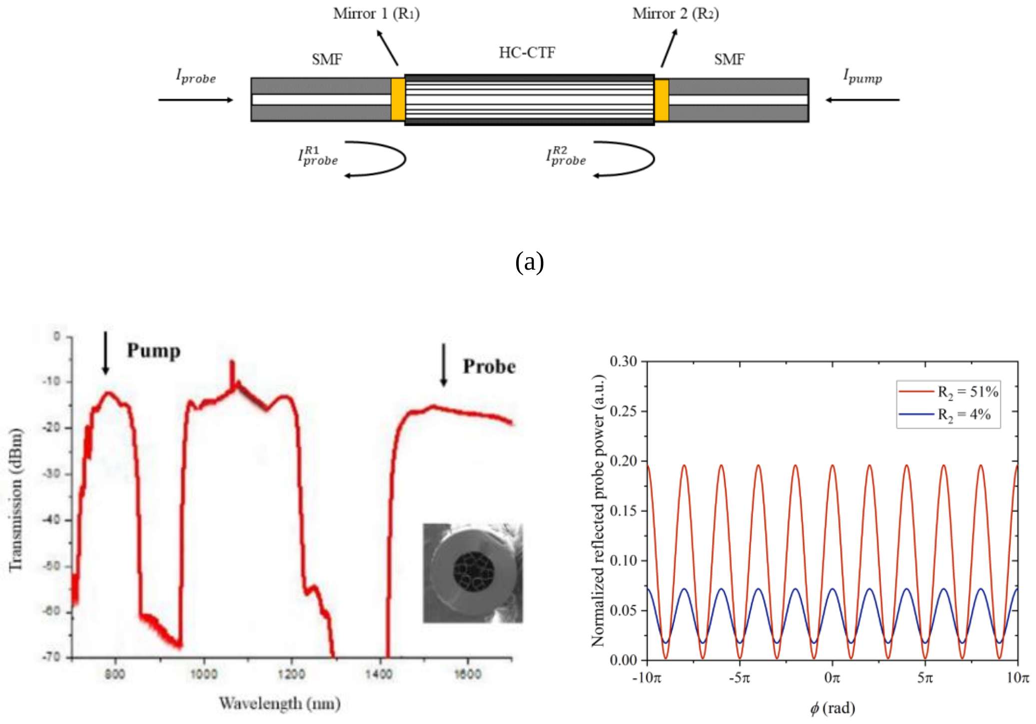

(a)

(b)

(c)

Fig. 4.10 (a) Illustration of the SMF/HC-CTF/SMF gas cell with designed reflective mirrors. (b) Spectral transmission of the HC-CTF. The inset is the cross-sectional image of the HC-CTF. (c) Simulated reflection spectrum of the FPI with different reflectivity of R_2 *and fixed* R_1 *of 4%.*

Compared with the FPI described in the previous chapter, the end-face of the SMF is coated with the mirrors with different reflectivity. Given the direct proportionality between the PT phase modulation and the length of interaction between the pump light and the gas inside the HCF, an extension of the HCF length from 4.3 cm to 14.5 cm is implemented. However, the gas cell with the longer length of the HCF is more susceptible to environmental perturbation, which enhances the detection sensitivity at the expense of the system stability. To further increase the optical path length of the pump light, the reflectivity of the mirror 1 as shown in Fig. 4.10(a) is >99.9% at the oxygen absorption band around 760 nm, which allows the pump light to travel one round trip within the HCF. Hence, the interaction length between the pump light and the gaseous medium is theoretically increased by a factor of ~6.7 compared with the 4.3-cm-long gas cell operated in Section 4.1. The reflectivity of the mirror 2 around 760 nm is controlled to within 1% to minimize multi-beam interference of the pump light.

The sensitivity of PT phase detection is influenced by the performance of the interferometer. The received power of the reflected light to the PD can be expressed as Eq. (3.19), with the experimentally measured coupling efficiency η_c of about 28%. Considering that the reflectivity of the mirror 1 for the probe is 4%, ideally, the visibility of the FPI for the probe light is optimal, i.e., $V = 1$, when the reflectivity of the mirror 2 is 51%. The red line depicted in Fig 4.10(c) represents the reflection spectrum of the FPI ascertained through simulation. For comparative purposes, the blue line illustrates the reflection spectrum of the FPI with a 4% reflectance of mirror 2, corresponding to the reflection spectrum of the FPI in Fig. 4.1. Compared with the FPI devoid of any coating treatment, the visibility of the FPI is increased to nearly 1. Consequently, the reflectivity of mirror 2 is designed to be 50%-60% to further enhance the PT phase-to-intensity conversion efficiency.

4.2.2 Oxygen detection with the optimized FPI

The experimental setup with the optimized FPI is illustrated in Fig. 4.11. We use a narrow-linewidth (<5 kHz) optical fiber laser (OFL) with a PZT (for wavelength tuning) as the probe source at 1550 nm and adjust the PC to maximize the visibility of FPI. The probe wavelength is operated at the quadrature point by monitoring the DC component of the probe detected by the PD1. The experimental parameters of the pump module are identical to that in Fig. 4.4. The mirrored SMF is commercial SMF-28e, which is multimode around 760 nm. We find that a PC may not provide an optimal solution for mode control, yet it offers a degree of simplicity. By meticulously adjusting the alignment of the PC, it is feasible to increase the coupling of pump power into the fundamental mode.

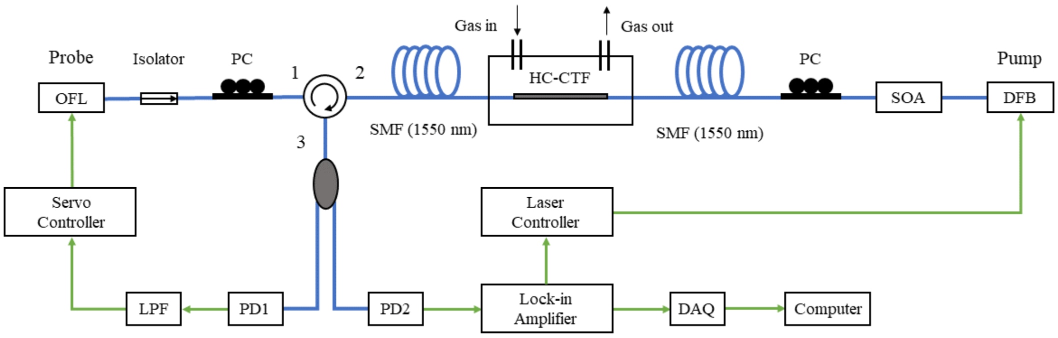

Fig. 4.11 Experimental setup of oxygen detection based on PTI with an HC-CTF.

Experiment was conducted under laboratory conditions with ambient air containing ~20.8% oxygen. The normalized frequency responses of PT phase modulation are demonstrated theoretically and experimentally with red line and blue dots as shown in Fig. 4.12(a), respectively. The simulation results are computed in the same way as detailed in Section 4.1.3. The modelled HC-CTF, as shown in Fig. 4.12(b), has a mode field radius of 12.2 μm at 760 nm and 12.1 μm at 1550 nm. Other simulation parameters are identical as before. The magnitude of PT phase modulation remains unchanged at low modulation frequencies and drops at higher modulation frequencies (e.g., *f* > 13 kHz).

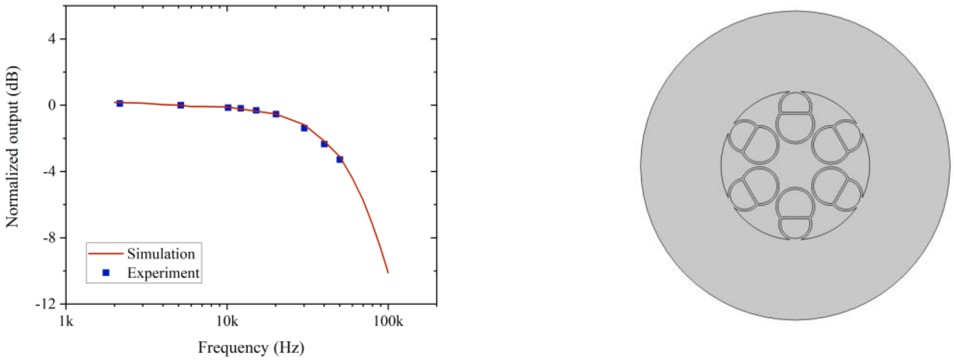

(a) (b)

Fig. 4.12 (a) Normalized PT signal as a function of pump modulation frequency. The red line is calculated by COMSOL Multiphysics and the blue dots are the experimental data. (b) The model for the HC-CTF.

For a pump power of approximately 30 mW, the magnitude of 2*f* (*f* =13 kHz) signal reaches 6.2 mV when the pump is swept across the absorption line at 760.9 nm, as shown in Fig. 4.13(a). To determine the system noise level, the pump wavelength is adjusted away from the absorption line and fixed at around 761.2 nm. For a lock-in time constant of 1 s, the SNR is 11697, giving an oxygen detection limit of 24 ppm for an SNR of unity.

Allan-Werle deviation analysis was also conducted based on the noise data recorded over 11 hours with a lock-in time constant of 100 ms when the pump wavelength was fixed at 761.2 nm, as shown in Fig. 4.13(b). The optimal averaging time is ~1000 s, at which the noise is ~0.070 µV. The corresponding NEC for the SNR of unity is estimated to be 3 ppm. The NEC for 10 s and 100 s averaging time are 21 ppm and 7 ppm, respectively.

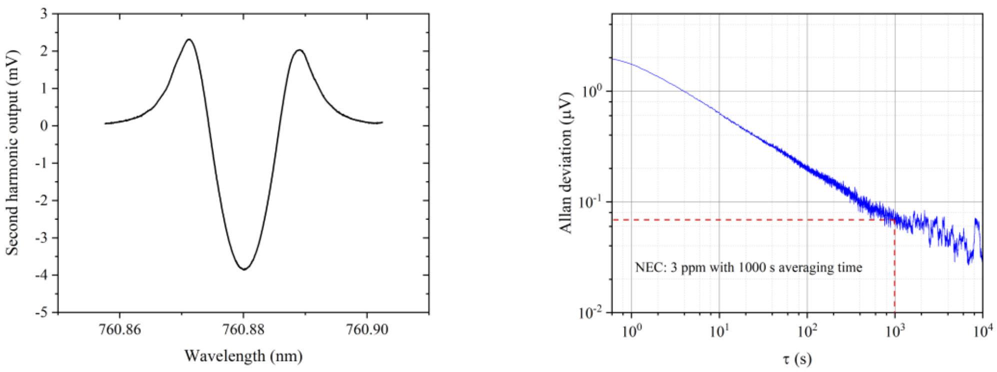

(a) (b)

Fig. 4.13 (a) The detected 2f signal of ambient air (~20.8% oxygen). (b) Allan-Werle plot based on the noise data over a period of 11 hours.

In order to assess the long-term stability of oxygen detection, ambient air with an oxygen concentration of approximately 20.8% was employed at standard room temperature and atmospheric pressure. The evaluation was conducted over a duration of 7 hours. The peak value of 2*f* signal was recorded by maintaining the pump wavelength fixed at the absorption line of oxygen, utilizing a time constant of 1 s, as shown in Fig. 4.14. The observed fluctuations in the recorded signal were found to be within 4.2%, indicating a favourable level of long-term stability. The fluctuations in the recorded signal can be attributed to various factors. Firstly, power fluctuations of both the pump and probe sources contribute to the observed signal fluctuations. Secondly, the drift of the working point of the probe interferometer can also affect the stability of the signal. Lastly, fluctuations in environmental parameters such as temperature, pressure, and humidity can introduce additional sources of signal drift.

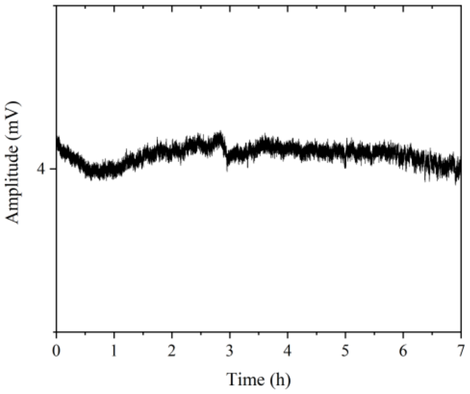

Fig. 4.14 Variation of the peak value of the 2f signal over 7 hours.

4.3 Cavity-enhanced PTS with a high-finesse Fabry-Perot cavity

In this section, we further present a compact, high-finesse FP cavity designed for oxygen detection. A shorter HCF is utilized to mitigate environmentally induced signal fluctuations. And the high-finesse cavity is to enhance the detected signal, derived from the PT phase modulation, by a factor directly proportional to the cavity finesse, thereby improving the overall performance of the system.

4.3.1 Construction of the high-finesse FP cavity

The schematic of the high-finesse FP cavity is shown in Fig. 4.15(a). The FP cavity is formed by sandwiching a 1-cm-long HC-CTF between the mirrored ends of two standard SMFs. The SMFs and the HC-CTF are joined together by mechanical splicing. The modulated pump beam is delivered to the HC-CTF to produce PT phase modulation.

The reflectivity of the mirrored SMF is <1% in the oxygen absorption band around 760 nm, which forms a non-resonant single pass configuration for the pump beam. The probe beam is coupled into the HC-CTF from the opposite end and the mirror reflection of >99% over the wavelength range of 1530 to 1570 nm enables the formation of a high-finesse FP cavity for the probe to detect the PT phase modulation.

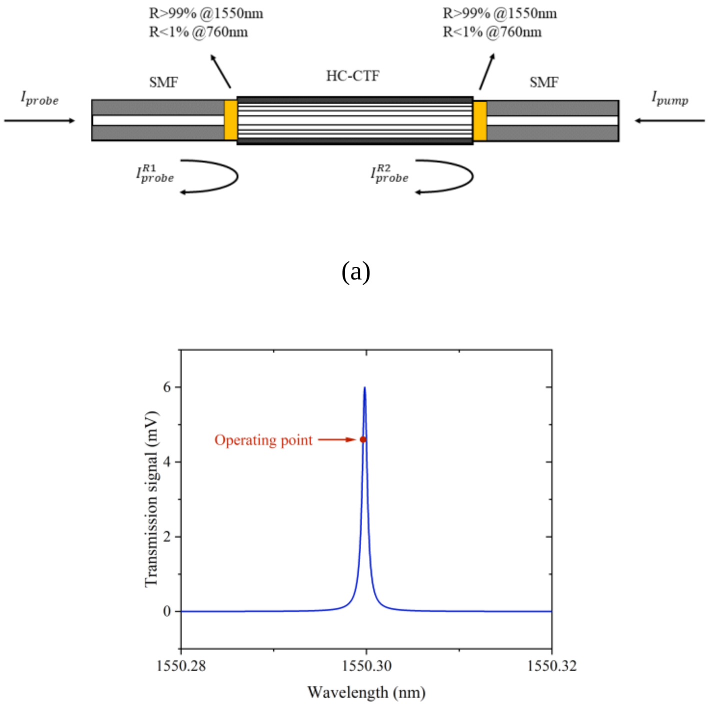

(a)

(b)

Fig. 4.15 (a) Schematic of the high-finesse FP cavity. (b) Measured transmission spectrum of the FP cavity.

Fig. 4.15(b) illustrates the transmission of the FP cavity around 1550.3 nm, which is selected as the probe wavelength. The FSR is measured to be 14.4 GHz and the linewidth of the cavity resonance is ~100 MHz, giving a cavity finesse of ~144. The operating wavelength of the probe is carefully selected to align with the steepest slope point of the transmission spectrum, which maximizes the sensitivity for phase detection, as shown in Fig. 4.15(b). The slope at the operating point is proportional to the cavity finesse and hence the PT signal of the high-finesse cavity is amplified by the resonating FP cavity as compared with the low-finesse FPI.

4.3.2 Oxygen detection with the high-finesse FP cavity

The experimental setup with the high-finesse FP cavity is shown in Fig. 4.16. We use a DFB laser with wavelength around 761.1 nm and linewidth of ~2 MHz as the pump and a narrow-linewidth OFL at 1550.3 nm as the probe source. The pump laser is wavelength-modulated at ~13 kHz while being slowly concurrently scanned across the oxygen absorption centered at 761.1 nm. The pump beam is delivered into the HC-CTF via a wavelength division multiplexer (WDM), propagates through the HC-CTF, and is eventually blocked by the isolator. The probe is launched into the HC-CTF from the opposite end and the transmitted probe through the FP cavity passes through the same WDM. An optical band-pass filter (OBPF) is employed to block the pump so that only the probe beam passes through. The transmitted probe beam, after passing the FP cavity, is detected by two PD1 and PD2. The probe wavelength is locked to the steepest slope position of the transmission by monitoring the DC component of the probe transmitted through the FP cavity with the PD1. The second harmonic component from the PD2 is demodulated by a LIA and used as the output signal.

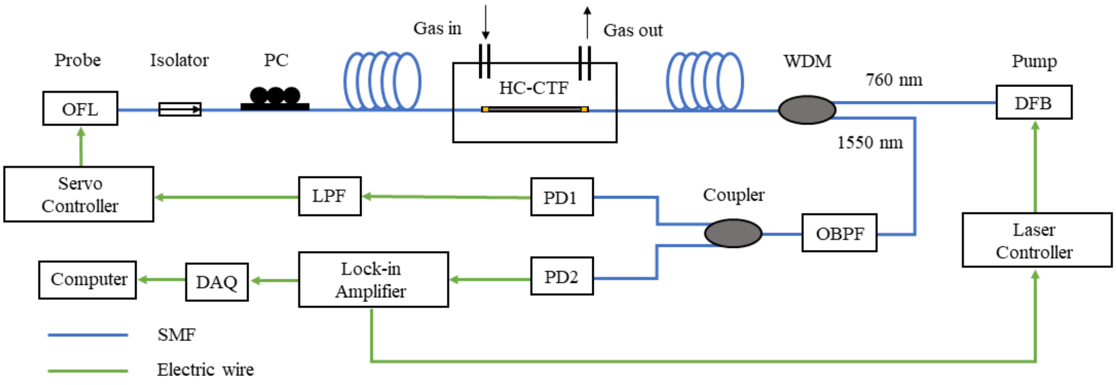

Fig. 4.16 Experimental setup for oxygen detection with a high-finesse FP cavity.

Experiment was conducted under laboratory conditions with ambient air containing ~20.8% oxygen and the pump power delivered to the HC-CTF is about 3 mW without the use of a SOA. Fig. 4.17(a) illustrates the recorded 2*f* signal when the pump is swept across the absorption line at 761.1 nm. The system noise is determined by tuning the pump wavelength away from the absorption line and fixing it around 761.2 nm and the results are presented in Fig. 4.17(b). For a lock-in time constant of 1 s, the output PT signal amplitude is 6.11 mV and the s.d. of the noise is 1.67 µV. The SNR is 3659, giving an oxygen detection limit of 57 ppm for an SNR of unity.

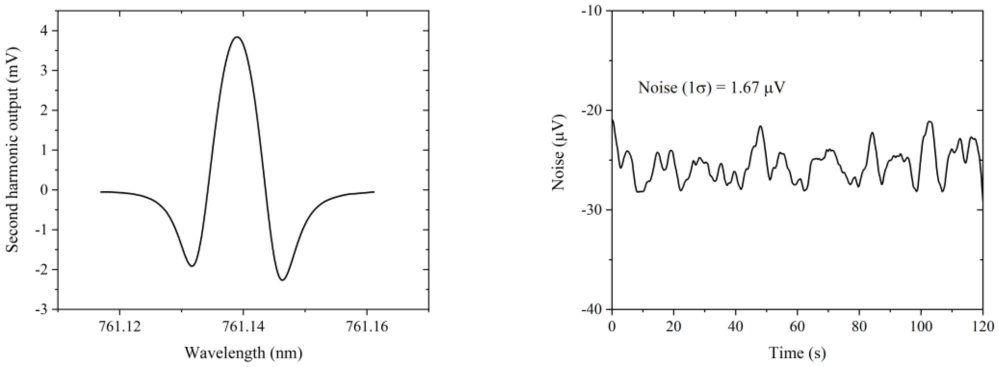

(a) (b)

Fig. 4.17 (a) Measured 2f signal of ambient air (~20.8% oxygen). (b) 2f signal when the pump is tuned away from the absorption line of oxygen.

Allan-Werle deviation analysis was performed utilizing the noise data collected over 14 hours, employing a lock-in time constant of 100 ms, and fixing the pump wavelength at 761.2 nm. The results are displayed in Fig. 4.18. The optimal averaging time is ~1000 s, yielding a noise level of ~0.17 μV. Correspondingly, the NEC for an SNR of unity is estimated to be 6 ppm. For shorter averaging times of 10 s and 100 s, the NEC values are ~53 ppm and ~17 ppm, respectively.

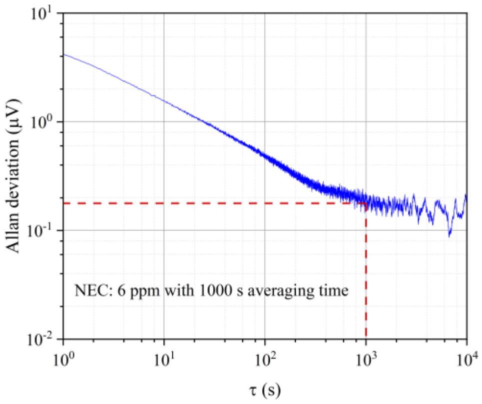

Fig. 4.18 Allan-Werle plot utilizing the noise data over a period of 14 hours.

To determine the dynamic range of the oxygen detection, the HCF sample was tested with varying concentrations of oxygen. Initially, the HCF sample was filled with pure nitrogen followed by a combination of pure oxygen and nitrogen at different ratios. The results of this experiment are displayed in Figure 4.19(a), revealing a favourable linear relationship between the detected signal and oxygen concentrations up to 90%. These results demonstrate that our detection system is capable of detecting oxygen within a concentration range spanning from low levels up to 90%. With a lower detection limit of 57 ppm in terms of NEC, the estimated dynamic range of our system exceeds four orders of magnitude, spanning from 57 ppm to 90%.

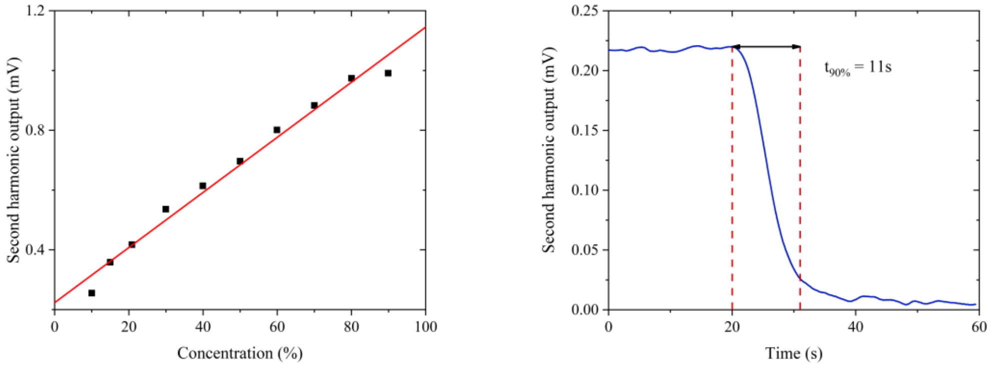

(a) (b)

Fig. 4.19 (a) The p.p. value of the 2f signal as a function of gas concentration. (b) The peak amplitude of the 2f signal as a function of time during gas unloading.

To examine the response time of the oxygen detection system, the gas chamber was initially filled with 20% oxygen balanced with nitrogen. The peak amplitude of the $2f$ signal was then collected while keeping the pump wavelength at 760.88 nm. Upon achieving a stable peak signal, the gas chamber was purged using pure nitrogen. Fig. 4.19(b) displays the peak value of the $2f$ signal over time. The response time, defined as the time required for the signal to decrease to $1-e^{-1}$ of the steady-state signal after purging with pure nitrogen, was determined to be 11 s. It is worth noting that the response time of the current gas sensor is not limited by the HCF gas cell but rather by the time required to fill the gas chamber. Further reduction of the response time could be theoretically achieved through introducing the microchannels along the HCF [8].

To assess the long-term stability of the system, the pump wavelength was repeatedly scanned across the oxygen absorption line and the p.p. value of $2f$ signal was recorded over a period of 3 hours. The variation of the p.p. value, normalized to the average, over 3 hours is 1.6%, as shown in Fig. 4.20. Compared to other FPI configuration, this system is stable due to the fact that the length of the HCF is only 1 cm, making it less susceptible to environmental interference.

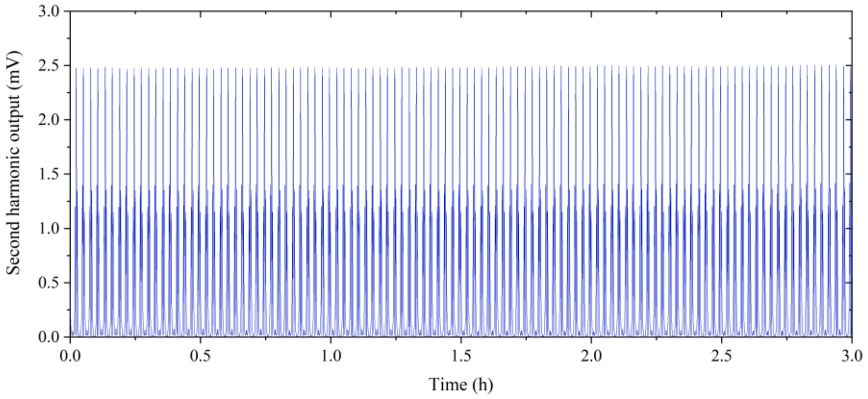
Second harmonic output (mV)
3.0
2.5
2.0
1.5
1.0
0.5
0.0
0.0
0.5
1.0
1.5
2.0
2.5
3.0
Time (h)

(a)

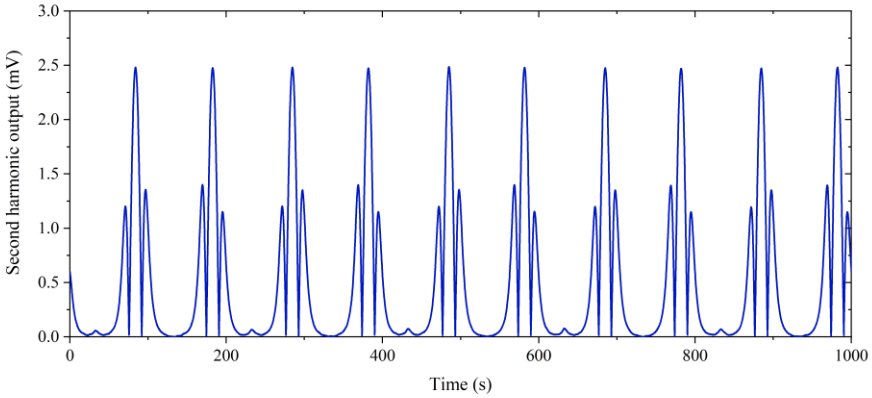
Second harmonic output (mV)
3.0
2.5
2.0
1.5
1.0
0.5
0.0
0
200
400
600
800
1000
Time (s)

(b)

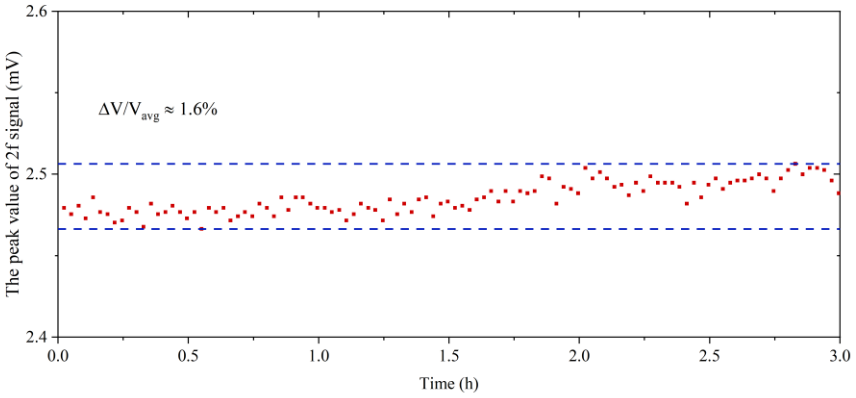
The peak value of 2f signal (mV)
2.6
2.5
2.4
ΔV/V_avg ≈ 1.6%
0.0
0.5
1.0
1.5
2.0
2.5
3.0
Time (h)

(c)

Fig. 4.20 (a) 2f signal over a period of 3 hours. (b) 2f signal from 0 to 1000 s. (c) The variation of the peak value of the 2f signal over 3 hours.

The signal fluctuations observed in Fig. 4.20 may be attributed to two sources. Firstly, due to the use of the laser source with a long coherence length, parasitic interferences caused by reflections and backward scattering may constrain the measurement stability. Secondly, the pump power within the HCF experiences fluctuations. Despite the application of anti-reflection coatings, a low-finesse FPI persists for the pump light, which in turn causes alterations in the pump power distribution within the HCF. The forthcoming chapter will explore these limitations in greater detail and propose potential solutions to address these challenges.

4.4 Conclusion

In this chapter, we present the all-fiber PTS-based gas sensors with optimized FPI configurations for sensitive oxygen detection.

We propose a scheme incorporating visible-pump and NIR-probe, capitalizing on the strong oxygen absorption in the visible range and the well-established telecom fiber optic components within the NIR domain. The detection limit of oxygen down to 54 ppm with a 600-s averaging time is achieved. By considering the thermal relaxation of oxygen and heat conduction in the

HCF, the PT phase modulation as a function of pump modulation frequency is investigated theoretically and experimentally.

To further improve the detection limit, several methods are presented. Firstly, employing a longer HCF serves as a simple way to increase the magnitude of the PT phase modulation. Secondly, the optical path length of the pump light is doubled. Lastly, optimizing the visibility of the FPI could lead to an improvement in the phase-to-intensity conversion. With the optimized FPI, we achieve an oxygen detection limit of 3 ppm with 1000-s averaging using a 14.5-cm-long HCF with about 30 mW pump power.

To achieve high performance with a more compact gas cell, we propose a high-finesse FP cavity with a 1-cm-long HCF. This configuration enables the detection of oxygen down to 6 ppm, with an averaging time of 1000 s and an approximate pump power of 3 mW. Furthermore, we also demonstrate a long-term stability of <1.6% over 3 hours. By using a shorter HCF gas cell and avoiding the use of a SOA to amplify the pump power, the stability of the system is improved significantly.

Reference of Chapter 4

1. I. E. Gordon, L. S. Rothman, C. Hill, R. V. Kochanov, Y. Tan, P. F. Bernath, M. Birk, V. Boudon, A. Campargue, K. V. Chance, B. J. Drouin, J. M. Flaud, R. R. Gamache, J. T. Hodges, D. Jacquemart, V. I. Perevalov, A. Perrin, K. P. Shine, M. A. H. Smith, J. Tennyson, G. C. Toon, H. Tran, V. G. Tyuterev, A. Barbe, A. G. Csaszar, V. M. Devi, T. Furtenbacher, J. J. Harrison, J. M. Hartmann, A. Jolly, T. J. Johnson, T. Karman, I. Kleiner, A. A. Kyuberis, J.

Loos, O. M. Lyulin, S. T. Massie, S. N. Mikhailenko, N. Moazzen-Ahmadi, H. S. P. Muller, O. V. Naumenko, A. V. Nikitin, O. L. Polyansky, M. Rey, M. Rotger, S. W. Sharpe, K. Sung, E. Starikova, S. A. Tashkun, J. Vander Auwera, G. Wagner, J. Wilzewski, P. Wcislo, S. Yu, and E. J. Zak, "The HITRAN2016 molecular spectroscopic database," J Quant Spectrosc Ra **203**, 3-69 (2017).

2. C. Yao, S. Gao, Y. Wang, P. Wang, W. Jin, and W. Ren, "MIR-Pump NIR-Probe Fiber-Optic Photothermal Spectroscopy With Background-Free First Harmonic Detection," IEEE Sensors Journal **20**, 12709-12715 (2020).

3. Y. Lin, W. Jin, F. Yang, J. Ma, C. Wang, H. L. Ho, and Y. Liu, "Pulsed photothermal interferometry for spectroscopic gas detection with hollow-core optical fibre," Sci Rep **6**, 39410 (2016).

4. J. Winefordner, "Photothermal Spectroscopy method for chemical analysis," (New York: Wiley, 1996).

5. K. A. Gillis, D. K. Havey, and J. T. Hodges, "Standard photoacoustic spectrometer: model and validation using O2 A-band spectra," Rev Sci Instrum **81**, 064902 (2010).

6. T. L. Cottrell, and J.-C. McCoubrey, *Molecular energy transfer in gases* (Butterworths, 1961).

7. H. Bao, Y. Hong, W. Jin, H. L. Ho, C. Wang, S. Gao, Y. Wang, and P. Wang, "Modeling and performance evaluation of in-line Fabry-Perot photothermal gas sensors with hollow-core optical fibers," Opt Express **28**, 5423-5435 (2020).

8. Y. L. Hoo, W. Jin, C. Shi, H. L. Ho, D. N. Wang, and S. C. Ruan, "Design and modeling of a photonic crystal fiber gas sensor," Applied Optics **42**, 3509-3515 (2003).

Chapter 5 Improving the precision and stability of PTI using fiber optic low-coherence interferometry

PTI has shown great potential as a cost-effective method for the detection of trace gases, offering remarkable sensitivity and specificity. However, it still falls short in applications such as the measurement of stable isotope ratios, which require high precision and stability. In this chapter, we demonstrate a novel technique, named LC-PTI for ultra-sensitive gas detection with remarkable precision and good stability.

5.1 Principle of LC-PTI

As illustrated in Fig. 5.1, the fiber optic LC-PTI consists of a pump laser, a BLS with coherence length L_C as the probe, a sensing interferometer and a reference interferometer. The sensing interferometer is an FPI which is the same as the one shown in Fig. 4.1. The length of the HCF, i.e., the FPI cavity length L, is however much longer than L_C, hence the two reflected beams would not interfere at the output of the FPI. The reflected probe beams are directed to a reference interferometer, i.e., a Michelson interferometer (MI), with OPD similar to that of the FPI. The MI is formed by two SMF-pigtailed Faraday rotator mirrors (FRMs) which is capable of suppressing the polarization fading [1]. Although the OPDs of the sensing and the reference interferometers both exceed the coherence length of the BLS, it is possible to make the differential OPD of the two interferometers within the coherence length of the BLS, which allows for effective interference between the 1st reflected probe beam which reaches the PD via the 4th reflector and the 2nd reflected probe beam which reaches the PD via the 3rd reflector.

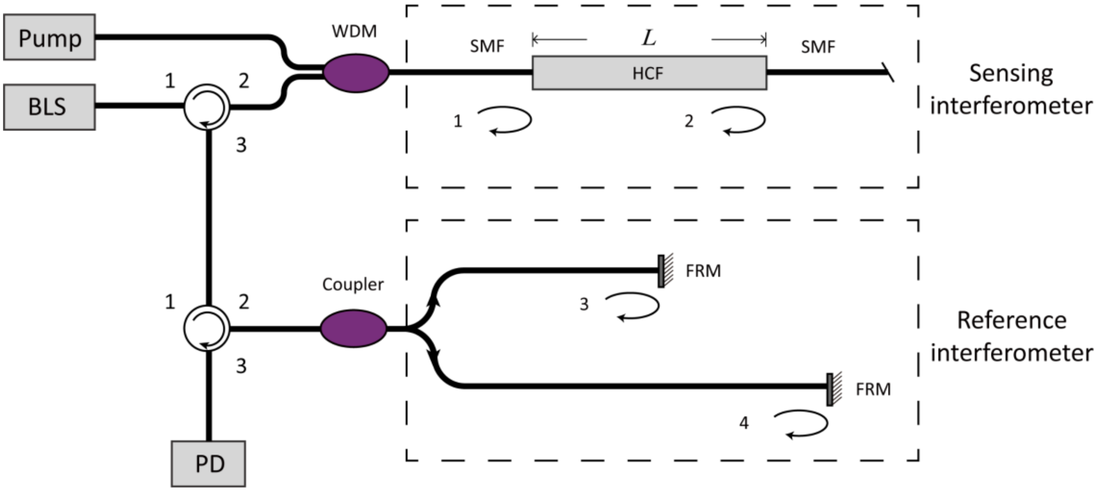

Fig. 5.1 Schematic diagram of the fiber optic LC-PTI.

By matching the OPD of the MI to that of the sensing FPI, the optical signal reaching the PD may be expressed as [2]:

$$I = \sum_{i,j} \left|E_{ij}\right|^2 + E_{23}E_{14}\gamma(\Delta L)cos\left(\frac{2\pi}{\lambda}\Delta L\right) \tag{5.1}$$

where E_{ij} is the amplitude of the probe beam at the PD arising from propagation via the ith reflective end of the FPI and the jth reflecting mirror of the MI, $\Delta L = L_{23} - L_{14}$ is the OPD between E_{23} and E_{14}, $\gamma(\Delta L)$ is coherence function of the source and λ is the probe wavelength. For a BLS with a Gaussian spectral profile, the detected interference signal of Eq. (5.1) is shown in Fig. 5.2(a). Any change in the ΔL results in a change in both the fringe visibility and the signal amplitude, which is contingent upon the coherence function of the probe BLS and decays rapidly as ΔL increases. For $\Delta L = L_{23} - L_{14} \approx 0$, the interference fringe has maximum visibility.

An optical pump laser beam, modulated in intensity, is directed into the FPI through a WDM, wherein its wavelength is adjusted to coincide with a gas absorption line. The WDM also acts as a filter for the reflected pump so that only the probe beam is directed to the reference interferometer via the circulator. Upon absorption of the pump beam by gas molecules within the HCF, heat is generated, subsequently altering the RI of the gas medium, which modulates OPD ($\Delta L_{PT} = 2\Delta n_{PT} L$) of the FPI and hence the phase difference (ϕ_{PT}) of the reflected probe beams as illustrated in Eq. (3.8).

To ensure the measurement of PT-phase modulation with maximum sensitivity, the LC-PTI can be operated around its phase quadrature point, where $2\pi\Delta L/\lambda = \pi/2$ or $\Delta L = \lambda/4$, as shown in Fig. 5.2(b). Under small signal approximation, i.e., $\phi_{PT} \ll 1$, the detected signal due to PT-phase modulation may be expressed as:

$$S = E_{23} E_{14} \gamma \phi_{PT} \tag{5.2}$$

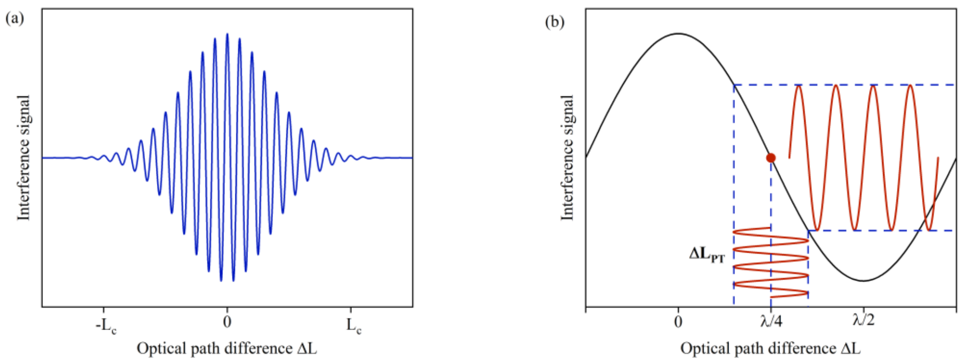

Fig. 5.2 (a) Interference pattern of the LC-PTI. (b) Illustration of interferometric output as a function of OPD near quadrature point of $\Delta L = \lambda/4$.

5.2 Gas detection with LC-PTI

5.2.1 Experimental setup

Fig. 5.3 depicts the experimental setup of the proposed LC-PTI for gas detection. The sensing FPI is constructed by mechanically splicing a 10-cm-long HC-CTF to two SMFs with ceramic ferrules and sleeves. The HC-CTF exhibits an outer cladding diameter of ~294 μm and a core diameter of 30.5 μm [3]. Small gaps of ~10 μm are kept at the splicing joints for gas filling. We use an ECDL operating at around 1532 nm as the pump. The pump is intensity modulated at 10 kHz by an acoustic-optic modulator (AOM) and amplified to about 500 mW by an erbium-doped fiber amplifier (EDFA). The probe beam is from a BLS with the bandwidth of ~20 nm and the center wavelength of 1550 nm. The pump and probe beams are combined with a WDM and co-propagating in the HC-CTF gas cell. The reflected probe beams from the FPI are guided into the MI via two optical circulators, which are reflected by the FRMs and the output from the MI is detected by a BD. A PZT with fiber around it is used in one arm of the MI to servo control the differential OPD $\Delta L = L_{23} - L_{14}$ to be $\lambda/4$, i.e., at the quadrature point of the interference fringe, to ensure maximum sensitivity for the gas detection. The first harmonic (1*f*) component at 10 kHz is demodulated by the LIA.

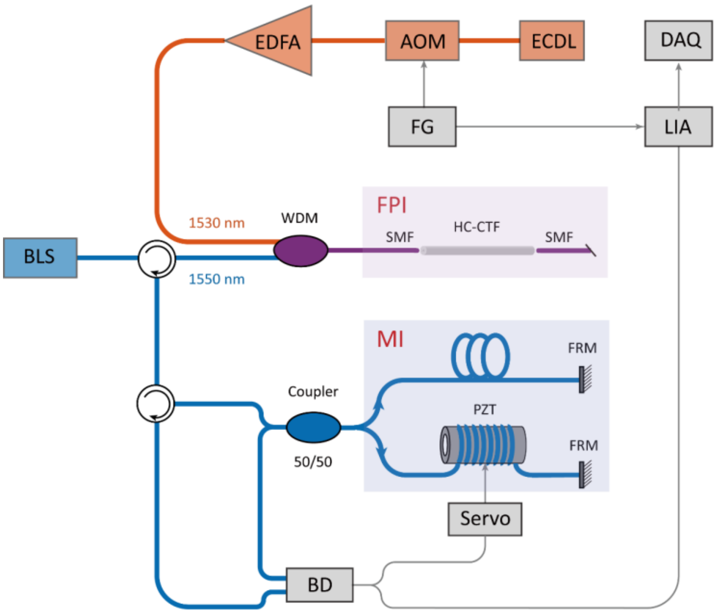

Fig. 5.3 Experimental setup for fiber optic LC-PTI gas detection. FG: function generator.

5.2.2 Limit of acetylene detection

Experiments were conducted with the LC-PTI filled with standard gas of 1000 ppm acetylene balanced in nitrogen at atmospheric pressure. Fig. 5.4(a) presents the detected 1*f* signal as the pump wavelength is tuned across the acetylene absorption line at 1531.59 nm. To assess the system noise, the gas cell was filled with pure nitrogen. With the EDFA output power of ~500 mW, the NEC for acetylene detection is ~8 ppb for a lock-in time constant of 1 s. Fig. 5.4(b) shows the p.p. values of the 1*f* signal and the s.d. of the detection noise for different pump power levels delivered into the HCF. The amplitude of the PT signal exhibits a linear relationship with the pump power, while the s.d. of the noise remains nearly constant.

Allan deviation analysis was also performed with the background noise over a duration of 90 minutes, as shown in Fig. 5.4(c). The measurement involved tuning the pump wavelength to 1531.59 nm, while the HC-CTF-based gas cell was filled with pure nitrogen. The optimal averaging time is ~600 s, resulting in a noise level of ~ 0.6 μV. The corresponding NEC for the SNR of unity is estimated to be 0.7 ppb. The NEC for 100 s averaging time is 2.2 ppb.

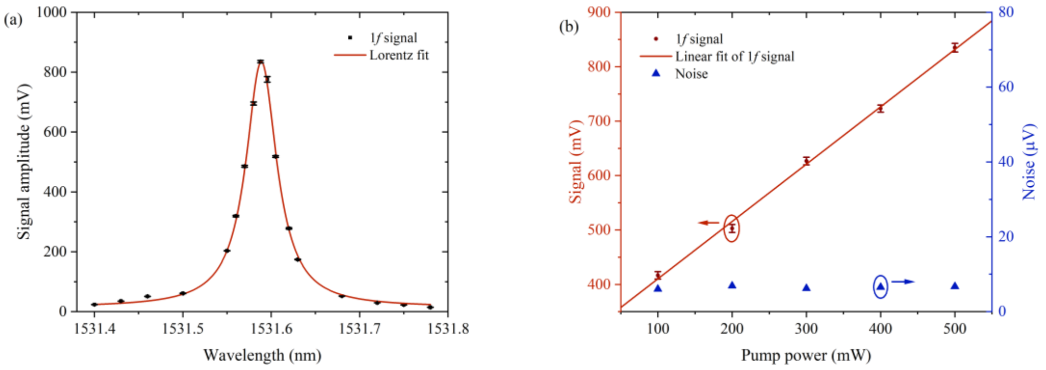

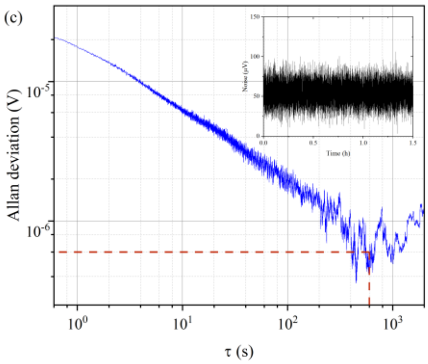

Fig. 5.4 (a) The demodulated 1f PT signal as the pump wavelength is tuned across the acetylene absorption line at 1531.59 nm. The error bars, which represent the s.d. from the 1-min measurement, are multiplied by a factor of five for improved clarity. (b) The p.p. value of the 1f signal and the s.d. of the detection noise as functions of the pump power level. The error bars, which represent the s.d. from the 1-min measurement, are multiplied by a factor of ten for improved clarity. (c) The Allan-Werle plot utilizing the noise data over a duration of 90 minutes.

5.2.3 Measurement precision

The measurement precision of a sensing system refers to the extent to which repeated measurements conducted under consistent conditions yield consistent outcomes, and it is associated with the presence of random measurement errors [4]. The precision of the LC-PTI is evaluated by its relative measurement error, which is estimated by the 1σ value of the distribution of the recorded signal amplitudes [5, 6]. Fig. 5.5(a) depicts a sequence of 4000 consecutive data points acquired over a duration of approximately 5 minutes, during which the pump wavelength remains fixed at the center of the P (11) absorption line of acetylene near 1531.59 nm. The normalized signal amplitudes of the measurements follow Gaussian distribution with 1σ of 0.025%, which is even better than that of mass spectrometer [6].

For comparison, we also evaluated the measurement precision of a PTI system powered by a narrow linewidth probe laser with coherence length of 100 m. Without the reference MI, the PT phase modulation is directly measured by the same 10-cm-long FPI [7]. Other experimental conditions are identical to that of LC-PTI system with the BLS. Fig. 5.5(b) shows the 4000 consecutive measured data points from each of systems. The normalized signal amplitudes of the measurements for the PTI system with narrow linewidth probe laser source also follow the Gaussian distribution with 1σ of 0.94%, which is nearly 40 times larger than that of the LC-PTI system.

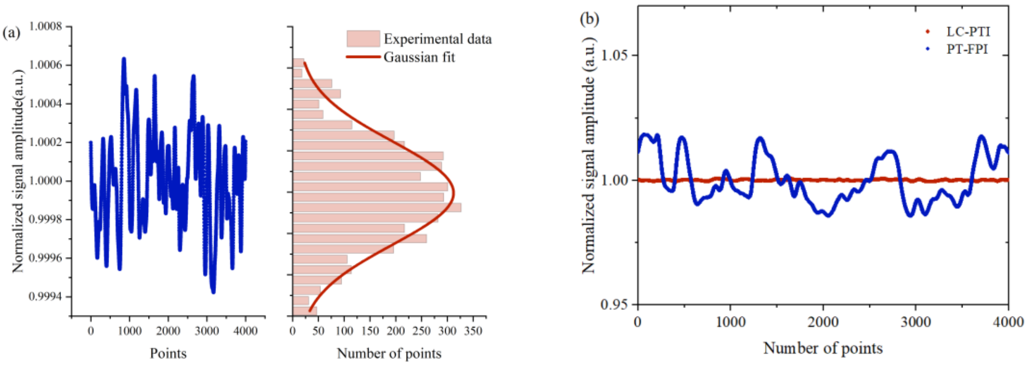

Fig. 5.5 (a) The normalized signal amplitude for the LC-PTI system with corresponding Gaussian distribution. (b) Comparison of the normalized signal amplitudes of 4000 consecutive measured data points for the PTI with narrow linewidth probe and LC-PTI systems.

5.3 Long-term stability

In this section, we demonstrate gas detection with improved long-term stability using the LC-PTI theoretically and experimentally.

The detected signal is proportional to P_{pump}. To ensure sustained and reliable gas detection, it is critical to maintain stable pump power within the HCF. Since the gas absorption line is narrow and a narrow linewidth pump laser is needed for efficient absorption spectroscopy, the pump power in the HCF may be expressed as [8]:

$$P_{pump} = \frac{t^2}{1 + r^4 - 2r^2 cos(\theta)} P_{pump,in} \tag{5.3}$$

where r and t are respectively the reflection and transmission coefficients of the FPI reflectors, which are assumed to be the same for both ends; $\theta = 4\pi L/\lambda$ is the single-pass phase shift of the FPI, and $P_{pump,in}$ is the pump power before getting into the FPI. P_{pump} could fluctuate due to changes in $P_{pump,in}$ and θ. The latter is sensitive to environmental perturbation such as temperature, vibration and gas flow, which may lead to significant pump power fluctuation in the FPI. Fig. 5.6(a) shows the calculated variation of the pump power within the FPI when the length is varied. The power fluctuation can be as high as 16% for the reflectance r^2 =4%. Even the reflectance is reduced down to 0.2% with anti-reflection coatings, there is still a 1% fluctuation in the pump power, as depicted in Fig. 5.6(b).

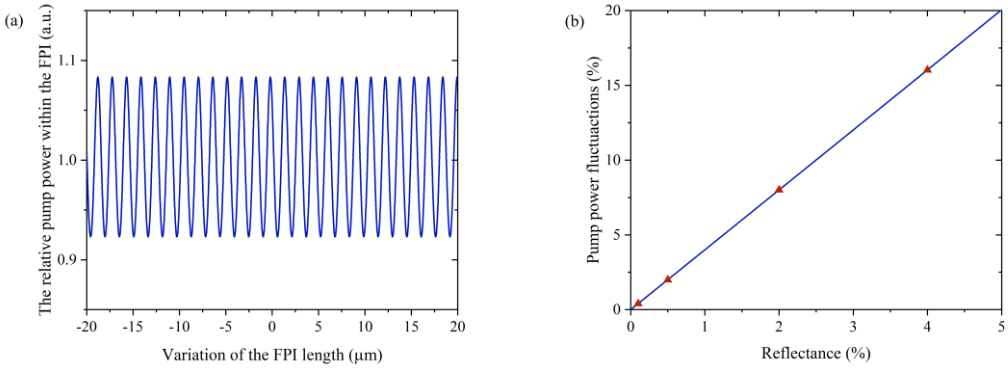

Fig. 5.6 (a) Calculated relative pump power variation within the FPI with optical path length, assuming reflectance of both ends is 4%. (b) Maximum pump power fluctuation as a function of the reflectance.

Fortunately, it is possible to stabilize the pump power within the FPI by actively adjusting the length of the FPI to balance the impact of environmental perturbation. In fact, if the transmitted pump power is monitored and maintained at a constant level by a servo-loop, both the effect of environmental perturbation to the FPI length and the input pump power fluctuation may be mitigated.

In the previous section, the measurement precision of LC-PTI was evaluated over a period of 5 min. Over such a short period, the pump power fluctuation due to environmental perturbation to the FPI and source power variation as well as the probe power variation is insignificant. We demonstrate gas detection with improved long-term stability by servo-controlling the pump power in the FPI and monitoring the probe power fluctuation to minimize its effect on the detected PT signal.

As shown in Fig. 5.7, a section of the HC-CTF forming the FPI is mounted on a PZT to stretch the HC-CTF according to the detected transmitted pump power. The variation of the DC component from the PD1 is used as an error signal to stabilize the pump power. At the same time, the power level of the BLS is detected by PD2 and used as a reference to compensate the probe power variation.

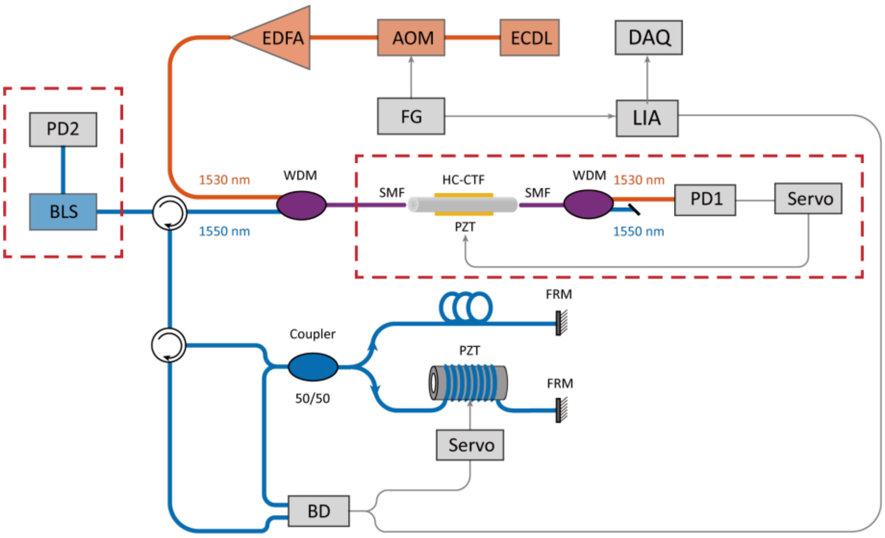

Fig. 5.7 Experimental setup for long-term stability of the LC-PTI-based gas detection.

Fig. 5.8(a) depicts the detected fluctuation of pump power P_{out} at PD1 as the FPI length is stretched by the PZT. P_{out} is related to the pump power P_{pump} within the FPI by $P_{out} =$

tP_{pump}. The pump power fluctuation can reach to ~15%, indicating that environmental perturbations could cause significant change of the pump power in the HCF. The detected pump power change is ~0.1% after stabilization by using the servo-loop.

We then conducted the gas detection measurement by fixing the pump wavelength to the center of the P (11) absorption line of acetylene near 1531.59 nm with 1000 ppm acetylene balanced with nitrogen. We simultaneously detected the $1f$ signal from the LIA and the slow-varying component induced by the probe power variation from the PD2. The peak value of the PT signal has a similar trend as the probe power drift and hence can be compensated by multiplying a compensation factor, which can be obtained by fitting the relationship between the $1f$ signal and the probe power. With the pump stabilization and the probe compensation, the peak value of the PT signal fluctuation over a period of 3 hours is $\pm 0.038\%$ for the average time of 10 min, as shown in Fig. 5.8(b). This is nearly 10 times better than the state-of-art PTI gas detection system, to our best knowledge [9].

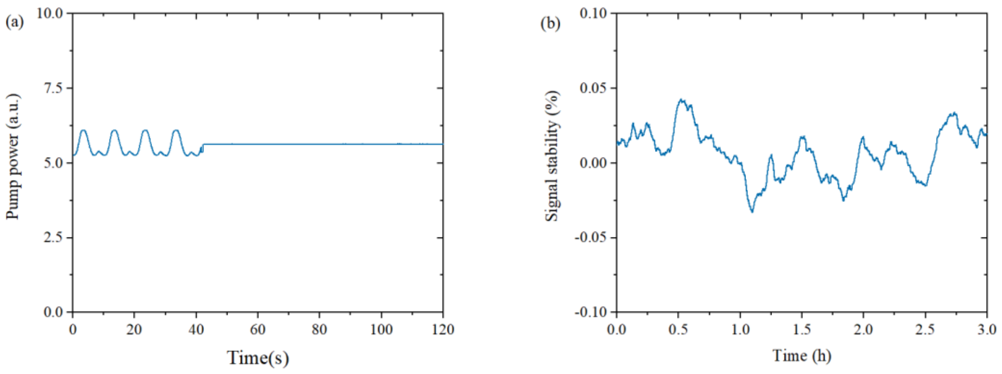

Fig. 5.8 (a) The detected pump power from PD1 when the PZT is stretched (0 to 43 s) and when it is stabilized via the servo-loop (43 to 120 s). (b) The relative fluctuation of PT signal with pump power stabilization and probe power compensation.

5.4 Measurement of acetylene isotope ratio

Measurement of stable isotope ratios is critical in chemistry [10]. Current solution to determine the ratio of stable isotope is to use isotope ratio mass spectrometers (IRMS). However, isotope ratio measurement with IRMS may be interfered by isobars with identical values of *m*/*z*, e.g., $^{34}S^{16}O^{16}O/^{32}S^{18}O^{16}O$ and $H^{12}C^{13}CH/H^{12}C^{12}CD$ [5]. Laser spectroscopic techniques can resolve this problem due to its immunity to isobaric interference. Here, we demonstrate high-precision measurement of $^{13}C/^{12}C$ isotope ratio of acetylene with LC-PTI.

The absorption coefficients of the P (10) line of 977.6 ppm $H^{12}C^{12}CH$ near 1530.9 nm and the P (5) line of 21.9 ppm $H^{12}C^{13}CH$ near 1531.1 nm are 3.95×10^{-4} cm^{-1} and 1×10^{-5} cm^{-1}, respectively. The small absorption coefficients make highly sensitive detection a requirement. Fig. 5.9(a) illustrates the computed absorption spectrum of acetylene with natural abundance near 1.53 μm with data acquired from HITRAN [11]. It is noted that $H^{12}C^{12}CD$ has negligible absorptions near 1.53 μm which would not interfere the isotope ratio measurement [11, 12].

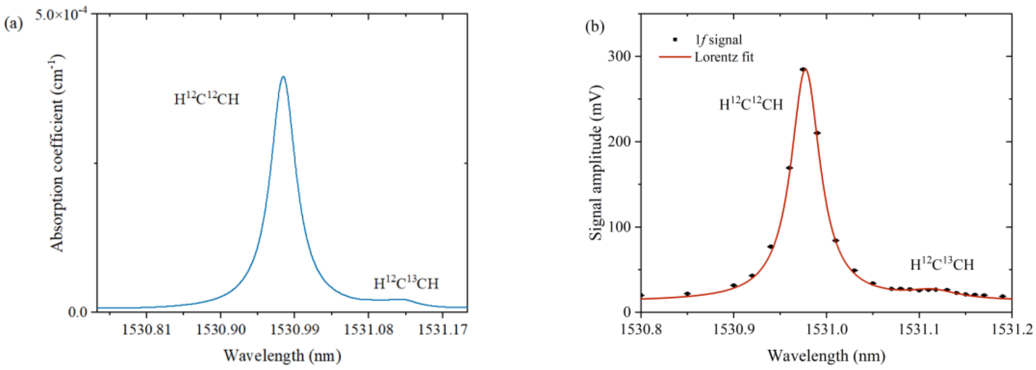

Fig. 5.9 (a) The calculated and (b) the measured absorption lines of $H^{12}C^{12}CH$ *and* $H^{12}C^{13}CH$ *with LC-PTI near 1531 nm. The error bars, which represent the s.d. from the 1-min measurement, are multiplied by a factor of five for improved clarity.*

The measurement was conducted utilizing the identical experimental configuration depicted in Fig. 5.7, where the gas cell was filled with a 1000 ppm acetylene concentration. The pump power out of the EDFA is 500 mW. Fig. 5.9(b) depicts the measured absorption lines of $H^{12}C^{12}CH$ and $H^{12}C^{13}CH$ with the LC-PTI. The isotope ratio of $^{13}C/^{12}C$ is determined by adopting δ notion as [5]:

$$\delta^{13}C = R_{sample}/R_{\mathrm{standard}} - 1 \tag{5.4}$$

where R_{sample} is the $^{13}C/^{12}C$ isotope ratio of the measurement and we use the mean value of the measurement as R_{standard} to evaluate the measurement precision due to the lack of knowledge of isotope ratio in the gas sample. Fig. 5.10 shows 10 values of the measured $\delta^{13}C$, each of which is determined from 100 sets of consecutive measurement data. The precision (1σ value) of the 10 $\delta^{13}C$ measurements is 0.01% which is comparable to IRMS [5, 13].

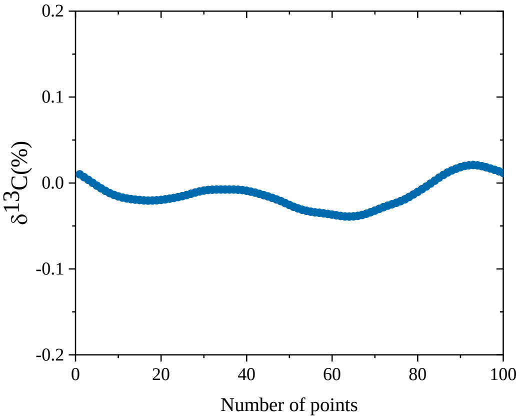

Fig. 5.10 Measured δ^{13}C *values for 1000 ppm acetylene.*

5.5 Discussion

One of the main limitations on the measurement precision of a PTI gas detection system is the phase error resulting from parasitic interferences caused by reflections and backward scatterings, which increase the noise level, cause variation in interference fringe visibility and fluctuation in the operating point of the optical interferometer. Considering a typical configuration of FPI system shown in Fig. 5.11, ideally only the probe beams reflected from the two ends of the FPI with the reflection coefficients of r_1 and r_2, i.e., $r_1E_0e^{j\varphi_1}$ and $r_2E_0e^{j\varphi_2}$ would interfere with each other, where E_0 is the intensity of the incident probe beam, φ_1 and φ_2 are the phase of the reflected probe beams, respectively. When a pump beam is coupled into the FPI, the phase difference of the reflected probe beams is modulated, i.e., $\varphi_2 - \varphi_1 = \phi_0 + \phi_{PT}$, where $\phi_0 = 4\pi L/\lambda$ is the static phase difference.

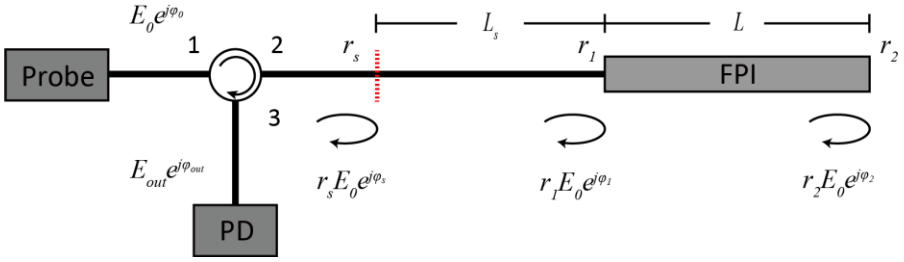

Fig. 5.11 Schematic diagram of a typical FPI gas detection system with a parasitic reflection.

Assume that there is a parasitic reflection $r_sE_0e^{j\varphi_s}$, where r_s and φ_s are the reflection coefficient and phase of the parasitic reflection, there will be three reflected beams involved in the interference process as indicated in Fig. 5.11. The light intensity received by PD may be expressed as:

$$\begin{aligned} I_{out} &= \langle E_{out} \cdot E_{out}^{*} \rangle \\ &= |E_0|^2 \begin{bmatrix} (r_1^2 + r_2^2 + r_s^2) + 2r_1r_2\gamma(L)\cos(\phi_0 + |\phi_{PT}|\sin(\omega t)) \\ +2r_1r_s\gamma(L_s)\cos(\phi_s) + 2r_2r_s\gamma(L+L_s)\cos(\phi_0 + \phi_s + |\phi_{PT}|\sin(\omega t)) \end{bmatrix} \end{aligned} \tag{5.5}$$

where $|\phi_{PT}|$ is the amplitude of the PT-induced phase modulation, ω is the angular modulation frequency, $\phi_s = \varphi_1 - \varphi_s$ is the spurious phase difference which is sensitive to the environmental perturbation and L_s is the distance from the spurious reflection point to the first end of the FPI. The first term in Eq. (5.5) is a summation of reflected light intensities, its spectrum is primarily determined by the noise spectrum of the probe source. The second term is the signal term, and the third and the fourth terms are due to parasitic interference. For properly designed system with low parasitic reflection, we can assume $r_s \ll r_1,\ r_2$, hence the magnitude of the third and fourth terms are significantly smaller than that of the signal term. Under such a condition, it is possible to maintain the operation around the quadrature point, i.e., $\phi_0 = \pi/2$ by a servo-loop [14].

Now considering a probe source with a long coherence length, i.e., $L_c \gg L + L_s,\ \gamma(L) = \gamma(L_s) = \gamma(L + L_s) = 1$, assume that $|\phi_{PT}| \ll 1$, we have:

$$\begin{aligned} I_{out} &= |E_0|^2 \begin{bmatrix} (r_1^2 + r_2^2 + r_s^2) - 2r_1 r_2 \sin(|\phi_{PT}| \sin(\omega t)) \\ +2r_1 r_s \cos(\phi_s) - 2r_2 r_s \sin(\phi_s + |\phi_{PT}| \sin(\omega t)) \end{bmatrix} \\ &= |E_0|^2 \begin{bmatrix} (r_1^2 + r_2^2 + r_s^2) - 2r_1 r_2 |\phi_{PT}| \sin(\omega t) \\ +2r_1 r_s \cos(\phi_s) - 2r_2 r_s \sin(\phi_s) - 2r_2 r_s \cos(\phi_s)\, |\phi_{PT}| \sin(\omega t) \end{bmatrix} \end{aligned} \tag{5.6}$$

If now the first harmonic signal of the pump modulation is detected, the amplitude of PT phase modulation signal derived from Eq. (5.6) would be:

$$S = \underbrace{K_0 |\phi_{PT}| \sin(\omega t)}_{signal} + \underbrace{K_N |\phi_{PT}| \sin(\omega t) + N}_{Noise} \tag{5.7}$$

where $K_0 = 2|E_0|^2 r_1 r_2$ is the scale factor for signal detection. $K_N = 2|E_0|^2 r_2 r_s \cos(\phi_s)$ represents a noise term that is proportional to the PT-induced phase modulation and hence gas concentration. The variation of K_N can be large due to stronger spurious interference, which is sensitive to environmental perturbations, increasing the detected noise. N represents noise terms independent of gas concentration, which contains components of $|E_0|^2[(r_1^2 + r_2^2 + r_s^2) + 2r_1 r_s \cos(\phi_s) - 2r_2 r_s \sin(\phi_s)]$ at detection frequency $\omega = 2\pi f$.

The measurement precision may be expressed as:

$$\varepsilon = \frac{\sigma(S)}{\bar{S}} \approx \frac{r_s}{r_1}\sigma[\cos(\phi_s)] + \frac{\sigma(N)}{K_0|\phi_{PT}|} \tag{5.8}$$

where σ represents the s.d. value. From Eq. (5.8), it is obvious that the measurement precision is influenced by two factors, namely the variation of K_N and N present in the system. Specifically, when the gas concentration is relatively high and $K_0|\phi_{PT}| \gg N$, the first term proportional to $\sigma[\cos(\phi_s)]$ in Eq. (5.8) plays a dominant role in determining the measurement precision, which is independent of gas concentration. In contrast, for low gas concentrations and small values of $K_0|\phi_{PT}|$, the impact of system noise N is more significant in determining the precision of the measurement. The system measurement precision is inversely proportional to gas concentration.

With a BLS of a short coherence length, i.e., $L_c \ll L, L_s$, if a reference interferometer with OPD matched to that of the FPI is used, the PT signal may be maximized while the parasitic interference terms, i.e., the third and the fourth terms in Eq. (5.5), are minimized with $K_N \approx 0$ in Eq. (5.7), indicating that the measurement precision of LC-PTI can be significantly better than that of the PTI with a narrow linewidth probe laser.

To verify the theoretical analysis, we conducted further experiments to compare measurement precisions for PTI systems with a narrow linewidth probe and a BLS, and the results are presented in Fig. 5.12. During the experiments, the pump wavelength is fixed at 1531.59 nm and the gas cell is filled with 5, 10, 100 and 1000 ppm acetylene balanced in nitrogen at atmospheric pressure. The measurement precision is determined by dividing 4000 measured data points to its mean value with detection bandwidth of 0.094 Hz.

It is evident that the measurement precision for PTI with BLS is significantly better than that with the narrow linewidth probe. The measurement precision remains relatively constant when the acetylene concentration is high. However, when the acetylene concentration drops below 10 ppm, the amplitude of signal variation gradually approaches that of the system noise, leading to a decrease in measurement precision. The overall trend of the measured system precision with gas concentration is in good agreement with the theoretical analysis.

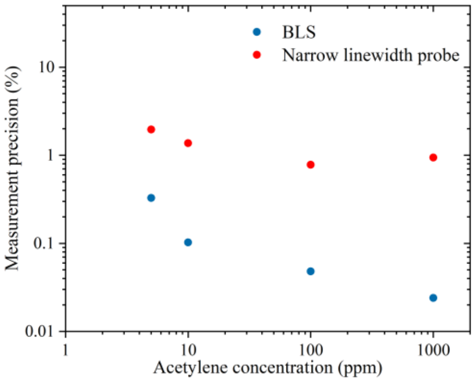

Fig. 5.12 The measurement precision for PTI system powered by BLS and narrow linewidth probe with different acetylene concentrations.

5.6 Conclusion

To conclude, we have demonstrated a novel gas detection method based on LC-PTI with a NEC of 0.7 ppb for acetylene detection. By stabilising the pump power within the HCF and compensating the drift resulting from probe power variation, the signal instability over a 3-hour period is found to be ±0.038%, which is an improvement of ten times over exiting PTI gas detection systems. We also demonstrate the measurement of the $^{13}C/^{12}C$ isotope ratio of acetylene with a measurement precision of approximately 0.01%. The results indicate the potential of LC-PTI as an alternative to mass spectrometers for reliable gas detection in compact form, harsh environmental applicability, and remote sensing capabilities.

Reference of Chapter 5

1. A. Kersey, M. Marrone, and M. Davis, "Polarisation-insensitive fibre optic Michelson interferometer," Electronics letters **27**, 518-520 (1991).
2. A. S. Gerges, T. Newson, and D. Jackson, "Coherence tuned fiber optic sensing system, with self-initialization, based on a multimode laser diode," Applied optics **29**, 4473-4480 (1990).
3. H. Bao, W. Jin, Y. Hong, H. L. Ho, S. Gao, and Y. Wang, "Phase-Modulation-Amplifying Hollow-Core Fiber Photothermal Interferometry for Ultrasensitive Gas Sensing," Journal of Lightwave Technology **40**, 313-322 (2022).
4. J. Taylor, *Introduction to error analysis, the study of uncertainties in physical measurements* (1997).

5. R. N. Zare, D. S. Kuramoto, C. Haase, S. M. Tan, E. R. Crosson, and N. M. Saad, "High-precision optical measurements of 13C/12C isotope ratios in organic compounds at natural abundance," Proceedings of the National Academy of Sciences **106**, 10928-10932 (2009).

6. T. M. Kana, C. Darkangelo, M. D. Hunt, J. B. Oldham, G. E. Bennett, and J. C. Cornwell, "Membrane inlet mass spectrometer for rapid high-precision determination of N2, O2, and Ar in environmental water samples," Analytical chemistry **66**, 4166-4170 (1994).

7. F. Liu, H. Bao, H. L. Ho, W. Jin, S. Gao, and Y. Wang, "Multicomponent trace gas detection with hollow-core fiber photothermal interferometry and time-division multiplexing," Optics Express **29**, 43445-43453 (2021).

8. M. B. G. Bram J. J. Slagmolen, Karl G. Baigent, and David E. McClelland, "Phase-sensitive reflection technique for characterization of a Fabry–Perot interferometer," Applied Optics **39** (2000).

9. P. Zhao, Y. Zhao, H. Bao, H. L. Ho, W. Jin, S. Fan, S. Gao, Y. Wang, and P. Wang, "Mode-phase-difference photothermal spectroscopy for gas detection with an anti-resonant hollow-core optical fiber," Nat Commun **11**, 847 (2020).

10. J. Bigeleisen, "Chemistry of Isotopes: Isotope chemistry has opened new areas of chemical physics, geochemistry, and molecular biology," Science **147**, 463-471 (1965).

11. I. Gordon, L. Rothman, R. Hargreaves, R. Hashemi, E. Karlovets, F. Skinner, E. Conway, C. Hill, R. Kochanov, and Y. Tan, "The HITRAN2020 molecular spectroscopic database," Journal of quantitative spectroscopy and radiative transfer **277**, 107949 (2022).

12. O. Lyulin, S. Vasilchenko, D. Mondelain, S. Kassi, and A. Campargue, "The acetylene spectrum in the 1.45 µm window (6627–7065 cm–1)," Journal of Quantitative Spectroscopy and Radiative Transfer **253**, 107057 (2020).

13. S. Jiang, F. Chen, S. Gao, Y. Wang, H. L. Ho, and W. Jin, "Precision Measurement of Carbon Dioxide Isotope Ratio and Ammonia based on Photo-thermal Spectroscopy in a Hollow-Core Fiber," in *Optical Fiber Sensors*(Optica Publishing Group2022), p. Th1. 5.

14. H. Bao, Y. Hong, W. Jin, H. L. Ho, C. Wang, S. Gao, Y. Wang, and P. Wang, "Modeling and performance evaluation of in-line Fabry-Perot photothermal gas sensors with hollow-core optical fibers," Opt Express **28**, 5423-5435 (2020).

Chapter 6 Enhancing the performance of PTI by optical phase modulation amplification

This chapter showcases two demonstrations of OPMA techniques aimed at improving the sensitivity of PTI. The first approach involves wavelength locking of a probe laser to the resonance of an HCF resonating cavity. Another is to employ a DMI operating at destructive interference.

6.1 OPMA with a resonating cavity

The technique of locking the laser wavelength to a resonance cavity has proven effective in enhancing the effective length of light-gas interaction, resulting in significantly improved NEC values [1-3]. However, these systems use open-path optical cavities with high finesse (e.g., >1000), which are bulky and require intricate alignment procedures. Here, we demonstrate amplification of the PT phase modulation by a factor equivalent to the cavity finesse by locking the probe wavelength to the center of the resonance of a high-finesse HCF cavity.

6.1.1 Principle of OPMA in an HCF FP cavity

The basic principle of OPMA in an HCF FP cavity may be explained by using Fig. 6.1. When an incident probe beam $\boldsymbol{E_i}$ is coupled into the cavity, the reflected and transmitted fields ($\boldsymbol{E_r}$, $\boldsymbol{E_t}$) may be expressed as [4]:

$$\boldsymbol{E_r} = |E_r|\exp(-i\phi_r) = \frac{r_{in} - r_{out}\left(r_{in}^2 + t_{in}^2\right)\exp(-i2\theta)}{1 - r_{in}r_{out}\exp(-i2\theta)}\boldsymbol{E_i} \tag{6.1}$$

$$\boldsymbol{E_t} = |E_t|\exp(-i\phi_t) = \frac{t_{in}t_{out}\exp(-i\theta)}{1 - r_{in}r_{out}\exp(-i2\theta)}\boldsymbol{E_i} \tag{6.2}$$

where r_{in}, r_{out}, t_{in} and t_{out} are the reflection and transmission coefficients of the first and second mirrors, respectively; ϕ_r and ϕ_t are the phases of the reflected and transmitted fields; $\theta = 2\pi nL/\lambda_{probe}$ is the single-pass phase shift through the cavity length L, n is the effective RI of HCF's fundamental mode. Fig. 6.1(b) depicts the amplitude and the phase of the reflected and transmitted beams as functions of θ near a cavity resonance $\theta = N\pi$, where N is an integer.

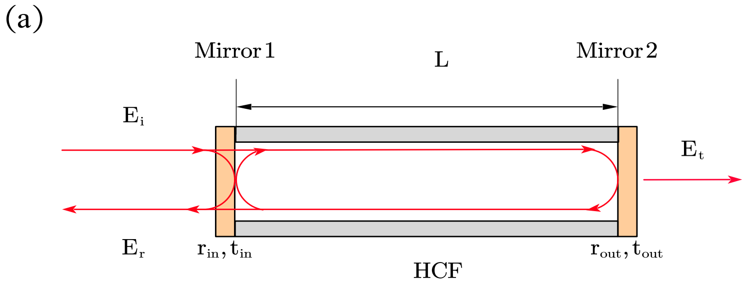

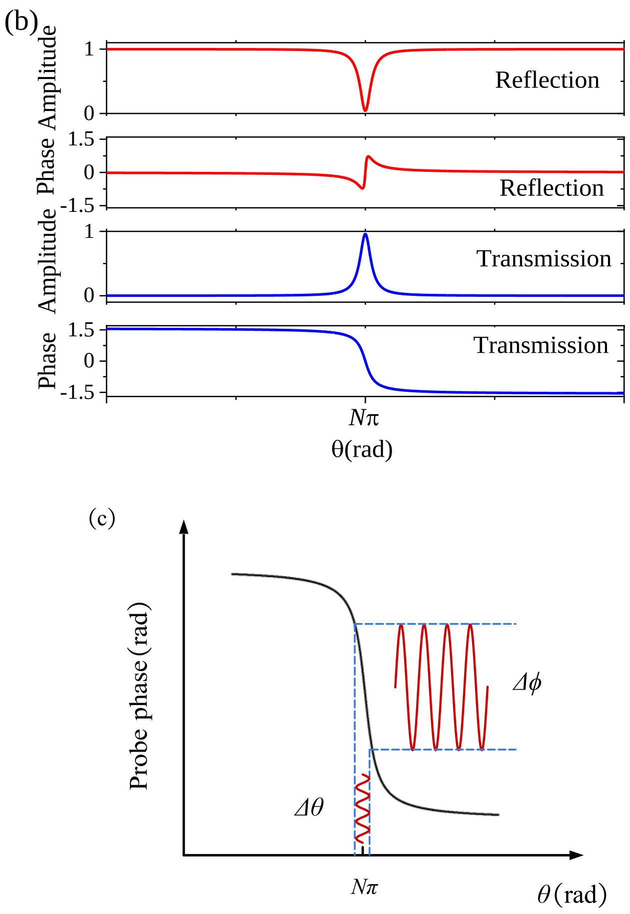

Fig. 6.1 Principle of OPMA in an HCF FP cavity. (a) The incident, transmitted and reflected light fields in an HCF FP cavity. (b) Amplitude and phase of the reflected and transmitted light fields as functions of the single-pass phase shift θ *near a cavity resonance for* $r_{in}^2 = 0.98$ *and* $r_{out}^2 = 0.97$. *(c) Schematic showing the OPMA effect near a cavity resonance.*

Near a cavity resonance $\theta = N\pi$, the reflected and transmitted beams experience dramatic phase changes. For simplicity, we assume that the mirror reflectivity is close to 1 and the cavity loss is negligible, then the slopes of the phase changes for the reflected and transmitted beams at cavity resonance may be approximated by:

$$k_r = \frac{d\phi_r}{d\theta} \approx \frac{F}{\pi}\frac{2t_{in}^2}{r_{in} - r_{out}} \tag{6.3}$$

$$k_t = \frac{d\phi_t}{d\theta} \approx -\frac{4F}{\pi} \tag{6.4}$$

Hence, a small baseline phase modulation ($\Delta\theta$) will be transformed into a large phase modulation ($\Delta\phi$) for the reflected (ϕ_r) or transmitted (ϕ_t) beam, as shown in Fig. 6.1(c). The amplifying factors (i.e., k_r and k_t) are proportional to the cavity finesse $F = \pi\sqrt{r_{in}r_{out}}/(1 - r_{in}r_{out})$. k_r is also inversely proportional to $r_{in} - r_{out}$, which could be further increased by making $r_{in} \approx r_{out}$. Note that k_r and k_t can have the same or opposite signs, depending on the relative values of r_{in} and r_{out}. The amplified phase modulation, i.e., $\Delta\phi_{r/t} = k_{r/t}\Delta\theta$, can be detected using optical fiber interferometry, which enables higher detection sensitivity for $\Delta\theta$.

When a modulated pump beam propagates in the FP cavity, gas absorption of the pump results in heating, which modulates the RI of the gas material and hence the phase of the probe beam propagating in the HCF. Consider firstly a non-resonant configuration where the mirror reflection coefficient (r_{in}, r_{out}) is low for the pump beam, the baseline probe phase modulation may be regarded as due to absorption of a single-pass pump beam through the HCF and expressed as Eq. (3.8).

If the mirror reflectivity is high for the pump beam, the pump field would resonate in the cavity, resulting in higher accumulated pump power in the cavity and hence enhanced PT phase modulation. At the cavity resonance, the baseline phase modulation of the probe beam may be expressed as [5]:

$$\Delta\theta = \frac{F}{\pi}\phi_{PT} \tag{6.5}$$

Both the single-pass and resonant pump configurations can be used in combination with the OPMA of the probe to achieve ultra-sensitive gas detection.

6.1.2 Construction of an HCF FP cavity

Fig. 6.2(a) illustrates an HCF FP cavity gas cell. The HCF is the same HC-CTF as used in Section 4.2.1. The spectral transmission and cross-section image of the HC-CTF can be found in Fig. 4.10 (b). The FP cavity is formed by sandwiching a ~10-cm-long HCF between the mirrored ends of two standard SMFs. The SMFs and the HCF are joined together by mechanical splicing with small air gaps between them.

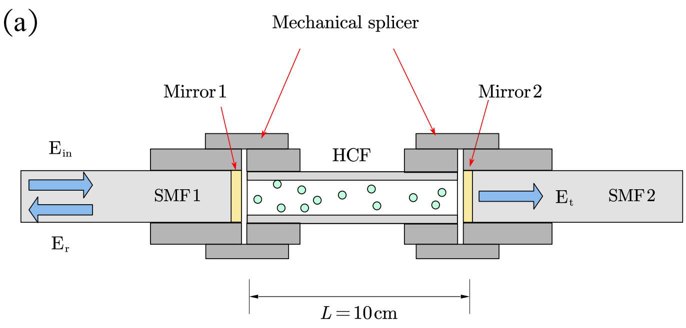

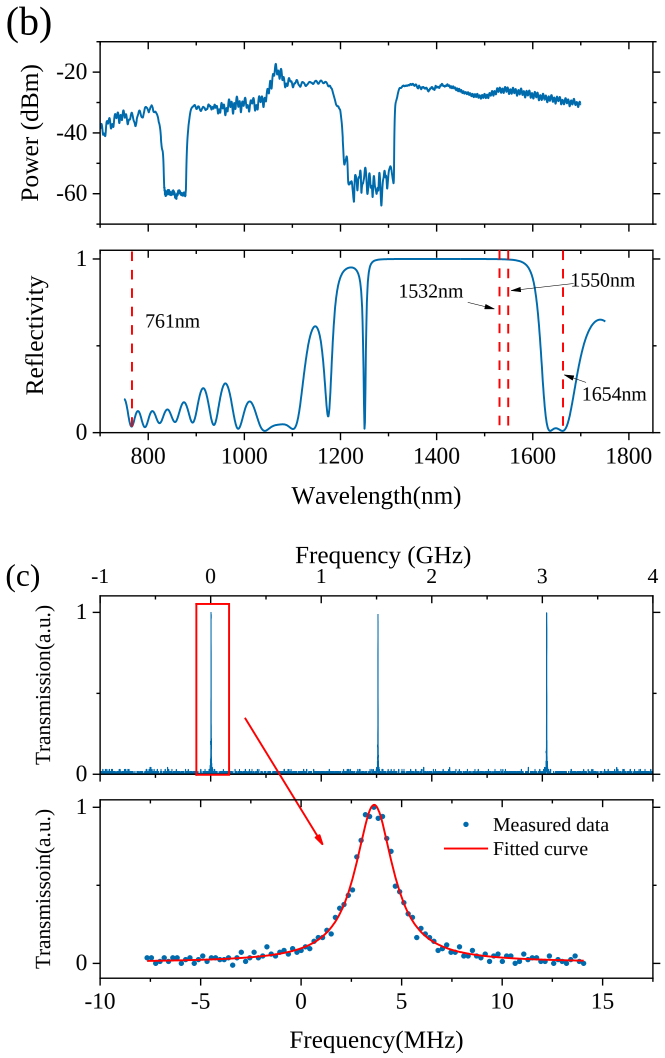

Fig. 6.2. (a) Schematic of an HCF FP cavity. (b) The spectrums of the HCF transmission (upper panel) and the mirror reflectivity (lower panel). (c) The normalized transmission of a 10-cm-long HCF FP cavity measured by scanning the laser wavelength around 1550.3 nm.

The reflectivity of the mirrored end as a function of wavelength is shown in the lower panel of Fig. 6.2(b). The mirror reflectivity is >99.5% from 1250 -1570 nm, which enables the formation of a high finesse HCF FP cavity in this wavelength range. Fig. 6.2(c) shows the transmission of the HCF cavity around 1550.3 nm, which is selected as the probe wavelength. The FSR is measured to be ~1.5 GHz and the linewidth of the cavity resonance is 2.2 MHz, giving a cavity finesse of ~700. At 1654 nm and 761 nm, which are respectively selected as the pump wavelengths for methane and oxygen detection, the mirror reflectivity is ~1% and ~4%. Hence, at these wavelengths, the PT phase modulation may be regarded as due to a single-pass of the pump through the gas-filled HCF. At 1532 nm, which is selected as the pump wavelength for acetylene detection, the pump is resonating in the cavity and the PT phase modulation is given by Eq. (6.5).

6.1.3 Methane and oxygen detection

Using the gas cell depicted in Fig. 6.2(a), we conducted experiments to detect methane and oxygen. The experimental setup employed is illustrated in Fig. 6.3. The probe beam is generated by a narrow linewidth (<5kHz) fiber laser with wavelength of 1550.3 nm, which is away from absorption lines of gases to be detected in the experiments. The probe wavelength is locked to the center of the cavity resonance using the Pound-Drever-Hall (PDH) method [6]. By operating the probe at the resonance, the baseline probe phase modulation resulting from the absorption of the pump is amplified at the transmitted (E_t^{probe}) and the reflected (E_r^{probe}) outputs. The amplified phase modulation is detected by combing the transmitted and reflected probe beams to form a two-beam MZI like all-fiber interferometer, which detects the phase difference between the transmitted and the reflected beams, i.e., $\Delta\phi = (k_r - k_t)\Delta\theta = G_s\Delta\theta$. The reflectance of the mirrors can be selected so that the phases of the reflected and transmitted beams are of opposite signs, ensuring the differential phase is always larger than those of the individual beams. The MZI is stabilized at quadrature with an active servo loop using a PZT phase modulator. The relative signs of phase modulation can be determined experimentally. The outputs of the MZI are detected by a BD and, the first or second harmonic component is demodulated as the PT signal by a LIA.

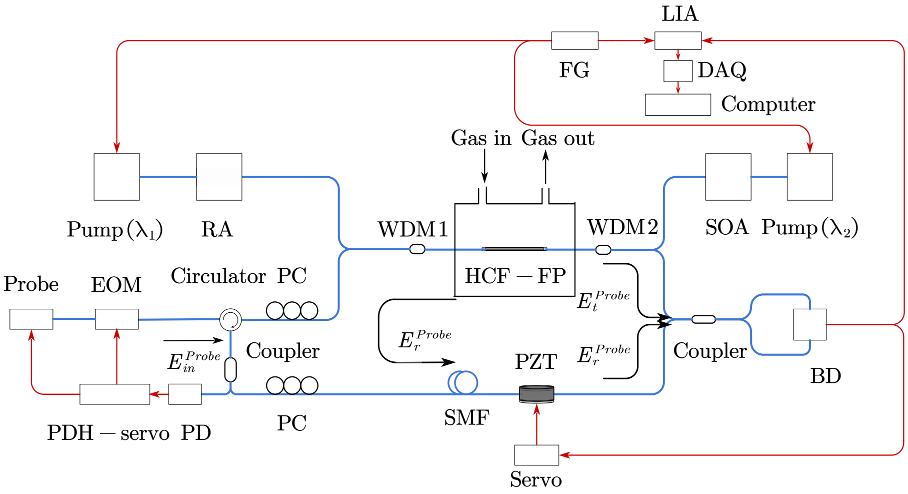

Fig. 6.3 Experimental setup for methane and oxygen detection based on OPMA with an FP cavity. EOM: electro-optical modulator.

To detect different gases, different pump lasers need to be used. The pump beam can be made to co-propagate (i.e., λ_1) or counter-propagate (i.e., λ_2) with the probe, as shown in Fig. 6.3. We firstly conducted methane detection experiment by using a DFB laser with wavelength λ_1 tuned to the R (3) line in the $2\nu_3$ band of methane near 1653.72 nm. The pump is wavelength modulated at 13 kHz while simultaneously being slowly scanned across the methane absorption line. The pump power is amplified using a Raman amplifier (RA) before being combined with the probe via a WDM1.

Fig. 6.4(a) presents the 2f signal for four different pump power levels measured from the output of the RA. The gas cell was filled with a gas mixture containing 1.8 ppm methane balanced in nitrogen. The system noise performance is evaluated by filling the gas cell with pure nitrogen. For a pump power of 250 mW from the RA, the average SNR for 5 measurements is ~14912 for a lock-in time constant of 1 s, yielding a NEC of ~121 ppt or a noise-equivalent-absorbance (NEA) of 4.5×10^{-11} cm^{-1}. Fig. 6.4(b) shows the time trace (inset) and the Allan-Werle plot of the system baseline noise measured with the gas cell filled with nitrogen. The optimal integration time is ∼200 s and the corresponding NEC is 15 ppt.

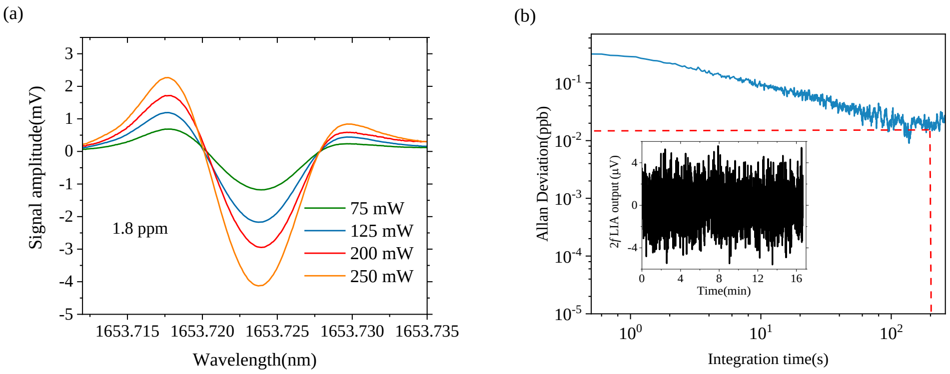

Fig. 6.4 (a) The measured 2f signal when the gas cell is filled with 1.8 ppm methane in nitrogen at atmospheric pressure. (b) The time trace (inset) and the Allan-Werle plot of the system baseline noise.

Fig. 6.5 shows the p.p. values of the measured 2f output as a function of methane concentration from 0.2 ppm to 107 ppm in nitrogen at atmospheric pressure when the RA output power is ~250 mW. An approximately linear relationship is obtained. To evaluate the OPMA factor, i.e., $G_s = k_r - k_t$, we compare the PT signal measured above with that of a single-pass HCF gas cell under the same conditions and obtain G_s ≈600.

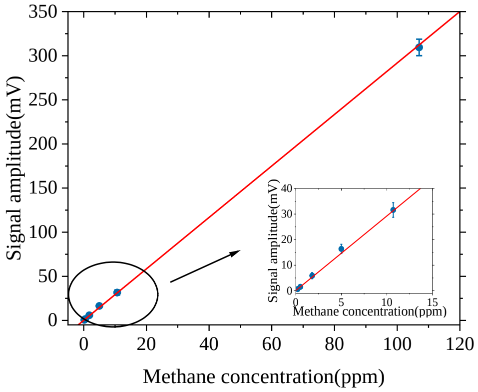

Fig. 6.5 The p.p. value of the measured 2f LIA outputs with methane concentration from 0.2 to 107 ppm and a linear fit. Error bars show 3 times the s.d. for five measurements. The inset shows the same plot for gas concentration from 0.2 ppm to 11 ppm.

The broad transmission bands of the HCF make it possible to detect multiple gas species with a single HCF gas cell, and a single probe OPMA and detection system. With the same experimental setup but an additional 761 nm pump laser in oxygen absorption band, we demonstrated simultaneous detection of methane and oxygen. Light from the DFB laser (λ_2=761 nm) is amplified to ~30 mW, by use of a SOA, before being coupled into the HCF gas cell from the opposite end, i.e., via WDM2. Fig. 6.6(a) shows the detected PT signal of methane and oxygen in the air. The two pump wavelengths (λ_1=1654 nm for methane and λ_2=761 nm for oxygen) are scanned in turn across the oxygen (0 to 75 s) and methane (75 to 150 s) absorption lines, as shown in the inset of Fig. 6.6(a). The NECs for oxygen and methane are estimated to be ~2 ppm and ~190 ppt for a lock-in time constant of 1 s, respectively. Fig. 6.6(b) displays the time trace (inset) and the Allan-Werle plot of the system baseline noise when the gas cell is filled with pure nitrogen. The NEC for oxygen is 0.56 ppm with an integration time of ~70 s.

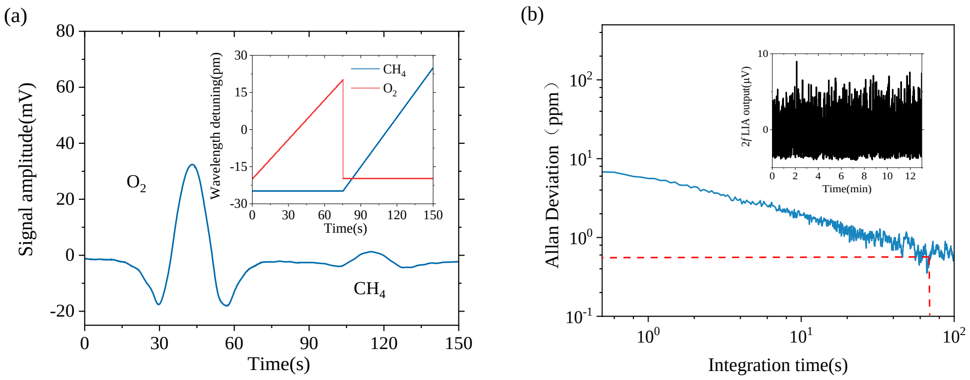

Fig. 6.6 (a) The demodulated PT signals (2f) of the methane and oxygen in the air with pump power of 250 mW at 1654 nm and 30 mW at 761 nm, respectively. The inset is the time trace of the wavelength tuning function for the 1654 nm and 761 nm lasers around the methane and oxygen absorption lines, respectively. (b) The time trace (inset) and the Allan-Werle plot of the system baseline noise for oxygen detection.

6.1.4 Acetylene detection

As illustrated in Fig. 6.7, we also conducted acetylene detection experiment with a narrow linewidth fiber laser (λ_1=1532 nm) as the pump and using the P (11) line in the $\nu_1 + \nu_3$ band of acetylene. Since the pump wavelength is within the high reflectivity band of the mirror, an additional PDH servo loop is used to lock the cavity resonance to the pump wavelength. We first fix the pump wavelength at the acetylene line center near 1531.59 nm. Then the pump beam is phase modulated at 21 MHz generating two sidebands for PDH locking. We lock the center of the HCF-FP cavity resonance to the pump wavelength by tuning the cavity length, which is achieved by using a PZT to stretch the HCF via a PDH servo. Once the cavity resonance is locked to the pump wavelength, we impose additional intensity modulation at 13 kHz on the pump beam. The pump power is amplified using an EDFA before being combined with the probe via a WDM1 and launched into the HCF FP cavity. The probe wavelength is locked to the center of another cavity resonance with a second PDH servo. The amplified phase modulation is detected by combing the reflected and transmitted probe beams to form an all-fiber MZI. The remaining part of the experimental setup is the same as in Fig. 6.3.

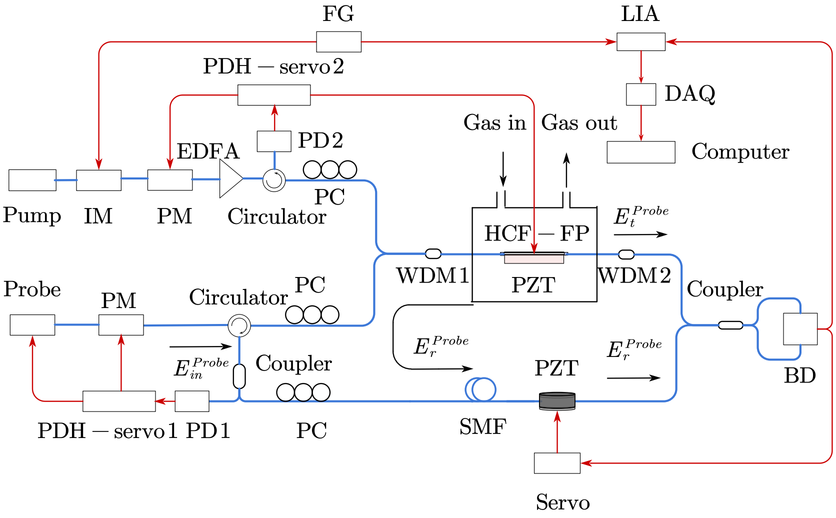

Fig. 6.7 Experimental setup for acetylene detection based on OPMA with an FP cavity. IM: intensity modulator. PM: phase modulator.

Fig. 6.8(a) shows the first harmonic component of the LIA output as the pump wavelength is tuned across the acetylene absorption line near 1531.59 nm. At each pump wavelength, the HCF cavity resonance is first locked to the pump laser, and then the probe wavelength is locked to the HCF-cavity resonance. The gas cell was filled with 0.1 ppm acetylene balanced in nitrogen. The system (baseline) noise is also evaluated by filling the gas cell with pure nitrogen. With the EDFA output power of ~100 mW, the NEC for acetylene detection is ~9 ppt for a lock-in time constant of 1 s. It is noted that there is a background signal when the pump wavelength is tuned away from the acetylene absorption line center, which is different from that observed in a previous work [7]. Such background signal is believed to be from the PT effect of the mirrors with high intracavity pump power [8, 9]. Fig. 6.8(b) shows the time trace (inset) and the Allan-Werle plot of the system baseline noise. The optimal integration time is ~113 s and the corresponding NEC is 2.7 ppt.

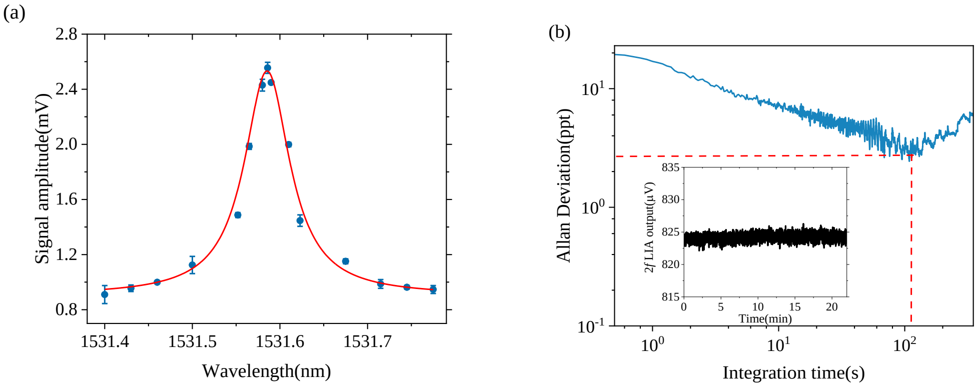

Fig. 6.8 (a) The demodulated PT signal (1f) as the pump wavelength is tuned across the acetylene absorption line near 1531.59 nm. Error bars show 3 times the s.d. from 5 measurements. (b) The time trace (inset) and the Allan-Werle plot of the system baseline noise for acetylene detection.

6.1.5 Discussion

Table 6.1 provides a comparative summary of the performance of various gas sensors based on laser spectroscopy. Considering the different gas species and gas cell lengths (L) used for different experiments, we use $NEA \cdot L$ to evaluate gas detection performance, which is independent of absorption strength and the gas cell length. The $NEA \cdot L$ of the OPMA with an

FP cavity is two orders of magnitude smaller than most of the existing laser spectroscopic gas sensors and is comparable to one of the most sensitive techniques, i.e., noise-immune cavity-enhanced optical heterodyne molecular spectroscopy (NICE-OHMS), which uses open-path optical cavities with a much higher finesse. The all-fiber OPMA-PTI system is much more flexible to construct and has a compact size and lower cost. The other attractive feature of the OPMA technique is its capability for multi-gas detection: the same detection system may be used to detect different gas species by simply changing a pump laser. Simultaneous detection of multiple gas species is also possible by coupling multiple pump wavelengths into the same HCF gas cell.

Table 6.1 Performance comparison of advanced gas sensors based on laser spectroscopy.

Gas type	Technology	λ_{probe}	Sensing element length (m)	Finesse	Integration time (s)	$NEA \cdot L$
C_2H_2	MPD-PTS [10]	1532	4.67	Single-pass	100	7.5×10^{-9}
C_2H_2	PTS [11]	1530	10	Single-pass	10	2.3×10^{-6}
NO	TDLAS [12]	5263	210	Single-pass	30	3.2×10^{-6}
C_2H_2	NICE-OHMS [13]	1532	0.39	55000	170	1.8×10^{-12}
CO	CMDS [14]	1560	0.74	41000	10	3.7×10^{-9}
CH_4	OPMA-PTS (This work)	1653	0.10	700	200	5.6×10^{-11}

C_2H_2	OPMA-PTS (This work)	1532	0.10	700	113	3.1×10^{-11}

CMDS: cavity mode-dispersion spectroscopy.

Further enhancement of detection sensitivity is possible by optimizing launching of the pump beam launch configuration into the HCF gas cell to enhance the pump power level in the HCF, and by using an HCF cavity with a higher finesse and a longer length. An HCF FP cavity with finesse up to 3000 has been experimentally achieved with a 36-cm-long HCF [15], which would enable gas sensors with detection limit down to part-per-quadrillion (ppq) level. The OPMA with an HCF resonating cavity holds great potential for enhancing the sensitivity of various phase or dispersion modulation-based sensors.

6.2 OPMA with a DMI

6.2.1 Principle of OPMA with a DMI

The principle of the OPMA with a DMI may be explained with the vector sum operation, as depicted in Fig. 6.9 [16]. The DMI comprises two sections of SMFs and one dual-mode HCF which excites LP_{01} and LP_{11} modes simultaneously within the hollow core. The two modes combine at the output SMF, and the combined electric field may be expressed as:

$$E_{out}\, exp(\omega t - j\psi) = \tag{6.6}$$

$$E_{01}exp(\omega t - j\phi_{01}) + E_{11}exp(\omega t - j\phi_{11})$$

where E_{out} and ψ are the amplitude and phase of the combined optical field, E_{01} and E_{11} are the amplitudes while ϕ_{01} and ϕ_{11} are the phases of the LP_{01} and LP_{11} modes, respectively, and ω is the angular optical frequency.

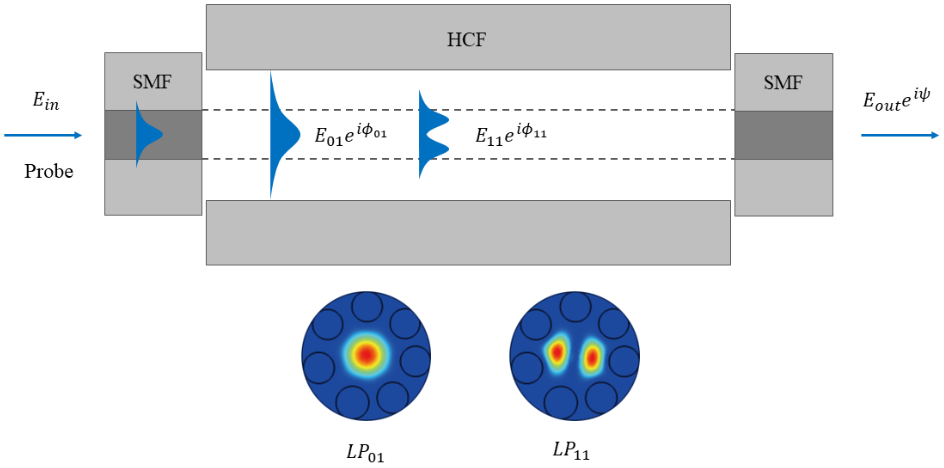

Fig. 6.9 Diagram of the excited LP_{01} and LP_{11} modes within the dual-mode HCF, and the two modes are combined at the output of the HCF.

The resultant phase ψ depends on the relative strength ($\hat{E} = E_{01}/E_{11}$) of two modes and the phase difference ($\varDelta\phi = \phi_{01} - \phi_{11}$) between the two optical modes, which is given by:

$$\psi = \phi_{11} + arctan\left(\frac{\hat{E}\sin(\varDelta\phi)}{1 + \hat{E}\cos(\varDelta\phi)}\right) \tag{6.7}$$

When a pump beam, which undergoes modulation, propagates through the HCF and gets absorbed by trace molecules within the gas medium, the absorption leads to the generation of heat, causing perturbations in the RI distribution of the gas. With the assumption of weak absorption, the PT-induced phase modulation can be expressed as Eq. (3.8). Hence, as illustrated in Fig. 6.10(a), with destructive interference condition, and $\hat{E}$ close to 1, a small baseline phase modulation in $\Delta\phi$, i.e., the PT phase modulation (ϕ_{PT}), will be transformed into a large phase modulation ($\Delta\psi$) at the output of the DMI, resulting in OPMA:

$$\Delta\psi = k\phi_{PT} \tag{6.8}$$

where k is the amplification factor defined by the slope of $d\psi/d\Delta\phi$ and can be determined by substituting the destructive interference condition ($\Delta\phi = \pi$) to Eq. (6.7):

$$k = \left|\frac{d\psi}{d\Delta\phi}\right| = \left|\frac{\hat{E}\,cos(\Delta\phi) + \hat{E}^2}{\hat{E}^2 + 2\hat{E}\,cos(\Delta\phi) + 1}\right| \approx \frac{\hat{E}}{1-\hat{E}} \tag{6.9}$$

Fig. 6.10(b) presents plots of illustrating the relationship between ψ and $\Delta\phi$ for various values of $\hat{E}$. In the calculation, since the value of ϕ_{11} will not change the derivative ($d\psi/d\Delta\phi$), which will not affect the amplitude of the amplified phase modulation, ϕ_{11} was set to 0 without loss of generality. As can be seen, the phase of the combined optical field experiences a dramatic change near $\Delta\phi = \pi$ where the slope increases as the relative strength $\hat{E}$ approaches unity.

Fig. 6.10(c), demonstrates the relationship between the amplitude ratio of the two probe modes and the amplification factor, denoted as k. As the amplitude ratio increases from 0.5 to 0.99, the amplification factor k rises from 1 to approximately 100. This observation suggests that significant amplification in optical phase modulation, up to a hundred-fold, can be achieved using the OPMA technique. However, it is worth noting that as the amplification magnitude increases, the linear range of the amplification decreases.

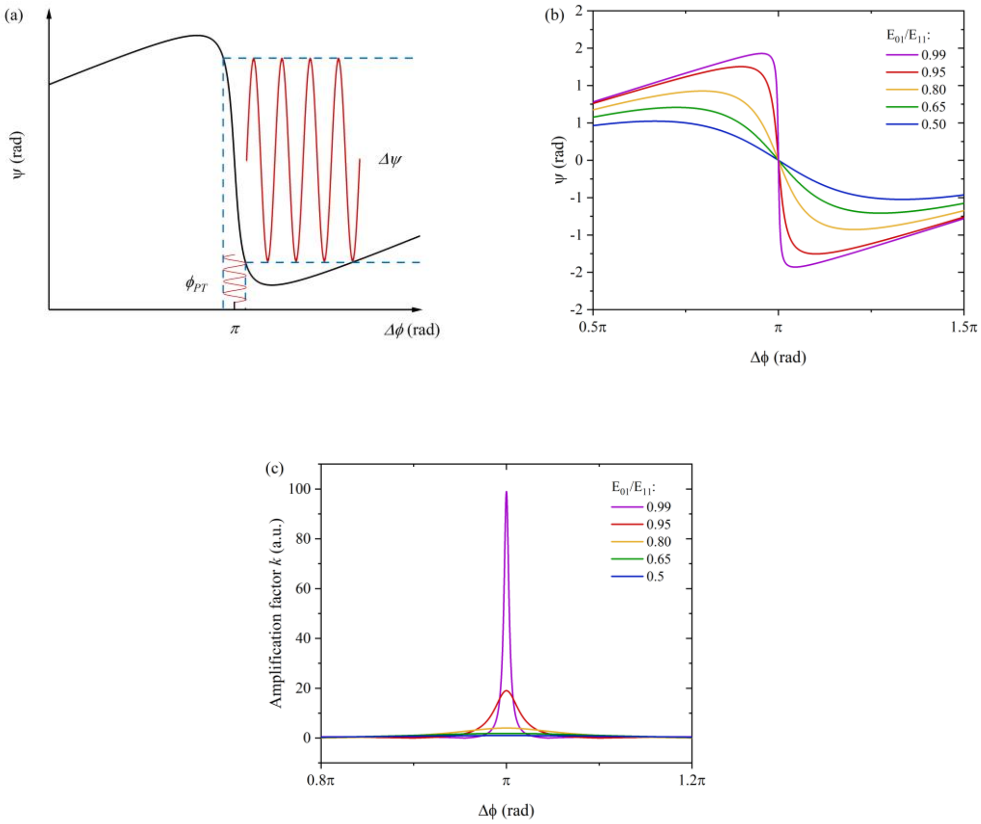

Fig. 6.10 (a) Illustration of the OPMA near $\Delta\phi = \pi$. (b) Plots of ψ as a function of $\Delta\phi$ for various values of $\hat{E}$. (c) The amplification factor k as a function of $\Delta\phi$ for various values of $\hat{E}$.

6.2.2 Construction and characteristics of the gas cell

The gas cell utilized is fabricated using a 50-cm-long HC-ARF characterized by a core diameter of 28 μm, which is designed to support the LP_{01} and LP_{11} modes with low transmission loss from 1000 nm to 2000 nm [17]. The HC-ARF is sandwiched between a SMF and a thermally expanded core fiber (TECF) via mechanical connection with ceramic sleeves and ferrules. The TECF is 8° angle-cleaved to avoid the formation of an FPI and its mode field diameter is 28 μm. Simultaneous excitation of the LP_{01} and LP_{11} modes is accomplished by introducing lateral offset, i.e., the lateral positions of the input SMF and output TECF with the HCF, respectively, which are deliberately controlled to adjust the ratio of the energy of the two modes to ensure good fringe contrast of the dual-mode interference. The ratio of the energy of these two modes can be further adjusted by the PC. The fringe contrast can be expressed as [18]:

$$\text{Fringe contrast} = 10\log_{10}\frac{1+\hat{E}^2+2\hat{E}}{1+\hat{E}^2-2\hat{E}} \tag{6.10}$$

Hence, the relative strength $\hat{E}$ along with the amplification factor k can be determined by the fringe contrast of the DMI which can be easily measured using an optical spectrum analyzer (OSA). Fig. 6.11 depicts the transmission spectrum of the DMI. As presented in Fig. 6.11(a), the FSR of the interference is ~4.6 nm determined through measurements conducted employing a BLS and an OSA. Fig. 6.11(b) presents a more refined measurement of the interference fringe near 1550 nm with a narrow linewidth tunable laser. The fringe contrast is ~31 dB, corresponding to a theoretical OPMA factor of 17.

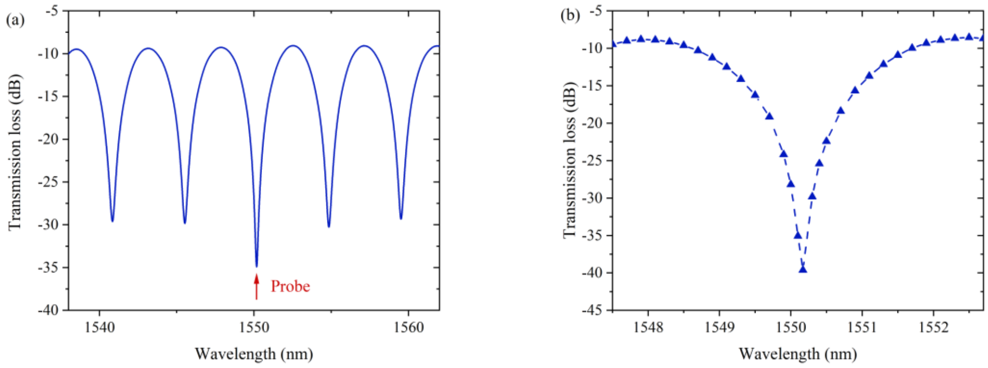

Fig. 6.11 The transmission spectrum of the HCF DMI. (a) Mode interference spectrum measured with an OSA. (b) Mode interference spectrum measured with a tunable laser.

6.2.3 Carbon dioxide detection

The experimental configuration is illustrated in Fig. 6.12. A pump beam from a DFB laser with a center wavelength at 2004 nm is amplified by a thulium-doped fiber amplifier (TDFA) to about 178 mW and coupled into the HC-ARF via a WDM. The pump wavelength is sinusoidally modulated at 11 kHz and slowly scanned across the R (16) line in the $2\nu_1 + \nu_3$ band of carbon dioxide absorption line near 2004.02 nm. The probe beam from an ECDL with the center wavelength of 1550.2 nm is divided into two beams by a fiber coupler. One beam with 99% power is coupled into the HC-ARF gas cell, which is positioned in the sensing arm of an optical fiber MZI. The PT-induced optical phase modulation is amplified by operating the probe wavelength at destructive interference of the DMI, which is detected by the MZI. The other beam is coupled into the reference arm to keep the MZI at quadrature via a PZT and an active servo loop. To achieve optimal fringe contrast of the MZI, the light intensity of the MZI is reduced via the attenuator to ensure the optical power of two arms of the MZI almost equal. The second harmonic component from the PD1 is demodulated as the PT signal by a LIA.

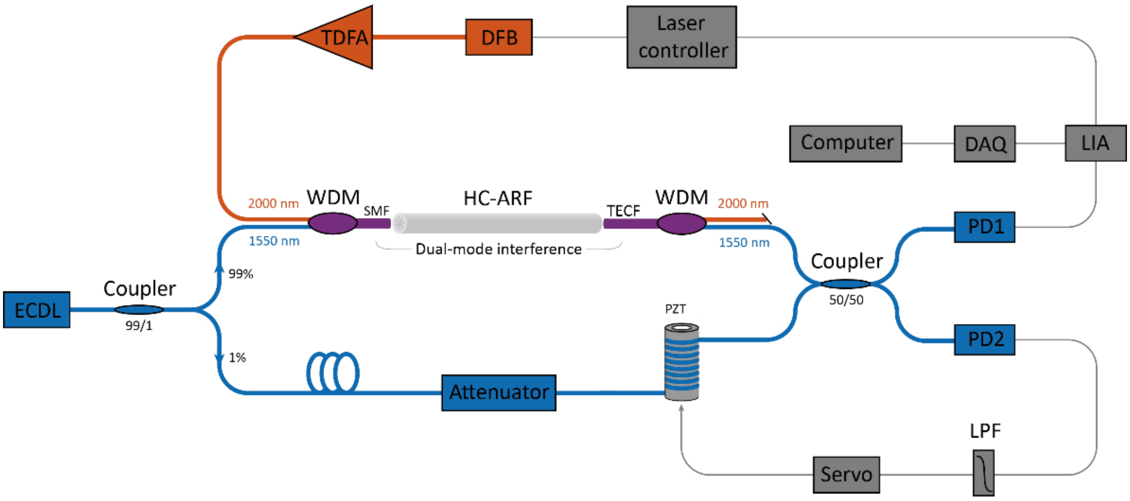

Fig. 6.12 Experimental setup for carbon dioxide detection based on OPMA with an HCF DMI.

Experiments were conducted with the HCF DMI filled with standard gas of 600 ppm carbon dioxide balanced in nitrogen. The gas was introduced into the hollow core of the fiber at a pressure of approximately 1.4 bar using a pressure controller located at the input joint, while the output joint remained open to the surrounding atmosphere. The flow rate of the gas was carefully regulated with the aid of a flow meter attached to the gas cylinder. Fig. 6.13(a) shows the detected 2*f* signal from the LIA when the pump wavelength is tuned across the carbon dioxide absorption line near 2004.02 nm for different pump power levels delivered into the HCF. The system noise performance is evaluated by filling the gas cell with pure nitrogen. The $2f$ PT signal is linearly proportional to the pump power while the s.d. of the detection noise remains unchanged, as shown in Fig. 6.13(b). With the input SMF carrying a pump power of approximately 178 mW, the SNR is measured to be 34148 for a lock-in time constant of 1 s. This measurement corresponds to a NEC of approximately 18 ppb for an SNR value of unity.

The stability of the system was assessed by employing the Allan deviation analysis on the background noise. To conduct this analysis, the pump wavelength was tuned to 2004.02 nm, and the gas cell was filled with pure nitrogen at a pressure of approximately 1.4 bar at the input joint. The results of the Allan deviation analysis, performed on the noise data acquired over a duration of 3 hours, are depicted in Fig. 6.13(c). The results are noisy near and beyond the averaging time of 1000 s, so we roughly choose 1000 s as the averaging time. The corresponding NEC for the SNR of unity is estimated to be 1 ppb. Furthermore, the NEC for an averaging time of 100 s is 6 ppb.

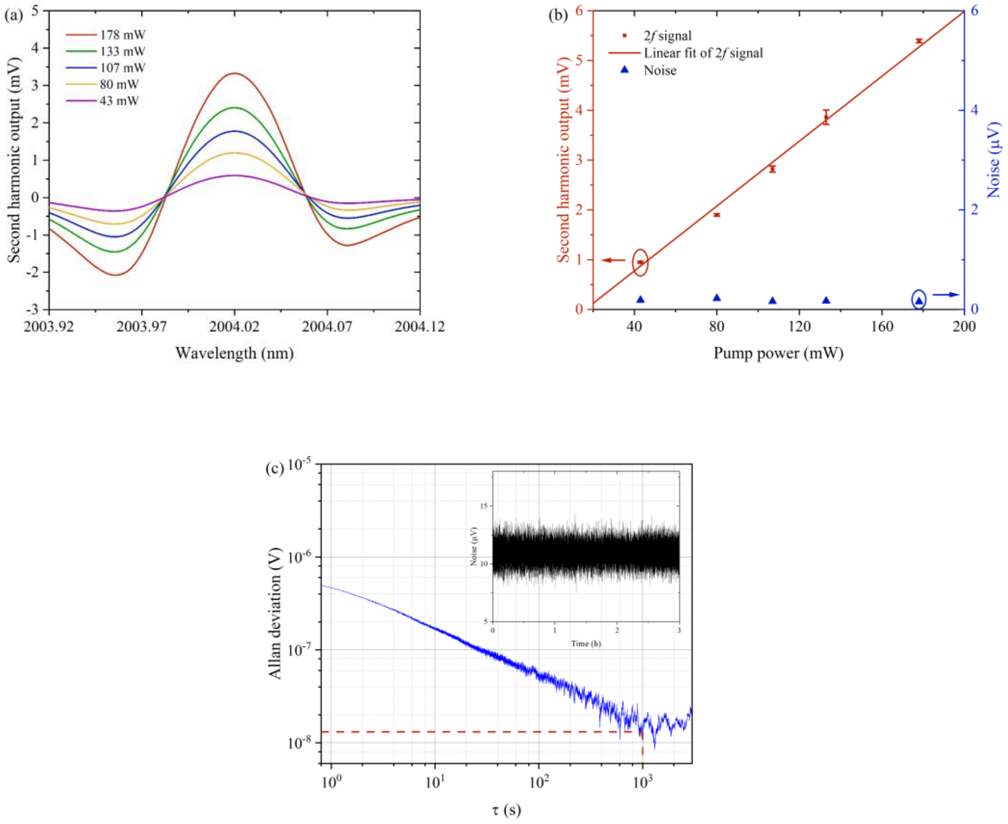

Fig. 6.13 (a) The detected 2f signal as the pump wavelength is tuned across the carbon dioxide line with different power levels. (b) The p.p. value of the 2f signal and the s.d. of the detection noise as functions of the pump power level. Error bars, representing the s.d. obtained from five measurements, are scaled up by a factor of five. (c) The Allan-Werle plot based on the noise data over a period of 3 hours, which is shown in the inset.

The sensor system's dynamic range is evaluated by introducing varying concentrations of carbon dioxide into the HCF. Fig. 6.14(a) shows the 2*f* signals for 10 ppm, 100 ppm, 600 ppm, 3000 ppm, 1% and 5% carbon dioxide balanced in nitrogen, whereas Fig. 6.14(b) specifically presents the 2*f* signals for 10 ppm carbon dioxide to demonstrate the ability to perform low concentration detection. Fig. 6.14(c) presents the p.p. values of the 2*f* signal, which are plotted as a function of the carbon dioxide concentration spanning from 10 ppm to 5%. The 2*f* signal exhibits an approximately linear escalation corresponding to the gas concentration. Upon evaluation, the dynamic range is evaluated to be ~5×10^7.

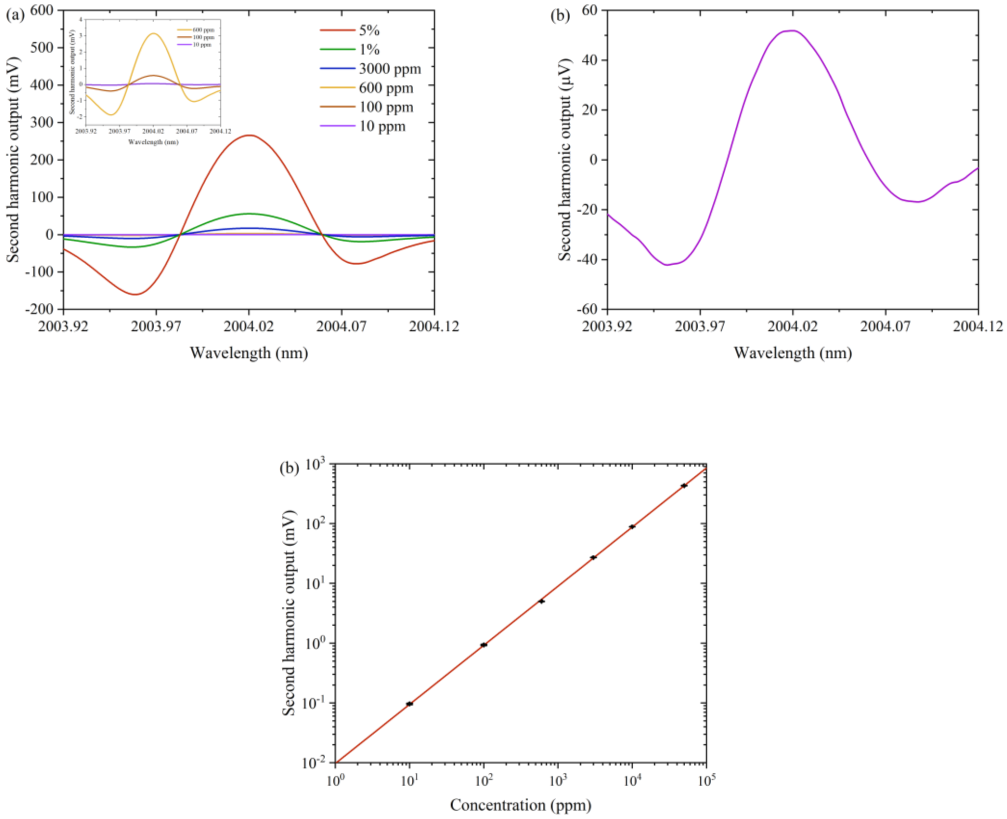

Fig. 6.14 (a) The detected 2f signal when pump laser is tuned across the carbon dioxide line for 10 ppm, 100 ppm, 600 ppm, 3000 ppm, 1% and 5% carbon dioxide concentration. The 2f signal for 10, 100 and 600 ppm carbon dioxide are scaled up in the inset for clary reason. (b) The detected 2f signal for 10 ppm carbon dioxide. (c) The p.p. value of the 2f signal as a function

of gas concentration. Error bars represent the s.d. derived from a set of five independent measurements.

6.2.4 Evaluation of OPMA factor

To determine the OPMA factor, we compare the 2*f* PT phase modulation with and without OPMA using the same DMI. With OPMA, the DMI is operated with the probe wavelength at the destructive interference and placed in the sensing arm of an MZI. The PT phase modulation is measured by the MZI. However, without OPMA, the PT phase modulation is directly measured by the DMI with the probe wavelength at the quadrature. We keep other experiment conditions identical. As shown in Fig. 6.15(a), the OPMA factor is estimated to be 18 when the p.p. values of the detected 2*f* signals with and without OPMA are 5.4 mV and 0.3 mV, respectively. The experimentally measured OPMA factor is consistent with the theoretical prediction. The s.d. of the noise for both schemes are ~0.1 μV, indicating that the OPMA does not increase the system noise level while amplifying the signal and hence improves the SNR.

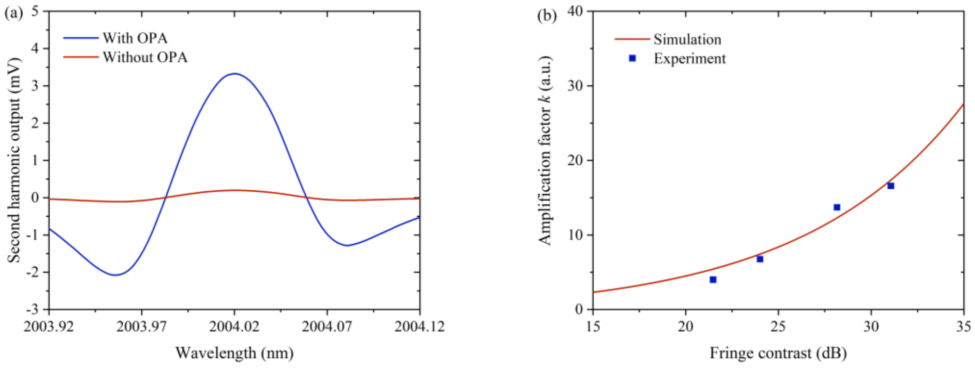

Fig. 6.15 (a) The detected 2f signal with and without OPMA. (b) The simulation and experimental results of the amplification factor as a function of the fringe contrast.

Further investigations were conducted to exhibit the potential for modulating the phase amplification factor through straightforward alterations of the fringe contrast of the interferometer. According to Fig. 6.11(a), there are several dips corresponding to the destructive interferences from 1540 to 1560 nm. We tuned the probe wavelength to the appropriate destructive interference and adjusted the fringe contrast with the PC, resulting in a DMI with different contrasts. At each setting of the contrast, we conducted the $2f$ signal detection with and without OPMA by tuning the probe wavelength to the corresponding operating points of the DMI. Fig. 6.15(b) illustrates the comparison between the experimental amplification factors and the theoretical counterparts, corresponding to distinct contrast setting. The observed pattern of the measured phase amplification factor's progression with varying contrast is in substantial agreement with the theoretical trajectory. These experimental findings corroborate the proposition that the amplification factor of the OPMA can be controlled through simple modifications of the fringe contrast. Notably, an increase in fringe contrast corresponds to an enhancement in the amplification factor.

6.2.5 Precision measurement of carbon dioxide isotope ratio

To exemplify its pragmatic implications, we demonstrated sensitive carbon dioxide isotope ratio detection, which can be applied for the diagnosis of *H. Pylori* infection. *H. Pylori* infection, a pathogenic condition linked to ailments such as gastric ulcers and gastric cancer, can be diagnosed by a non-invasive urea breath test (UBT) using stable ^{13}C isotope [19]. Delta over baseline (DOB) value is used to determine the infection and assess the severity of the disease. The DOB value is defined as:

$$DOB = \left({}^{13}R_{sample}/{}^{13}R_{reference} - 1\right) \tag{6.11}$$

where ${}^{13}R_{sample}$ and ${}^{13}R_{reference}$ refer to the $^{13}CO_2/^{12}CO_2$ before and after ^{13}C-labeled urea administration, respectively [20]. Hence, sensitive detection of the CO_2 isotope ratio is of prime importance.

In CO_2 isotope ratio measurement, it is desirable for $^{13}CO_2$ and $^{12}CO_2$ have comparable absorption line strengths and temperature coefficients at proximity frequency. Fig. 6.16(a) shows the calculated absorption lines of 3.56% $^{12}CO_2$, 400 ppm $^{13}CO_2$ and 1% H_2O at 273 K and 1 atm. The absorption coefficients of 3.56% $^{12}CO_2$ R (68) at 1994.52 nm and 400 ppm $^{13}CO_2$ R (38) at 1993.48 nm are 6.4×10^{-6} and 7.6×10^{-6} cm^{-1}, respectively. The small absorption coefficients make highly sensitive detection a requirement.

The CO_2 isotope ratio measurement was conducted with standard gas of 5% carbon dioxide balanced in nitrogen. A DFB laser with center wavelength at 1993 nm is used as pump source, which is amplified by the TDFA. Other experiment conditions are identical to the experiments we mentioned before. When the pump power in the input SMF is ~178 mW, the detected $2f$ signal of 5% CO_2 in the laboratory conditions is shown in Fig. 6.16(b). The absorption lines of $^{12}CO_2$ R (68) and $^{13}CO_2$ R (38) are well defined without the interference from the absorption of H_2O.

Fig. 6.16(c) shows the p.p. values of the selected line pair over a period of 1 hour, where the blue dots are $^{12}CO_2$ R (68) and the red dots are $^{13}CO_2$ R (38). The average of the $^{13}CO_2/^{12}CO_2$ as $^{13}R_{reference}$ is used to calculate the DOB value, as shown by the black dots in Fig. 6.16(c) [21]. We performed Allan variation analysis on the DOB data shown in Fig. 6.16(d). The DOB precision with ~170 averages could reach 1‰, which makes it an economical candidate for ^{13}C-labeled UBT with high accuracy.

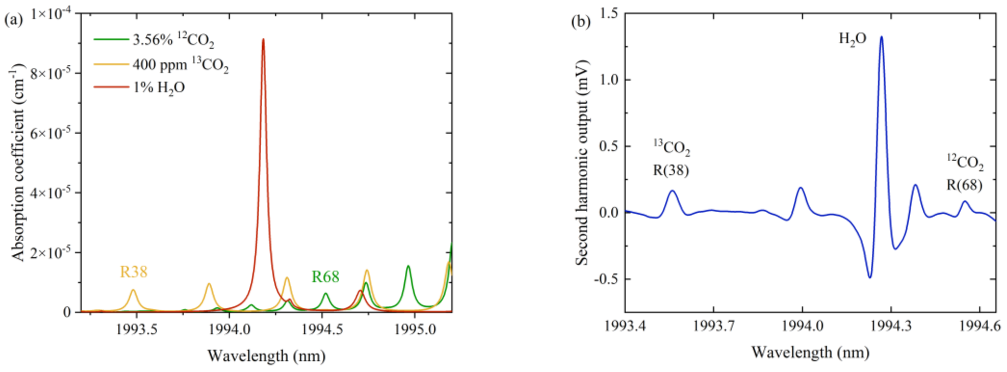

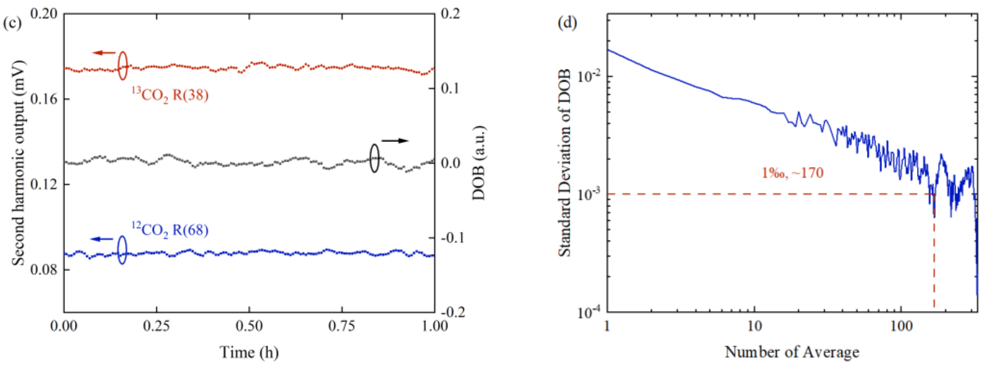

Fig. 6.16 (a) The calculated absorption spectrum of 3.56% $^{12}CO_2$*, 400 ppm* $^{13}CO_2$ *and 1%* H_2O *at 273 K and 1 atm according to HITRAN2016 database. (b) The detected 2f signal of 5%* CO_2 *in the laboratory conditions. (c) The p.p. value of the 2f signal of* $^{12}CO_2$ *R (68) and* $^{13}CO_2$ *R (38) and DOB value over a period of 1 hour. (d) S.d. of DOB with different numbers of average.*

6.2.6 Noise analysis

The performance improvement of the PT gas detection using OPMA has been demonstrated theoretically and experimentally. To understand the limitation of the technique, we examine the noise contributions by measuring the spectrum of the electronic noise of PD, the probe laser intensity noise, the PTI noise with and without OPMA. From the experiments in the previous section, the received optical power at the PD is ~2 μW and hence we ensure that the received optical power and other conditions are consistent when measuring each of the noise components. As shown in Fig. 6.17, the PTI noise with OPMA is very close to the PTI noise without OPMA, indicating that the OPMA does not increase the system noise level. And the main noise source for both cases is the electronic noise of PD. It is worth noting that in the low frequency band (<10 kHz), the PTI noise with OPMA is mainly affected by the PZT, which is used to stabilize the MZI.

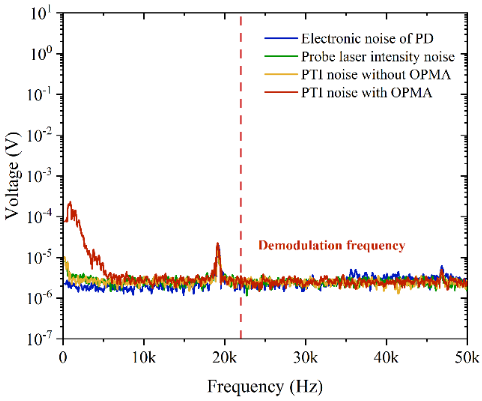

Fig. 6.17 The spectrum of the electronic noise of PD, the probe laser intensity noise, the PTI noise with and without OPMA.

To verify the experimental results, we also perform the theoretical analysis of the system noise, utilizing the detailed discussion provided in Section 3.3. The noise present in the PTI system exhibits intricate characteristics that are contingent upon the particular configuration and arrangement of the interferometers.

Laser phase noise could be transferred into interferometric output fluctuation depending on the OPD of the MZI. By scanning the wavelength of the ECDL and observing the interference fringe pattern on the oscilloscope, we find that the OPD of the dual-beam MZI can be minimized by using a motorized optical fiber delay line compared to that of the DMI. The time delay between the two modes in the HCF can be expressed as:

$$\tau_d = \frac{\Delta nL}{c} \tag{6.12}$$

where $\Delta n(= n_{01} - n_{11})$ is the effective RI difference between LP_{01} and LP_{11} modes, which is 9×10^{-4}, and c is the speed of light, giving τ_d of 1.5×10^{-12} s and the optical phase difference of 450 μm for a 50-cm-long HCF. The coherence time of the probe laser can be expressed as:

$$\tau_c = \frac{1}{\pi\Delta\nu} \tag{6.13}$$

where $\Delta\nu$ is the laser linewidth. For our experiments, the linewidth of the probe laser is ~100 kHz, giving τ_c of 3.2×10^{-6} s and hence $\tau_d \ll \tau_c$. For this case with OPMA and at the quadrature operation point of the MZI, the RMS of the MZI output fluctuation induced by the laser phase noise may be expressed as [22]:

$$i_{phase} = R_{PD}Pk\frac{2}{\sqrt{\tau_c}}|\tau_d|e^{|\tau_d|/\tau_c}\sqrt{\Delta f} \tag{6.14}$$

The analysis methods for intensity noise, electronic noise, and shot noise are presented in detail in Section 3.3. The total RMS deviation of the output noise can be rewritten as Eq. (3.28). The sensor performance is analyzed by theoretical calculation of the system noise and its contributions which is depicted in Fig. 6.18 when the system is operated with OPMA and without OPMA, respectively. For both cases, the electronic noise dominates the system noise when the probe power is lower than 2 μW. As the probe power is increased, the contribution of shot noise surpasses electronic noise and dominates the system noise. Furtherly increasing the probe power, probe intensity noise starts being the major contribution to the system noise. For system operated with OPMA, even though the laser phase noise is amplified by the OPMA, its contribution remains relatively small compared with other noise contributions. Hence, the system performance is not limited by the probe phase noise. Noteworthy, the large amplification factor arising from the pronounced fringe contrast would lead to a low probe power at the destructive interference, thereby preventing the system from reaching the detection limit.

For our experiment with ~2 μW probe power reached PD, electronic noise and shot noise contribute comparably to the system noise. Improvement of the detection SNR is possible by using probe laser with higher power ensuring shot noise dominants the system noise. This is attributed to the linear relationship between the signal and probe power, whereas shot noise follows a square root dependency with respect to the probe power.

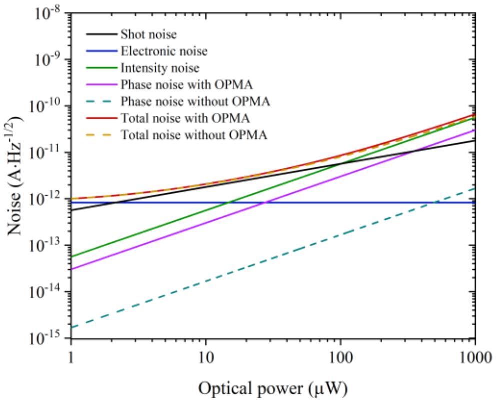

Fig 6.18 The simulated results of the noise as a function of the optical power received by the PD.

6.3 Conclusion

In conclusion, we have shown that the use of OPMA can enhance the sensitivity of PTI for gas detection. Two implementations are demonstrated.

Firstly, we demonstrate OPMA by locking the probe wavelength to the center of the resonance of a high-finesse HCF cavity. By locking the wavelength of a 1550 nm probe laser to the resonance of a 10-cm-long HCF FP cavity with a finesse of ~700, OPMA of more than two orders of magnitude is achieved, which enables ultra-sensitive gas detection with large dynamic range. With 1654 nm, 1532 nm, and 761 nm pump lasers, we demonstrate detection of methane, acetylene, and oxygen with NEC of 15 ppt, 2.7 ppt, and 0.56 ppm, respectively. Further improvement in NEC is possible by use of a higher finesse cavity with a longer length of HCF.

Extension of the technique to other gases, other types of phase or dispersion modulation-based sensors, and other optical resonating cavities is straightforward.

Secondly, we demonstrate OPMA of a DMI operating at destructive interference. With OPMA, detection of carbon dioxide with NEC of 1 ppb has been achieved with a 50-cm-long HC-ARF and 1000-s averaging time under ambient conditions. The dynamic range is over 7 orders of magnitude. We have confirmed both theoretically and experimentally that phase noise in the DMI is not the main noise source of our system and hence the OPMA with the DMI does not significantly increase the system noise level. Comparing with the gas detection without OPMA, the PT signal is enhanced by a factor of ~20 while the system noise remains the same, meaning that the SNR of the PTI system is enhanced by the same factor. Based on the noise analysis of the OPMA, the detection sensitivity could be significantly improved with higher power of the probe laser. The utilization of an OPMA integrated with an optical fiber DMI presents a viable approach to enhance the sensitivity of sensors based on phase modulation. This configuration offers a compact and straightforward design, thereby facilitating ease of implementation and improved sensor performance.

Reference of Chapter 6

1. G. Zhao, D. M. Bailey, A. J. Fleisher, J. T. Hodges, and K. K. Lehmann, "Doppler-free two-photon cavity ring-down spectroscopy of a nitrous oxide (N 2 O) vibrational overtone transition," Physical Review A **101**, 062509 (2020).

2. J. Van Helden, N. Lang, U. Macherius, H. Zimmermann, and J. Röpcke, "Sensitive trace gas detection with cavity enhanced absorption spectroscopy using a continuous wave external-cavity quantum cascade laser," Applied Physics Letters **103**, 131114 (2013).

3. J. Langridge, T. Laurila, R. Watt, R. Jones, C. Kaminski, and J. Hult, "Cavity enhanced absorption spectroscopy of multiple trace gas species using a supercontinuum radiation source," Optics Express **16**, 10178-10188 (2008).

4. B. J. Slagmolen, M. B. Gray, K. G. Baigent, and D. E. McClelland, "Phase-sensitive reflection technique for characterization of a Fabry–Perot interferometer," Applied Optics **39**, 3638-3643 (2000).

5. P. Patimisco, S. Borri, I. Galli, D. Mazzotti, G. Giusfredi, N. Akikusa, M. Yamanishi, G. Scamarcio, P. De Natale, and V. Spagnolo, "High finesse optical cavity coupled with a quartz-enhanced photoacoustic spectroscopic sensor," Analyst **140**, 736-743 (2015).

6. R. W. Drever, J. L. Hall, F. V. Kowalski, J. Hough, G. Ford, A. Munley, and H. Ward, "Laser phase and frequency stabilization using an optical resonator," Applied Physics B **31**, 97-105 (1983).

7. C. Yao, S. Gao, Y. Wang, P. Wang, W. Jin, and W. Ren, "MIR-pump NIR-probe fiber-optic photothermal spectroscopy with background-free first harmonic detection," IEEE Sensors Journal **20**, 12709-12715 (2020).

8. Y. Tan, W. Jin, F. Yang, Y. Jiang, and H. L. Ho, "Cavity-enhanced photothermal gas detection with a hollow fiber Fabry-Perot absorption cell," Journal of Lightwave Technology **37**, 4222-4228 (2019).

9. K. An, B. Sones, C. Fang-Yen, R. Dasari, and M. Feld, "Optical bistability induced by mirror absorption: measurement of absorption coefficients at the sub-ppm level," Optics letters **22**, 1433-1435 (1997).

10. P. Zhao, Y. Zhao, H. Bao, H. L. Ho, W. Jin, S. Fan, S. Gao, Y. Wang, and P. Wang, "Mode-phase-difference photothermal spectroscopy for gas detection with an anti-resonant hollow-core optical fiber," Nature communications **11**, 847 (2020).

11. W. Jin, Y. Cao, F. Yang, and H. L. Ho, "Ultra-sensitive all-fibre photothermal spectroscopy with large dynamic range," Nature communications **6**, 6767 (2015).

12. D. D. Nelson, J. B. McManus, S. C. Herndon, J. H. Shorter, M. S. Zahniser, S. Blaser, L. Hvozdara, A. Muller, M. Giovannini, and J. Faist, "Characterization of a near-room-temperature, continuous-wave quantum cascade laser for long-term, unattended monitoring of nitric oxide in the atmosphere," Optics letters **31**, 2012-2014 (2006).

13. G. Zhao, T. Hausmaninger, W. Ma, and O. Axner, "Differential noise-immune cavity-enhanced optical heterodyne molecular spectroscopy for improvement of the detection sensitivity by reduction of drifts from background signals," Optics Express **25**, 29454-29471 (2017).

14. A. Cygan, P. Wcisło, S. Wójtewicz, G. Kowzan, M. Zaborowski, D. Charczun, K. Bielska, R. S. Trawiński, R. Ciuryło, and P. Masłowski, "High-accuracy and wide dynamic range frequency-based dispersion spectroscopy in an optical cavity," Optics Express **27**, 21810-21821 (2019).

15. M. Ding, E. R. N. Fokoua, T. D. Bradley, F. Poletti, D. J. Richardson, and R. Slavík, "Hollow core fiber Fabry-Perot interferometers with finesse over 3000," in *CLEO: Science and Innovations*(Optica Publishing Group2020), p. SF2P. 2.

16. M. B. Ayun, A. Schwarzbaum, S. Rosenberg, M. Pinchas, and S. Sternklar, "Photonic radio frequency phase-shift amplification by radio frequency interferometry," Opt Lett **40**, 4863-4866 (2015).

17. S. L. Jiang, W. Jin, F. F. Chen, S. F. Gao, and H. H. Lut, "Carbon Dioxide Detection with High Sensitivity Based on Photo-Thermal Spectroscopy in Hollow-Core Optical Fiber," Acta Opt Sin **41** (2021).

18. M. Born, and E. Wolf, *Principles of optics: electromagnetic theory of propagation, interference and diffraction of light* (Elsevier, 2013).

19. B. Braden, B. Lembcke, W. Kuker, and W. Caspary, "13C-breath tests: current state of the art and future directions," Digestive and Liver Disease **39**, 795-805 (2007).

20. L. M. Best, Y. Takwoingi, S. Siddique, A. Selladurai, A. Gandhi, B. Low, M. Yaghoobi, and K. S. Gurusamy, "Non‐invasive diagnostic tests for Helicobacter pylori infection," Cochrane Database of Systematic Reviews (2018).

21. Z. Wang, Q. Wang, J. Y.-L. Ching, J. C.-Y. Wu, G. Zhang, and W. Ren, "A portable low-power QEPAS-based CO2 isotope sensor using a fiber-coupled interband cascade laser," Sensors and Actuators B: Chemical **246**, 710-715 (2017).

22. M. R. Salehi, and B. Cabon, "Theoretical and Experimental Analysis of Influence of Phase-to-Intensity Noise Conversion in Interferometric Systems," Journal of Lightwave Technology **22**, 1510-1518 (2004).

Chapter 7 Conclusions and future works

7.1 Conclusions

In this thesis, we have studied the techniques to enhance the performance of fiber optic PTI with HCFs for gas sensing. The contributions can be succinctly summarized as follows:

1. For gases such as oxygen with weak optical absorption in the NIR domain, we propose a visible-pump and NIR-probe scheme. This configuration enables efficient light-gas interaction within the visible spectrum, simultaneously offering a cost-effective solution for the detection of oxygen by employing a NIR probe interferometer. Comprehensive modelling for PT phase modulation in HCF by considering thermal relaxation of oxygen and thermal conduction has been carried out. The optimized configurations with reflective mirrors are employed to enhance the sensitivity of oxygen detection. To develop practical PTI gas sensors, a compact high-finesse FP cavity with a short HCF is proposed. The detection limit of oxygen down to 6 ppm and a long-term stability of <1.6% over 3 hours has been achieved with a 1-cm-long HCF.
2. The parasitic interferences due to reflections and backward scatterings are investigated with PTI systems powered by broadband and narrow-linewidth probe sources. To suppress parasitic interference, a fiber optic LC-PTI for gas detection with ultra-high

precision and stability is proposed, employing a BLS with a short coherence length. With a 10-cm-long HCF, acetylene detection with NEC of 0.7 ppb and measurement precision of 0.025% is achieved. The stability of the detection over a period of 3 hours is ±0.038%, ten times better than the state-of-the-art PTS. The measurement of the $^{13}C/^{12}C$ isotope ratio of acetylene with measurement precision of ~0.01% is demonstrated, highlighting the potential of LC-PTI as an alternative to mass spectrometers in a compact form.

3. To further improve the gas detection sensitivity, an OPMA is firstly demonstrated by locking the probe wavelength to the resonance of an HCF FP cavity. Employing different pump lasers, we demonstrate the detection of methane, acetylene, and oxygen, achieving a NEC of 15 ppt, 2.7 ppt and 0.56 ppm, respectively. To avoid the complexity due to the precise wavelength locking, we further elucidate the exploration of OPMA by operating a fiber optic DMI at destructive interference. With a 50-cm-long dual-mode HCF, amplification of PT phase modulation by a factor of nearly 20 is achieved, which enables carbon dioxide detection down to 1 ppb with a dynamic range of over 7 orders of magnitude. The theoretical and experimental results demonstrate that the OPMA with DMI does not increase the system noise level, and hence improves the SNR of the PTI system. This technique presents itself as a solution for enhancing the

sensitivity of sensors predicated on phase modulation, due to its compact design and uncomplicated configuration.

7.2 Future works

The following suggestions are presented as potential avenues for further enhancing the sensitivity and stability of gas detection using HCF based sensors, as well as exploring their practical applications:

1. The effect of temperature on the PT phase modulation and stability of fiber optic interferometers should be considered. Quantitative theoretical and experimental study of the effect of temperature variation might lead to the development of practical gas sensors with improved measurement precision and stability through temperature compensation.
2. The OPMA technique could be further explored using other fiber optic interferometers at destructive interference. Furthermore, the demodulation of the amplified phase modulation can be implemented using different interferometric configurations.